# Design and Fabrication of Ferroelectric Thin Film based Microwave Miniature Tunable Devices

**Zhou Linlin**
(B. Sc., Dalian University of Technology, PRC)

A THESIS SUBMITTED FOR THE
DEGREE OF MASTER
DEPARTMENT OF PHYSICS
NATIONAL UNIVERSITY OF SINGAPORE
2009

# Acknowledgements

I would like to foremost thank my supervisor Professor Ong Chong Kim for his continuous guidance and support during my studies. I am grateful to him for accepting me as a member of his research centre, Centre for Superconducting and Magnetic Materials (CSMM). He has been very involved with my research and provided great helps. I benefited a lot from his deep knowledge during my research.

I also like to thank Dr. Wang Peng for his introduction to microwave theory and computer simulation of microwave devices, as well as his help for advices and discussions. I am grateful for Mr. Cheng Weining for his introduction to pulsed laser deposition and RF sputtering techniques; Dr. Wang Peng for his introduction of lithography and wet etching; Miss Song Qing for her introduction of X-ray diffraction, scanning electron microscope and target preparation.

I would also like to thank my friends at CSMM, Miss Song Qing, Miss Lim Siewleng, Miss Phua Lixian, Dr. Liu Yan, Dr. Liu Huajin and Dr. Wang Peng, with them my graduate life is enrich and happy.

Finally, I want to thank my parents for their endless support and love.

This research is partly supported by Agency for Science, Technology and Research.

# Table of contents

**Contents** **Pages**

# Summary

This study presents a research effort for implementation of room temperature microwave planar tunable filter and phase shifter with barium strontium titanate thin film varactors, as well as characterization of bismuth zinc niobate thin film at microwave frequency for tunable devices applications.

For room temperature operation of the filter and phase shifter, $Ba_{0.5}Sr_{0.5}TiO_3$ thin film varactors and gold strips are chosen. $Ba_{0.5}Sr_{0.5}TiO_3$ thin film has a Curie temperature around room temperature, where high relative permittivity and tunability exist. Thin films are patterned instead of whole plate one, together with high conductivity gold conducting layer, to decrease both the dielectric loss and ohmic loss in the devices. $Ba_{0.5}Sr_{0.5}TiO_3$ thin films as well as $Bi_{1.5}Zn_{1.0}Nb_{1.5}O_7$ thin films are deposited by pulsed laser deposition method, gold conducting layer are grown by RF sputtering and electroplating methods.

The tunable band-pass filter is based on the coupling of microstrip open-loop resonators with $Ba_{0.5}Sr_{0.5}TiO_3$ thin film planar varactors on $LaAlO_3$ (LAO) substrate. The extract of external quality factor and coupling coefficient are studied by full wave electromagnetic simulation. The effects of spacing between resonator at input/output and feed line on the external quality factor as well as the spacing between adjacent resonators on coupling coefficient are discussed. The fabricated filter is measured using vector network analysis (VNA) equipment and the experimental results are compared with its high temperature superconductor (HTS) counterpart.

The phase shifter is designed to consist of high impedance coupled microstrip lines periodically loaded with $Ba_{0.5}Sr_{0.5}TiO_3$ thin films planar varactors on LAO substrate. The balun circuit used to provide odd mode excitation to coupled microstrip lines and also as an impedance matching network is discussed. Expression of the tunability of the phase shifter is deduced to find out factors affecting the tunability. Full wave electromagnetic simulation is performed to study the effects of strip width as well spacing between strips of the coupled microstrip lines and the quarter wavelength lines in the balun circuit on these factors and maximize the tunability. During optimization of phase shifter, impedance matching should also be maintained by examining the dimension of balun circuit. The experimental results of the fabricated phase shifter agree well with the analysis

At last, characterization of $Bi_{1.5}Zn_{1.0}Nb_{1.5}O_7$ thin film as alternative tuning material is performed. Thin films are deposited on platinum coated silicon (Pt/Si) and single crystal LAO, respectively. Crystallization and morphology of thin films are studied by X-ray diffraction and scanning electron microscope. Microwave permittivity characterization is performed at room temperature based on the parallel plate varactor on Pt/Si and planar plate interdigital varactor on LAO substrates. The impedance of the varactor under test is extracted by one-port reflection measurement using VNA equipment. Experimental results of dielectric properties of these two varactors and thin films prove the feasibility of application of $Bi_{1.5}Zn_{1.0}Nb_{1.5}O_7$ thin film into microwave tunable devices.

# List of Figures

**Figure Captions** **Pages**

# Chapter1:

# Introduction

## 1.1 Microwave tunable devices and tuning technologies

Microwave tunable devices mainly include resonators, filters, phase shifters, delay lines, matching circuits, power dividers and oscillators, etc and have applications in both commercial and military communication and radar systems.

Many mechanisms are used to produce tunable microwave devices including ferrite, Micro electromechanical systems (MEMS), semiconductor, ferroelectrics, etc [1-3].Ferrite phase shifters technology has been largely employed in military systems. However, they require strong magnetic fields, which will be power consuming. Besides, ferrite phase shifters are slow and can not be used in application where rapid response is required. Semiconductors are promising in terms of integration possibilities, high tunability and much faster response speed. However, the linear decrease of the quality factor with frequency is the main disadvantage for high frequency above 20GHz applications. Traditional mechanically tunable microwave components are slow and bulky. MEMS varactors are small, low loss and most important, have very high quality factor value. However, the tuning speed and high operating voltage remain issues [4-5].

Ferroelectric materials are of great interest owing to their properties of non-linear relationship between relative permittivity and applied bias electric field, which results in an ability to control their relative permittivity by applying bias electric field. Due to

the high relative permittivity, the sizes of tunable devices based on ferroelectrics are usually small. The breakdown strength of these materials is sufficiently high, so ferroelectric components have high tunability, for thin film parallel plate varactors the tunability can be up to 50%. Ferroelectric device have low power consumption and fast tuning speed of less than 1.0ns. These properties of ferroelectric materials make them promising candidates as tuning elements [6-11].

### 1.2 Ferroelectric thin film and its varactors

Ferroelectrics are important components in a wide spectrum of applications including microsystems, high frequency electrical components, and memories. Application of ferroelectrics to microwave devices began in 1960s [12-16]. At that time, bulk ferroelectrics suffered from the high bias voltage needed for efficient tuning, which usually of the order of hundreds of volts to tens of kilovolts. The investigation of thin film ferroelectric started at the late 1960s and early 1970s for fabrication of memories. However, difficulties with materials processing frustrated their practical applications. Until in 1980s the advances in processing of complex ferroelectric oxide and monolithically compatible processing of ferroelectric thin-film compounds, thin film ferroelectric materials were inspired wide investigation instead of bulk forms taking the advantages of small tuning voltage needed for a required tunability, the potential to produce microwave integrated circuits in one technological cycle to reduce production costs, further miniaturization of devices, and the possibility to integrate with micro electronic circuits [17-19].

### 1.2.1 Non-linear dependence of polarization on an applied electric field of ferroelectric material

In general, ferroelectrics are a class of materials possessing a spontaneous electric polarization. The spontaneous electrical polarization of ferroelectric materials is due to electric dipoles. At a certain temperature range, the centers of the positive and negative charges in a crystal of such a material become displaced even without an external applied electric field. Groups of dipoles tend to align in the same direction instead of random arrangement, which will form a spontaneous polarization domain, to minimize energy. In experiment, spontaneous polarization of ferroelectrics implies a hysteresis loop in the response of polarization to an external electric field as shown in figure1.1.

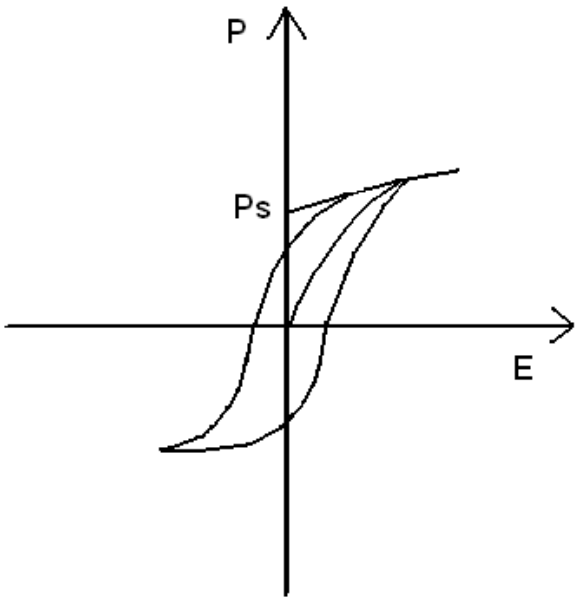


(a)

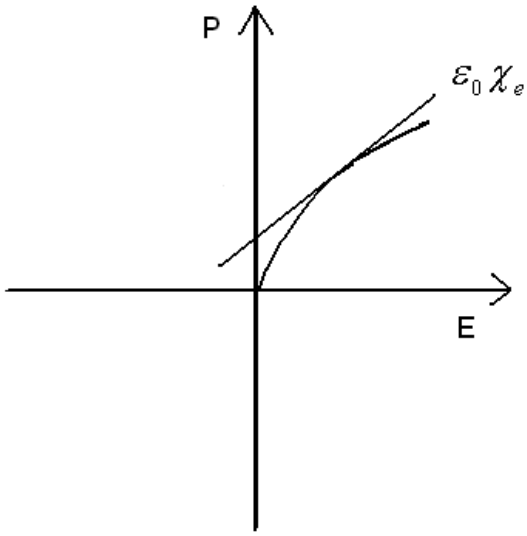


(b)

Figure1.1. Polarization-Electric field curves of ferroelectric material at (a) ferroelectric phase and (b) paraelectric phase.

The material relative permittivity $\varepsilon_r$ is a complex quantity:

$$\varepsilon_r = \varepsilon_r^{'} - j\varepsilon_r^{''} = \mathrm{Re}(\varepsilon_r) - \mathrm{Im}(\varepsilon_r) \qquad (1.1)$$

By definition, the real part of the relative permittivity $\varepsilon_r^{'}$ of ferroelectrics is proportional to the ratio of the electric polarization to applied electric field strength, which is corresponding to the slope of the P-E curve shown in figure1.1. This non-linear polarization for ferroelectric materials is the origin of the changing of relative permittivity $\varepsilon_r^{'}$ on an applied electric field, which is the key to their tunable devices applications.

For description of the non-linear dependence of relative permittivity $\varepsilon_r^{'}$ on bias applied electric field and temperature, a phenomenological model could be expressed [18],

$$\varepsilon_r'(E,T) = \frac{\varepsilon_{00}'}{\phi(E,T)} \tag{1.2}$$

Where

$$\phi(E,T) = \left[\left(\xi^2 + \eta^3\right)^{1/2} + \xi\right]^{2/3} + \left[\left(\xi^2 + \eta^3\right)^{1/2} - \xi\right]^{2/3} - \eta$$

$$\xi(E) = \left[\left(\frac{E}{E_N}\right)^2 + \xi_{st}^2\right]^{1/2}$$

$$\eta(T) = \frac{\Theta}{T_c}\left[\frac{1}{16} + \left(\frac{T}{\Theta}\right)^2\right]^{1/2} - 1$$

Here, $E_N$ is the normalizing bias field, $\xi_{st}$ is the rate of crystal strain, and $\Theta$ the Debye temperature. The change of relative permittivity $\varepsilon_r'$ with frequency is small in the microwave frequency range. $T_c$ is the Curie temperature, $\varepsilon_{00}'$ is a constant analogous to the Curie constant.

For microwave tunable devices applications, the main concern of ferroelectric materials is to what extent the relative permittivity depends on applied electric field. This characteristic is described by the tunability n defined as the ratio of the relative permittivity of the material at zero electric field to its relative permittivity at non-zero electric field,

$$n = \frac{\varepsilon_r'(0)}{\varepsilon_r'(E)} \tag{1.3}$$

$$n_r = \frac{\varepsilon_r'(0) - \varepsilon_r'(E)}{\varepsilon_r'(0)} = 1 - \frac{1}{n} \tag{1.4}$$

Where $n_r$ is the relative tunability. A schematic presentation of the relationship between relative permittivity $\varepsilon_r^{'}$ and bias electric field of a ferroelectric material in the paraelectric phase is shown in figure1.2,

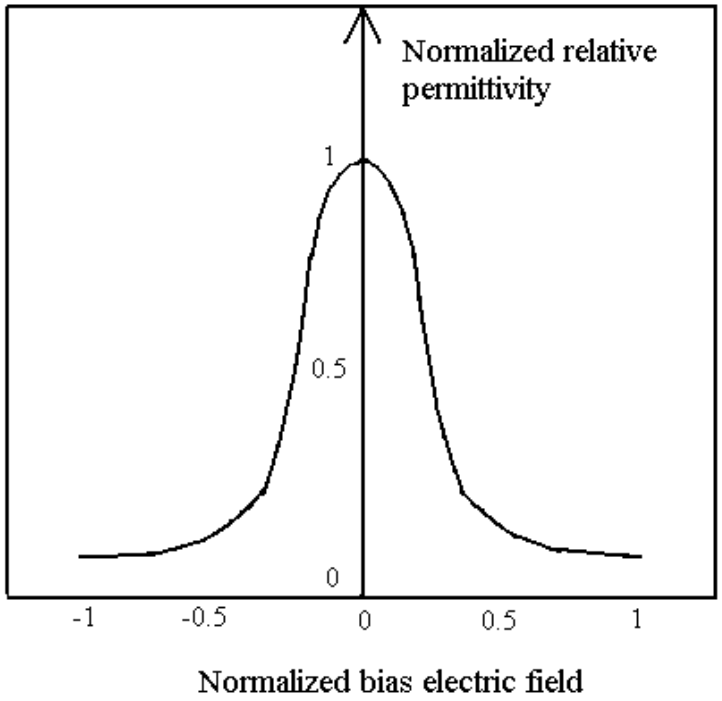


Figure1.2. A typical relative permittivity $\varepsilon_r^{'}$ vs bias electric field characteristics of a ferroelectric material. The relative permittivity and bias electric field are normalized to their maximum values, respectively.

The spontaneous polarization of ferroelectric material is dependent on temperature. The material undergoes a phase transition between ferroelectric phase below their Curie point temperature $T_c$, and a non-polar paraelectric phase above the Curie temperature. The relative permittivity $\varepsilon_r^{'}$ of both bulk and thin film ferroelectric

materials reaches its maximum value when the temperature approaches the Curie temperature.

In the paraelectric regime above Curie temperature, the $\varepsilon_r^{'}$ remains non-linear dependent on the applied electric field and decreases with the increasing of temperature according to the Curie-Weiss relation,

$$\varepsilon_r^{'}(T) = \frac{C}{T - T_c} \tag{1.5}$$

Where C is the Curie constant. For tunable components uses, paraelectric phase slightly above Curie temperature is preferable since it remains high permittivity with property of non-linear electric field dependent complex permittivity and low hysteresis effect.

Another important property of ferroelectric materials is the loss tangent, $\tan\delta$ , defined as the ration of imaginary and real part of the relative permittivity,

$$\tan\delta = \frac{\varepsilon_r^{''}}{\varepsilon_r^{'}} = \frac{\mathrm{Im}(\varepsilon_r)}{\mathrm{Re}(\varepsilon_r)} \tag{1.6}$$

In general the loss in a ferroelectric material originates from three main sources: 1) a fundamental loss associated with multiphonon scattering, 2) a loss associated with the conversion of the microwave field into acoustic oscillations by regions with residual ferroelectric polarization and 3) a loss due to charged defects converting the microwave field into acoustic oscillations [20],

$$\tan\delta = \tan\delta_1 + \tan\delta_2 + \tan\delta_3 \tag{1.7}$$

where

$$\tan\delta_1 = A_1\left(\frac{T}{T_c}\right)^2 \frac{1}{\Phi(E,T)^{3/2}}$$

$$\tan\delta_2 = A_2 Y(E,T)^2 \frac{1}{\Phi(E,T)}$$

$$\tan\delta_3 = A_3 n_d \frac{1}{\Phi(E,T)},$$

$$Y(E,T) = \left[\left(\xi^2+\eta^3\right)^{1/2}+\xi\right]^{1/3} + \left[\left(\xi^2+\eta^3\right)^{1/2}-\xi\right]^{1/3}$$

$$\Phi(E,T) = \left[\left(\xi^2+\eta^3\right)^{1/2}+\xi\right]^{2/3} + \left[\left(\xi^2+\eta^3\right)^{1/2}-\xi\right]^{2/3} - \eta$$

$$\xi(E) = \left[\left(\frac{E}{E_N}\right)^2 + \xi_{st}^2\right]^{1/2}$$

$$\eta(T) = \frac{\Theta}{T_c}\left[\frac{1}{16}+\left(\frac{T}{\Theta}\right)^2\right]^{1/2} - 1$$

Here $A_1$ , $A_2$ , $A_3$ are material parameters, $Y$ is a normalized parameter of the ferroelectric polarization and $n_d$ is the density of charged defects.

Microwave tunable device applications of ferroelectric materials require enough high tunability with low dielectric loss. A Commutation Quality Factor K, which characterizes the tunable performance of the material, is adopted to provide estimation with the optimal trade-off between tunability and dielectric loss,

$$K = \frac{(n-1)^2}{n \cdot \tan\delta(E_1) \cdot \tan\delta(E_2)} \qquad (1.8)$$

where $E_1$ and $E_2$ are the electric field applied in the two states of the ferroelectrics, n is the tunability.

### 1.2.2 Ferroelectric thin film varactors

One of the simplest and most widely used microwave components is a varactor, where more complex circuits such as resonators, filters, phase shifters and mixers are built on. The desired electrical characteristics of varactors are high tunability with low loss tangents (high quality factors) at operation frequency and temperature range [10, 21-22]. Several factors like varactor structure, properties and quality of the thin film used, as well as the type and quality of conducting metallization could play a role.

#### 1.2.2.1 Basic structures of varactors

There are generally two types of thin ferroelectric films varactors used as tunable elements for microwave devices, planar plate varactor and parallel plate varactor as shown in figure1.3 [23].

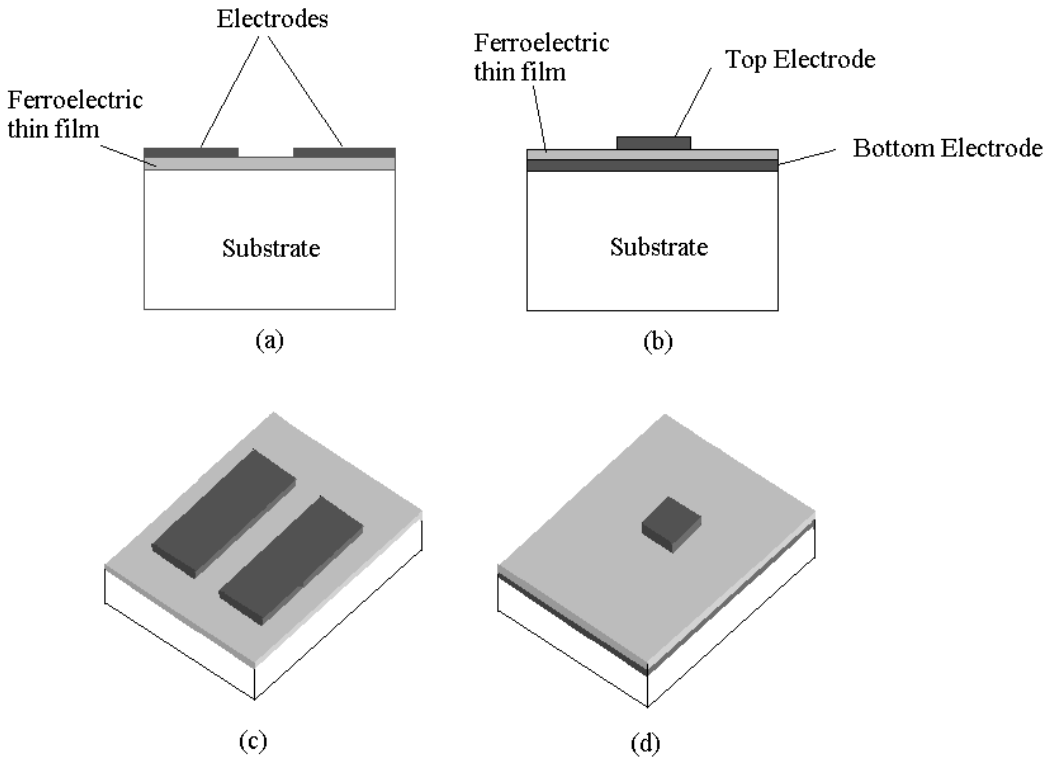


Figure1.3 Layout of planar plate varactor (a) side view and (c) 3D view; parallel plate varactor (b) side view and (d) 3D view.

For planar plate varactor shown in figure1.3 (a) and (c), ferroelectric thin films are deposited on appropriate substrate and electrodes metallization is then patterned on the top of the films. For parallel plate varactor in figure 1.3 (b) and (d), the films are deposited on a bottom electrode on substrate, followed by forming top electrodes on the top of the films.

When bias electric field E is applied across the electrodes for both parallel and planar varactors, the relative permittivity of ferroelectric thin film changes from $\varepsilon_r^{'}(E_1)$

to $\varepsilon_r^{'}(E_2)$ , and thus the capacitance of the varactor altered from $C(\varepsilon_r^{'}(E_1))$ to $C(\varepsilon_r^{'}(E_2))$ with the relative tunability

$$n_r = \frac{C(\varepsilon_r^{'}(E_1)) - C(\varepsilon_r^{'}(E_2))}{C(\varepsilon_r^{'}(E_1))} = 1 - \frac{C(\varepsilon_r^{'}(E_2))}{C(\varepsilon_r^{'}(E_1))} \qquad (1.9)$$

From equation (1.9) for a given bias voltage, narrowing the spacing between electrodes will result in larger electric field in the ferroelectric thin film and thus increasing the tunability of the varactor.

For a planar varactor, the electric field is applied between the electrodes across the gap. For a parallel plate structure, the electric field is applied between the top and bottom electrodes and across the thickness of the ferroelectric thin film. Ferroelectric thin films for microwave tunable components applications generally have a thickness less than 1 $\mu m$, which will be much thinner than the electrodes gap of the planar varactor, which is typically of the order of ten micrometer. As a result, the tuning voltage needed for planar varactor will be more than an order of magnitude, typically in the range of 100V, larger than that for a parallel plate varactor, which is usually 1-20V, to give the same tunability.

On the other hand, the high relative permittivity and the small spacing between electrodes for parallel plate varactor will result in a large capacitance and limit its high frequency applications. Moreover, by far most parallel plate varactors are built with platinum bottom electrodes, which will contribute to the total loss of the device much more than in the case of the planar plate structure.

### 1.2.2.2 Dielectric properties and quality of ferroelectric thin film

The properties of ferroelectrics introduced in section 1.2.1 are equally applicable to bulk and thin film forms. However, the dielectric properties of ferroelectric thin films are usually different from those of bulk materials with lower relative dielectric constant, higher dielectric loss, and in some cases shifted phase transition temperature [7, 24-27] due to additional effects. For example compared with $Ba_{0.7}Sr_{0.3}TiO_3$ ceramic, which has a relative dielectric constant more than 10000 at the phase transition temperature, the value of the relative dielectric constant of $Ba_{0.7}Sr_{0.3}TiO_3$ thin film is only several hundred [28]. The relative dielectric constant of bulk $Ba_{0.1}Sr_{0.9}TiO_3$ is around 6000 in contrast with that of thin film, which has a value of about 480 [24]. The loss tangent of $Ba_xSr_{1-x}TiO_3$ single crystals is of the order of$10^{-3}$, but in the thin film forms this is much bigger in the range of 0.01-0.1 irrespective of their composition [29-32], which could result in a low quality factor of varactor.

Besides the distinct processing conditions, several mechanisms have been proposed to explain this difference. For the permittivity, main effects include mechanical stressing of the film by the substrate, depolarizing effects and the poling effect. For the loss tangent, in contrast to single crystal where the intrinsic loss contribute to the total loss, in thin film the probable loss mechanisms also include charged defects and local polar regions. This relative high dielectric loss of ferroelectric thin film is probably the main area of concern in the development of ferroelectric films for microwave applications, where the losses need to be reduced further if such films are to be used in the widespread applications mentioned previously.

Vary from their bulk forms, performance of thin films could be affected by many external conditions and differs from each other. The deposition methods and conditions such as substrate temperature, deposition rate, working pressure for physical vapor deposition, etc could influence the film stoichiometry and defect population. The choice of substrate is also important because the dielectric properties of thin films could be impacted by the different internal stress and interfacial properties. Substrates with good lattice match at the deposition temperature are preferred. Sapphire, MgO and $LaAlO_3$ are typical substrate for deposition of $Ba_xSr_{1-x}TiO_3$ thin film due to their good lattice matching to the perovskite ferroelectrics. For thin film deposited on metal bottom electrodes, as in the case of parallel plate varactor, the lattice mismatch could induce additional stress. An approach to control the strain caused by lattice mismatch is to grow a buffer layer. Post-annealing procedure could also reduce the defects density and improve the homogeneity. In addition, doping has proved to be an effective method to improve the dielectric properties of a ferroelectric thin film by means of substitution of the cations or redistribution of the precipitation of a non-ferroelectric phase at grain boundaries.

#### 1.2.2.3 Barium strontium titanate ferroelectric thin film

Barium strontium titanate, a continuous solid solution of $BaTiO_3$ and $SrTiO_3$ and denoted as $Ba_xSr_{1-x}TiO_3$ (BST), is one of the widely investigated ferroelectric materials due to its high relative permittivity, moderate loss tangent and significant tunability.

Especially, $Ba_xSr_{1-x}TiO_3$ is preferable for room temperature devices applications as tunable components because it's Curie temperature and hence its electric properties can be tailored by variation of the Ba/Sr composition. Since the Curie temperature of $Ba_xSr_{1-x}TiO_3$ decreases linearly with increasing Sr concentration at a rate of 3.4°C per mole % Sr, with the value of x varies from 0 to 1, the Curie temperature of $Ba_xSr_{1-x}TiO_3$ changes from about 40K for $SrTiO_3$ (STO) to 400K for pure $BaTiO_3$ (BTO). Generally, a value of x in the range from 0.4-0.6 is desirable for room temperature application and thus $Ba_{0.5}Sr_{0.5}TiO_3$ thin film with Curie temperature around room temperature is used in this work as tuning elements of filter and phase shifter [10].

#### 1.2.2.4 Bismuth Zinc Niobate thin film as alternative candidate for tuning materials

Other than $Ba_xSr_{1-x}TiO_3$ thin film, several materials have been considered for tunable devices applications. For example, incipient ferroelectric $SrTiO_3$ thin film mentioned in earlier section presents high permittivity and tunability at ~77K, thus suitable for low temperature applications [33]. Investigations also show that dielectric properties of $Pb_{0.3}Sr_{0.7}TiO_3$ thin film are comparable to that of $Ba_xSr_{1-x}TiO_3$ thin films at microwave frequency [34].

$Bi_{1.5}Zn_{1.0}Nb_{1.5}O_7$ ceramics in $Bi_2O_3$ - $ZnO$ - $Nb_2O_5$ system have attracted much attention due to low temperature coefficient, low sintering temperature, medium relative permittivity and tunability with very low dielectric losses. Unlike most

ferroelectric thin film, it is found that the dielectric properties of $Bi_{1.5}Zn_{1.0}Nb_{1.5}O_7$ thin films are comparable to those reported for bulk $Bi_{1.5}Zn_{1.0}Nb_{1.5}O_7$ [35-36] with further advantages of size reduction and lower tuning voltage needed [35-40]. These properties make $Bi_{1.5}Zn_{1.0}Nb_{1.5}O_7$ thin film to be a promising candidate for tuning elements applications.

#### 1.2.2.5 Conductor layer and conducting loss

Except for dielectric loss of thin film material, conductor loss from metal conducting layer also contributes to the total loss of varactor. There are generally two kinds of conducting metallization for microwave devices depending on the operation temperature: superconductor and normal metal.

In 1987 the development of high-temperature superconductor (HTS) in complex metal oxide simulates the insertion of ferroelectric thin film into microwave system because the extremely small loss in HTS film suggests integration of HTS with ferroelectric material could reduce the overall losses of the devices [41-44]. In addition, the similar perovskite type crystal structure of superconductive oxide $YBa_2Cu_3O_7$ and ferroelectrics assures a high quality interface between ferroelectric thin film and HTS electrodes. Typical representatives of incipient ferroelectric thin films $SrTiO_3$ (STO) and $KTaO_3$ (KTO) as well as conventional ferroelectric thin film $Ba_xSr_{1-x}TiO_3$ with x value around 0.1 could be applied in conjunction with HTS films because of their crystalline compatibility with HTS and their properties at cryogenic temperature.

On the other hand, the complication of low temperature technique and the high cost of the cryogenic equipments together with the situation, where cryogenic requirements are not acceptable, necessitate the development of microwave devices operating at room temperature. Therefore, efforts in optimizing tunable microwave devices operating at room temperature to realize devices which have large frequency tunability with acceptable low losses are worthwhile [45-47]. $Ba_xSr_{1-x}TiO_3$ thin film with x a value in the range of 0.4-0.6 posses a Curie temperature around room temperature as well as $Bi_{1.5}Zn_{1.0}Nb_{1.5}O_7$ thin film are favored tuning elements for room temperature applications.

### 1.3 Scope and outline of this study

A brief outline of the organization of this thesis is as follows:

In chapter2, methods and processes involving in filter, phase and varactor fabrication of this study are discussed. Systems and equipments used including pulsed laser deposition, RF sputtering and electroplating are presented.

Chapter3 describes development of a microwave planar tunable band-pass filter using $Ba_{0.5}Sr_{0.5}TiO_3$ thin film varactors as tuning components for room temperature application. A general overview of microwave filter is introduced that includes theory and establishment of prototype, frequency and elements transformation, physical implementation and transmission media. The design details of the tunable filter and its open-loop resonator structures will be explained next. Last part discusses the measured performance of the filter with a comparison with its HTS counterpart.

In chapter4, a microwave planar tunable phase shifter using $Ba_{0.5}Sr_{0.5}TiO_3$ thin film varactors as tuning element for room temperature application is implemented. The first part introduces the general phase shift theory of a transmission line, followed by even and odd modes of coupled microstrip lines. Balun structure will be explained next. Then the design details of the phase shifter will be described and optimization of maximum phase shifter will be demonstrated. At last, the measured performance of the phase shifter will be discussed.

Chapter5 demonstrates characterization of bismuth zinc niobate $Bi_{1.5}Zn_{1.0}Nb_{1.5}O_7$ thin film at microwave frequency. A general structure of $Bi_{1.5}Zn_{1.0}Nb_{1.5}O_7$ thin film is described first. Crystallization, surface and cross-section morphology will also be examined by X-ray diffraction and scanning electron microscope. The detailed dielectric properties of $Bi_{1.5}Zn_{1.0}Nb_{1.5}O_7$ thin film will be characterized at microwave frequency based on parallel plate varactor and planar plate interdigital varactor structures. Meanwhile, the performance of these two varactors will be discussed.

**Reference**

[1] Gerald F. Dionne, Daniel E. Oates and Donald H. Temme, YBCO/Ferrite low loss microwave phase shifter, *IEEE Transactions on Applied Superconductivity,* Volume 5, Number 2 , Pages 2083–2086 (1995)

[2] Huey D. Wu, Kevin F. Harsh, Ronda S. Irwin, Wenge Zhang, Alan R. Mickelson and Y.C. Lee, MEMS designed for tunable capacitors, *Microwave Symposium Digest, 1998 IEEE MTT-S International,* Volume 1, Pages 127-129 (1998)

[3] S.R. Chandler, I.C. Hunter, and J.G. Gardiner, Active Varactor Tunable Bandpass Filter, *IEEE Guided wave letters*, Volume 3, Number 3, Pages 70-71 (1993)

[4] Robert R. Romanofsky, Array Phase Shifters: Theory and Technology, *NASA Technical Memorandum* TM-2007-214906 (2007)

[5] Eric Marsan, Jules Gauthier, Mohamed Chaker and Ke Wu, Tunable microwave device: status and perspective, IEEE-NEWCAS Conference, 2005. The 3rd International, Pages 279-283 (2005)

[6] X.X.Xi, Hong-Cheng Li, Weidong Si, A.A.Sirenko, I.A.Akimov, J.R.Fox, A.M.Clark and Jianhua Hao, Oxide thin films for tunable microwave devices, *Journal of Electroceramics* , Volume 4 , issue 2/3, Pages 393-405 (2000)

[7] O. G. Vendik, E. K. Hollmann, A. B. Kozyrev, and A. M. Prudan Ferroelectric tuning of planar and bulk microwave devices, *Journal of Superconductivity*, Volume12, Number 2, Pages 325-338 (1999)

[8] Felix A Miranda, Fred W.Van Keuls, Robert R.Romanofsky, Carl H. Mueller, Samuel Alterovitz and Guru Subramanyam, Ferroelectric thin films-based technology for frequency- and phase- agile microwave communication applications, *Integrated Ferroelectrics,* Volume 42, Pages 131-149 (2002)

[9] A.K.Tagantsev, V.O.Sherman, K.F. Astafiev, J.Venkatesh, and N.Setter, Ferroelectric Materials for Microwave Tunable Applications, *Journal of Electroceramics,* Volume 11, Pages 5-66 (2003)

[10] M J Lancaster, J Powell and A porch, Thin-film ferroelectric microwave devices *Superconductor Science and Technology*, Volume11, Nomber11, Pages1323-1334 (1998)

[11] N. Setter, D. Damjanovic and L. Eng, Ferroelectric thin films: Review of materials, properties and applications*, Journal of applied physics*, 100, 051606 (2006)

[12] M. Di Domenico, D.A. Johnson and R.H. Pantell, Ferroelectric garmonic generator and the large-signal microwave characteristics of ferroelectric ceramic, *Journal of Applied Physics,* Volume 33, pages 1697-1706 (1962)

[13] Microwave ferroelectric phase shifters and switches, *US Army Final Report* Contract DA 36-039-AMC-02340 (E) US Army Electronics Laboratories, Fort Monmouth, NJ, USA (1964)

[14] Rupprecht G and Bell P O, Microwave losses in Strontium Titanate above the phase transition, *Physical Review,* Volume 123, Issue 6, Pages 1915–1920 (1962)

[15] K. M. Johnson, Variation of dielectric constant with voltage in ferroelectric ceramics, *Journal of Applied Physics,* Volume 33, Pages 2826-2831 (1962)

[16] Yu. M. Poplavko, Electrically controlled ferroelectric devices at microwaves, *Radio Eng. Electr*. 7(8), Pages 1458-1462 (1962)

[17] O. G. Vendik, I. G. Mironenko, and L. T. Ter-Martirosyan, Some properties and applications of ferroelectrics at microwaves, *Journal De Physique*, Volume 33, Number 4, Pages C2 277–280 (1972)

[18] O. G. Vendik, Dielectric nonlinearity of the displacive ferroelectrics at UHF, *Ferroelectrics*, Volume 12, Issue 1, Pages 85–90 (1976)

[19]. O. G. Vendik, Ferroelectrics at microwaves (in Russian) (Sovyetskoye Radio , Moscow, 1979)

[20] Orest G. Vendik, Leon T. Ter-Martirosyan and Svetlana P. Zubko, Microwave losses in incipient ferroelectrics as functions of temperature and biasing field, *Journal of applied physics,* Volume 84, Number 2, Pages 993–998 (1998)

[21] David S. Korn and Huey Daw Wu, A comprehensive review of microwave system requirements on thin-film, *Integrated Ferroelectrics*, Volume 24, Pages 215-237 (1999)

[22] R. York, A. Nagra, E. Erker, T. Taylor, P. Periaswamy, J. Speck, S. Streiffer, and O. Auciello, Microwave Integrated Circuits using Thin-Film BST, *Applications of Ferroelectrics, 2000. ISAF 2000. Proceedings of the 2000 12th IEEE International Symposium on,* Volume 1, Pages 195-200 (2000)

[23] P Bao, T J Jackson, X Wang and M J Lancaster, Barium strontium titanate thin film varactors for room-temperature microwave device applications, *Journal of physics D: Applied physics*, Volume 41, Number6, 063001, Pages1-21 (2008)

[24] Abdelkader Outzourhit, John U. Trefny, Tomoko Kito, Baki Yarar, Ali Naziripour, and Allen M. Hermann, Fabrication and characterization of Ba1-x Sr1-x TiO3 tunable thin film capacitors, *Thin Solid Films*, Volume 259, Pages 218-224 (1995)

[25] O.G. Vendik, E. Kollberg, S.S. Gevorgian, A.B. Kozyrev, and O.I. Soldatenkov, 1 GHz tunable resonator on bulk single crystal SrTiO3 plated with YBa2Cu3O7-x films, *Electronics Letters*, Volume 31, Number 8, Pages 654-656 (1995)

[26]. M.J. Dalberth, R.E. Stauber, J.C. Price, C.T. Rogers, and D. Galt, *Applied Physics Letters.*, Volume **72**, Pages 507-509 (1998).

[27] Yyes Lemaitre, Bruno Marcilhac, Daniel Mansart, Julius Siejka, and Jean Claude Mage, Study of YBa2Cu3O7-x/SrTiO3 heterostructures on 2" LaAlO3 substrates for microwave applications, *Physica C*, Volume **372**, Pages667-670 (2002).

[28] T. M. Shaw, Z. Suo, M. Huang, E. Liniger, R.B.Larbowitz and J.D. Baniecki, The effect of stress on the dielectric properties of barium strontium titanate thin films, *Applied Physics Letters*, Volume 75, Number 14, Pages 2129-2131 (1999)

[29] Miranda F A, Mueller C H, Cubbage C D, Bhasin K B, Sing R K and Harkness S D, HTS/ferroelectric thin films for tunable microwave components, *IEEE Transactions Applied Superconductivity,* Volume 5, Issue 2, Pages 3191–3194(1995)

[30] Miranda F A, Mueller C H, Koepf G A and Yandrofski R M, Electrical response of ferroelectric/superconducting/dielectric Ba*x*Sr1−*x*TiO3/YBa2Cu3O7−delta/LaAlO3 thin-film multilayer structures, *Superconductor. Science and Technology,* Volume 8, Pages 755–763 (1995)

[31] Huey Daw Wu , Zhihang Zhang , Frank Barnes , Charles M. Jackson, Aron Kain and J.D. Cuchiaro, Voltage tunable capacitors using high temperature superconductors and ferroelectrics, *IEEE Transactions on Applied Superconductivity,* Volume 4, Number 3, Pages 156–159 (1994)

[32] U. Syamaprasad, R K, Galgali and B.C. Mohanty, Dielectric properties of Ba1−*x*Sr*x*TiO3 system, *Materials Letters,* Volume 7, Number 5,6 Pages 197–200 (1988)

[33] Hong-Cheng Li, Weidong Si, Alexander D. West and X X Xi, Near single crystal-level dielectric loss and nonlinearity in pulsed laser deposited SrTiO3 thin films, *Applied Physics Letters,* Volume 73, Number 2, Pages 190-192 (1998)

[34] Dey, S K Wang ,C G Cao ,W Bhaskar, S Li, J and Subramanyam G, Voltage tunable epitaxial $Pb_xSr_{1-x}TiO_3$ films on sapphire by MOCVD: Nanostructure and microwave properties, *Journal of Materials Science,* Volume 41, Pages 77-87 (2006)

[35] R. L. Thayer, C. A. Randall and S. Trolier-McKinstry, Medium permittivity bismuth zinc niobate thin film capacitors, *Journal of applied physics*, Volume 94, Number 3, Pages 1941-1947 (2003)

[36] Wei Ren, Susan Trolier-McKinstry, Clive A. Randall, and Thomas R. Shrout, Bismuth zinc niobate pyrochlore dielectric thin films for capacitive applications, *Journal of applied physics*, Volume 89, Number 1, Pages 767-774 (2001)

[37] Young P. Hong, Seok Ha, Ha Yong Lee, Young Cheol Lee, Kyung Hyun Ko, Dong-Wan Kim, Hee Bum Hong and Kug Sun Hong, Voltage tunable dielectric properties of rf sputtered $Bi_2O_3$ - $ZnO$ - $Nb_2O_5$ pyrochlore thin films, *Thin Solid Films*, Volume 419, Pages 183-188 (2002)

[38] Shan-Tao Zhang, Yi-Zhang, Ming-Hui Lu, Yan-Feng Chen and Zhi-Guo Liu, Structures and dielectric properties of $Bi_{1.5}Zn_{1.0}Nb_{1.5-x}Ti_xO_7$ (x=0, 0.05 and 0.10) thin films, *Applied physics letters*, Volume 90, 042903 (2007)

[39] S.HA, Y.S.LEE, Y.P.HONG, H.Y.LEE, Y.C.LEE, K.H.KO, D.W.KIM, H.B.HONG and K.S.HONG, The effect of substrate heating on the tunability of rf-sputtered $Bi_2O_3$ - $ZnO$ - $Nb_2O_5$ thin films, *Applied physics A*, Volume 80, Pages 585-590 (2005)

[40] S.W.Jiang, B.Jiang, X.Z.Liu and Y.R.Li, Laser deposition and dielectric properties of cubic pyrochlore bismuth zinc niobate thin films, *Journal of Vacuum Science and Technology A*, Volume 24, 261-263 (2006)

[41] Raafat R. Mansour, Microwave superconductivity, *IEEE transactions on microwave theory and techniques,* Volume 50, Number 3, Pages 750-759 (2002)

[42] Spartak S. Gevorgian, Erik F. Carlsson, Staffan Rudner, Ulf Helmersson, Erik L. Kollberg, Erfand Wikborg, and Orest G.Vendik, HTS/Ferrolectric Devices for Microwave Application, *IEEE transactions on applied superconductivity,* Volume 7, Number 2, Pages 2458-2461 (1997)

[43] O. G. Vendik, I. G. Mironenko, and L. T. Ter-Martirosyan, Superconductors spur application of ferroelectric films, *Microwaves and RF*, Pages 67–70 (1994).

[44] O. G. Vendik, L. T. Ter-Martirosyan, A. I. Dedyk, S. F. Karthemanenko, and R. A. Chakalov, High-Tc superconductivity: New applications of ferroelectrics at microwave frequencies, *Ferroelectrics,* Volume 144, Issue 1, Pages 33–43 (1993).

[45] O.G. Vendik, Ferroelectric films in microwave technique: physics, characterization, and tunable devices, *Physics and Engineering of Microwaves, Millimeter, and Submillimeter Waves, MSMW 04. The Fifth International Kharkov Symposium on*, Volume 1, Pages 66-71 (2004)

[46] C. L. Chen, H. H. Feng, Z. Zhang, A. Brazdeikis, Z. J. Huang, W. K. Chu, and C. W. Chu, Epitaxial ferroelectric Ba0.5Sr0.5TiO3 thin films for room-temperature tunable element applications, *Applied physics letters,* Volume 75, Number 3, Pages 412-414 (1999)

[47] O. G. Vendik and S.P.Zubko, Ferroelectric phase transition and maximum dielectric permittivity of displacement type ferroelectrics, *Journal of applied physics,* Volume 88 Number 8, Pages 5343-5350 (2000)

# Chapter2:

# Fabrication of thin films and conducting layers

This chapter concerns fabrication methods and process involving in the thin films and conducting layers for the filter, phase shifter and varactor implemented in later chapter 3, 4 and 5. In the first part, after an introduction to pulsed laser deposition theory and system, parameters for $Ba_{0.5}Sr_{0.5}TiO_3$ and $Bi_{1.5}Zn_{1.0}Nb_{1.5}O_7$ thin films deposition are presented. Next, sputtering deposition and electroplating methods used for the growth of conducting metal are explained. Process of lift-off method for patterned $Ba_{0.5}Sr_{0.5}TiO_3$ thin film is discussed in the last section.

## 2.1 Pulsed laser deposition of Barium strontium titanate and Bismuth zinc niobate thin films

Thin films could be prepared by RF sputtering deposition, chemical vapor deposition, metalorganic deposition and pulsed laser deposition (PLD), etc. The PLD process has been widely applied for thin film deposition due to its ease of use, low cost, conceptually simple, suitable for many materials deposition and precise control of the stoichiometry composition.

### 2.1.1 Target preparation

Targets of both $Ba_{0.5}Sr_{0.5}TiO_3$ and $Bi_{1.5}Zn_{1.0}Nb_{1.5}O_7$ are self-prepared. In contrast to well studied $Ba_{0.5}Sr_{0.5}TiO_3$, $Bi_{1.5}Zn_{1.0}Nb_{1.5}O_7$ is new in our lab. The target material of

$Bi_{1.5}Zn_{1.0}Nb_{1.5}O_7$ is prepared using a conventional solid reaction process. $Bi_2O_3$, $ZnO$ and $Nb_2O_5$ powders are weighed according to the composition of $Bi_{1.5}Zn_{1.0}Nb_{1.5}O_7$ and then mixed as aqueous slurries using acetone by ball milling for 4hours.The resulting powders are dried out and then calcined at 800 for 4hours in furnace. After calcination, the powders are pressed into pellets about 30mm in diameter and 3mm in thickness. The pellets are sintered at 950 °C in oven for 4hours.

### 2.1.2 Introduction to pulsed laser deposition system

The system set-up of a PLD system is quite simple and the main components include a laser system, optics, a vacuum system and a chamber. A schematic configuration of a basic PLD system is shown in figure2.1.

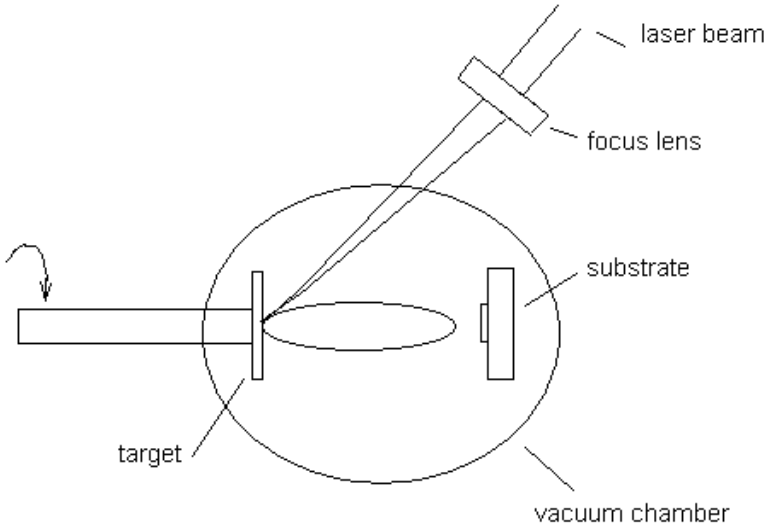


Figure2.1 A schematic diagram of PLD system.

Compared with its simple system set-up, the physical principle of thin film formation in PLD is very complex and generally could be described by four stages: the

interaction of pulsed laser with target, formation and transfer of ablation materials, deposition of the ablated materials on the substrate, nucleation and growth of thin film on the substrate.

As the beginning, a high power pulsed laser beam, which could be produced from a laser system, is focused inside a vacuum chamber to strike a target with the desired composition. Commonly used lasers include ArF, KrF excimer lasers and Nd:YAG laser. The incident laser pulse penetrates into the surface of the target material and the electrons of the material within the penetration region could be removed by the electromagnetic field of the laser light. These free electrons then oscillate within the electromagnetic field of the laser light and collide with the atoms of the target material. By this means, energy of electrons are transferred to the lattice of the target material. At sufficiently high flux densities and short pulse duration, surface of the target is heated up and materials with stoichiometry as in the target are dissociated from the target surface and form a plasma plume.

At the second stage, these emitted materials expand perpendicularly to the target surface to the suitably positioned substrate. The third stage involves interaction between the ejected species and the substrate. High energy species ablated from the target strike the substrate surface and a collision region will be formed between incident elements from target and sputtered species from the substrate. This region serves as a source for condensation of particles. When the condensation rate is high enough, a thermal equilibrium can be reached and the film begins to grow on the substrate surface at the expense of the direct flow of ablation particles and the thermal equilibrium obtained.

Film nucleates and grows at the fourth stage. The nucleation process depends on the interfacial energies between the three phases present - substrate, the condensing material and the vapor. The crystalline film growth depends on the surface mobility of the atoms [1].

Deposition parameters, including laser density and frequency, deposition gas pressure, substrate temperature, target-to-substrate distance, should be optimized to achieve high quality thin films.

### 2.1.3 Deposition parameters for $Ba_{0.5}Sr_{0.5}TiO_3$ and $Bi_{1.5}Zn_{1.0}Nb_{1.5}O_7$ thin films

Both $Ba_{0.5}Sr_{0.5}TiO_3$ and $Bi_{1.5}Zn_{1.0}Nb_{1.5}O_7$ thin films used in this study are prepared using a KrF excimer (λ= 248nm) complex 201 PLD system (Lambda Physik, Germany) from their stoichiometric ceramic targets. Substrate for $Ba_{0.5}Sr_{0.5}TiO_3$ thin film filter and phase shifter are (001) $LaAlO_3$ (LAO) single crystal; those for $Bi_{1.5}Zn_{1.0}Nb_{1.5}O_7$ thin film varactors are commercial (111) platinum coated silicon (Pt (200nm)/Ti (20nm)/SiO2 (500nm)/Si) to form parallel plate varactor and (001) $LaAlO_3$ (LAO) single crystal substrate for planar plate varactor. The depositions are carried out with a pulse frequency of 3Hz and an energy density of 1.5 $J/cm^2$ for $Ba_{0.5}Sr_{0.5}TiO_3$ thin film and 5Hz, 1.0 $J/cm^2$ for $Bi_{1.5}Zn_{1.0}Nb_{1.5}O_7$ thin film. The substrate temperatures for $Ba_{0.5}Sr_{0.5}TiO_3$ and $Bi_{1.5}Zn_{1.0}Nb_{1.5}O_7$ thin films are 700°C and 650°C when deposition is carried out and the substrate to target distance maintains at 48mm.The base pressure in the vacuum chamber is $1.0x10^{-5}$ mbar. High

purity oxygen is used as reactive gas and working pressure during deposition is 0.2mbar for $Ba_{0.5}Sr_{0.5}TiO_3$ thin film and 0.5mbar for $Bi_{1.5}Zn_{1.0}Nb_{1.5}O_7$ thin film. Half an hour in-situ post-annealing is performed for both thin films after deposition to improve the crystallization of the films.

### 2.2 Preparation of conducting layer

Conducting material used for room temperature filter, phase shifter and varactor in this study is gold. For microwave devices applications, thick metal layers, usually several time of the skin depth at the operation frequency range, are preferable. In our lab, after deposit a thin film Cr and Au seed layer about several ten nanometers by RF sputtering, electroplating process is carried out to grow thick gold layer.

#### 2.2.1 RF sputtering of thin Au/Cr seed layer

Like pulsed laser deposition, sputtering deposition is also a physical vapor deposition process of thin films, in which gaseous ions collide with the target and atoms of target materials are removed and then condensed on the substrate surface. Usually magnetrons are used to confine electrons close to the surface of the target and produce more ionizing collisions with gaseous neutrals resulting in higher deposition rate.

In this study, the Au/Cr seed layers are grown using a C·K-6B metal multilayer film magnetro sputtering system (Shenyang Institute of UHV Technology and Applications). Firstly, 20nm chromium layer is grown with RF energy of 100W. Then

20nm gold layer is deposited on top of the chromium using 80W RF energy. The working pressures for these two films are $2\times10^{-3}$ mbar.

### 2.2.2 Electroplating of thick gold layer

Electroplating is a material deposition method using electric current to remove cations of a desired material from a solution to the object to be plated at the cathode. In our lab, the electroplating process is carried out in a self-constructed simple electroplating system. The anode is made of a gold wire and cathode is the sample after Au/Cr seed layer deposition. Solution used is commercial Microfab® AU 100 (Electroplating Engineers of Japan). During plating, the temperature of solution maintains 60°C and DC current density is 5mA/cm$^2$.

### 2.3 Lift-off method for fabrication of patterned $Ba_{0.5}Sr_{0.5}TiO_3$ thin films

In a microwave device, conductor loss, dielectric loss, radiation loss and losses due to mismatching contributes the total insertion loss. For the filter and phase shifter designed in this study, we follow the lift-off method to prepare patterned $Ba_{0.5}Sr_{0.5}TiO_3$ thin film instead of whole plate $Ba_{0.5}Sr_{0.5}TiO_3$ to reduce the dielectric loss [2-3]. The sideview of these two types of $Ba_{0.5}Sr_{0.5}TiO_3$ thin films structure are shown in figure2.2 below,

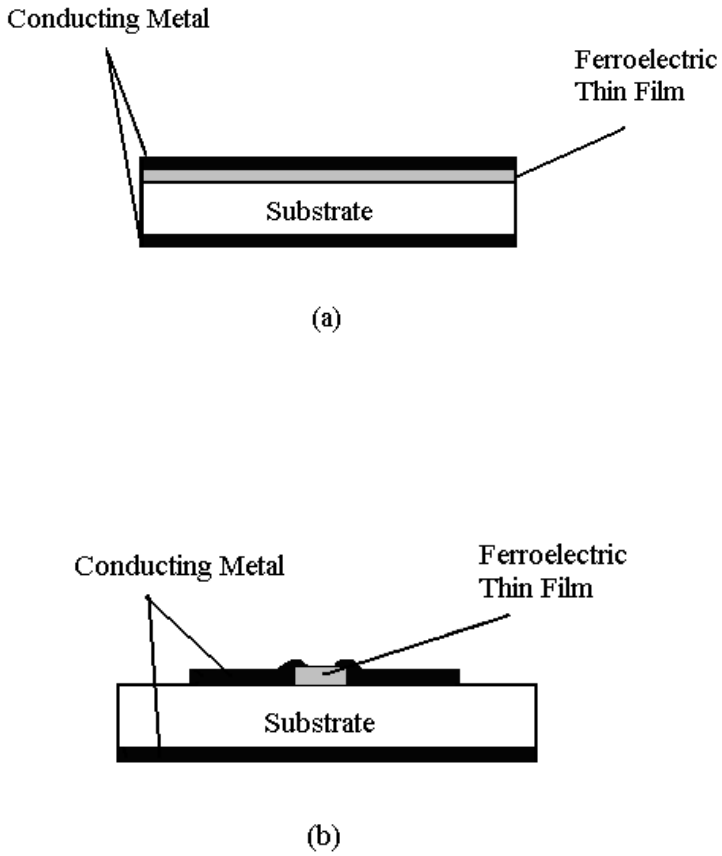


Figure2.2. Side view of (a) whole plate and (b) patterned $Ba_{0.5}Sr_{0.5}TiO_3$ thin film

In the patterned $Ba_{0.5}Sr_{0.5}TiO_3$ thin film structure, only the parts of device where tunability is needed are patterned with $Ba_{0.5}Sr_{0.5}TiO_3$ thin film. In the design of filter, only six rectangular $Ba_{0.5}Sr_{0.5}TiO_3$ thin films with the area of 0.09mm*0.36mm are used instead of 10mm*10mm whole plate film. This will decrease the dielectric loss in $Ba_{0.5}Sr_{0.5}TiO_3$ thin film largely.

### 2.3.1 Fabrication of patterned $Ba_{0.5}Sr_{0.5}TiO_3$ thin film

In order to obtain the patterned $Ba_{0.5}Sr_{0.5}TiO_3$ thin films, a lift-off method is adopted. In the lift-off method, $YBa_2Cu_3O_{7-\delta}$ (YBCO) thin film is deposited firstly by the pulsed laser deposition method on the substrate as a refractory masking layer. The thickness of YBCO thin film is 400nm. Then using photolithography to remove the unusable parts of YBCO and only maintain the usable parts. These remaining parts are the opposite pattern of $Ba_{0.5}Sr_{0.5}TiO_3$ thin films designed. Then 300nm $Ba_{0.5}Sr_{0.5}TiO_3$ thin film is deposited by PLD with parameters in section2.1.3. After growth of $Ba_{0.5}Sr_{0.5}TiO_3$ thin film, YBCO thin film is removed by wet etching technique. Above this YBCO thin filter is the undesirable parts of $Ba_{0.5}Sr_{0.5}TiO_3$ film. So these undesirable parts of $Ba_{0.5}Sr_{0.5}TiO_3$ film are removed together with YBCO and designed pattern of $Ba_{0.5}Sr_{0.5}TiO_3$ is obtained. A schematic process flow of the fabrication of the patterned $Ba_{0.5}Sr_{0.5}TiO_3$ thin film is shown in figure2.3 below,

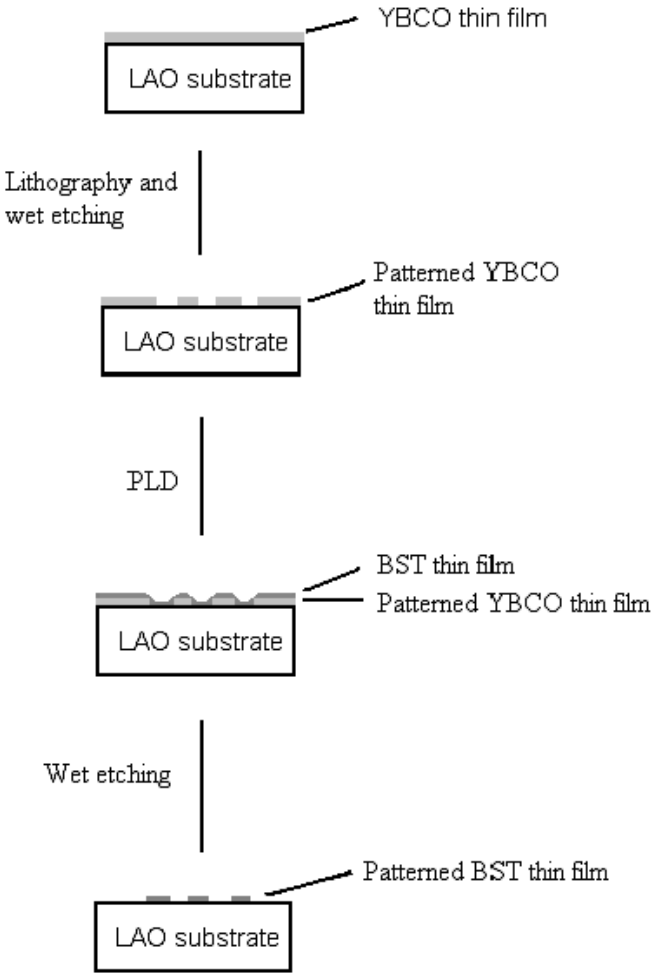


Figure2.3 Fabrication process flow for patterned $Ba_{0.5}Sr_{0.5}TiO_3$ thin film

**Reference**

[1] Douglas B. Chrisey and Graham K. Hubler, *Pulsed Laser Deposition of Thin Films*, John Wiley & Sons (1994)

[2] Tan Chin Yaw, *High Tc superconductor, ferroelectric thin films and microwave devices*, Ph. D. Thesis, National University of Singapore(2005).

[3] C K Ong and C. Y. Tan, patterned ferroelectric thin film for microwave devices,

US Patent No US 2006/0201415 A1 (2006)

# Chapter3:

# Microwave tunable coupled microstrip open-loop resonators bandpass filter with $Ba_{0.5}Sr_{0.5}TiO_3$ thin film varactors

A microwave filter is a two-port frequency selection device, which is designed to select, reject, channel, separate, or combine microwave signals at selected frequency ranges. World War Π and the invention of radar commence significant developments in filters to separate the complete band of radar signal into sub-bands. This chapter is arranged to describe the design, fabrication and measurement of a coupled microstrip open-loop resonators bandpass filter using $Ba_{0.5}Sr_{0.5}TiO_3$ thin film varactors as tuning element on $LaAlO_3$ substrate. After a general introduction to microwave filter, the low-pass prototype specification and band-pass parameters of the filter are determined. The third part concerns the theory and realization of the open-loop resonator, followed by the explanation of external quality factor and coupling coefficient for designing the filter. After fabrication of the filter, in the last section, measurement performance of the filter is presented and discussed.

## 3.1 Introduction to design of microwave filter

From the insertion loss viewpoint, the design of microwave filters is normally starting with selecting a low-pass prototype network, regardless of the eventual physical realization of the filter. Low-pass prototype networks are basically two-port lumped-element circuits with an angular cutoff frequency of 1 rad/s and a normalized source and load resistance 1Ω. Butterworth, chebychev, as well as elliptic, etc are typical

types of the low-pass prototype responses, which exhibit maximally flat passband, equal ripple passband or equal ripple in both passband and stopband. The choice of the type of the response and parameters of the low-pass prototype like ripple level, number of order are depended on the filter specification including return loss level in the pass-band, rejection loss level in the stop-band, etc. After determining the ripple level and number of order for the specific low-pass prototype filter, the normalized element values of the low-pass prototype can be obtained from tables, which have been investigated by researchers and could be found in textbooks and papers. Followed by applying frequency and element transformations, the response of any type low-pass lumped-element prototype circuit can be related to the response of a corresponding practical low-pass, high-pass, band-pass or band-stop filter. Frequency transformation involves the process to map a response in the low-pass prototype frequency with a cutoff frequency 1 to that in the practical filter response with desired cutoff or pass-band, stop-band frequency. The normalized reactive elements with respect to the source impedance in the low-pass prototype could also, by applying impedance transformation, be transformed to the elements of the practical filter with desired source impedance. Figure3.1 shows a schematic circuit of low-pass prototype filter and its transformation to a band-pass filter.

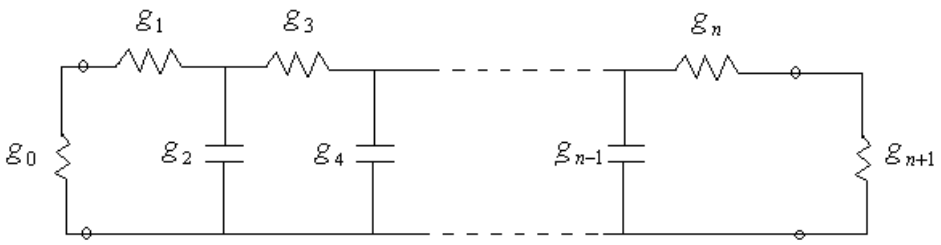

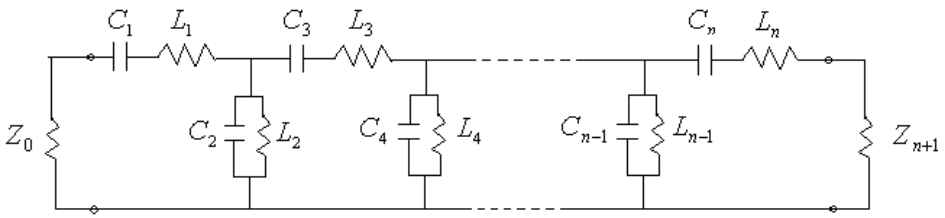


Figure3.1 (a) Low-pass prototype filter (b) Band-pass filter transformed from the low-pass prototype

Having determined the lump-element filter circuit, the next step involves transformation of this lumped-element filter into microwave structure and physical realization of the microwave filter. Here, Richard's transformation can be used to convert lump-elements to transmission line sections by means of replacing the inductors and capacitors of the lump-element filter circuit by short-circuited and open-circuited stubs. Furthermore, for practical filter implementation, Kuroda's identities, impedance inverters or admittance inverters may be used to facilitate the implementation of filters. Design formulas for specific filter could be applied to calculate the dimension and layout of the filter. For coupled resonators filters, like the band-pass filter designed in this thesis, transformation from lumped-element filter circuit to microwave structures could be achieved by generating the coupling coefficients of inter-coupled resonators and external quality factors of the input and output resonators using data from a full-wave electromagnetic field simulator instead of complicated calculation[1-4].

Transmission media for implementing filter include waveguide, coaxial lines, ceramic, printed circuit filter in microstrip, stripline, coplanar strip, etc. A hollow waveguide,

which may be in a rectangular or circular form, is a closed metal tube without a center conductor and can propagate TE or TM mode above a certain cutoff frequency. Waveguide resonators give good unloaded quality factor, which will result in filters with minimum insertion loss for a given fractional bandwidth. However, these filters have the disadvantages of being bulky in low frequency application and limited upper frequency range because of the possibility of higher-order mode. Parallel plate waveguide and Coaxial lines are types of TEM transmission lines. Because of the trend toward miniaturization and integration, microwave filters are constructed using planar transmission lines instead of waveguide and coaxial lines. Much smaller filters may be constructed using TEM or quasi-TEM printed circuit, which does not need a minimum cross-sectional dimension to ensure propagation. Striplines consist of a thin conducting strip centered between two wide conducting ground plates and the region between two ground plates is filled with a dielectric. Stripline can support TEM wave as well as higher order TE and TM modes; however, stripline is difficult in fabrication process. Microstrip can support quasi-TEM field and is one of the most popular types of planar transmission lines due to its ease in fabrication and integration with other microwave circuits [5].

The physical realizations of microwave filter include lumped element filter, directional coupled filter, parallel-coupled-line filter, hairpin filter, interdigital filter, combline filter, etc. lump-element filters have been applied to microwave system with their characteristics of high Q and smaller dimensions. At higher microwave frequencies, lumped realizations of filters are not usually practical because the wavelength becomes comparable to the physical dimensions of lump elements. For this reason, a variety of distributed-element forms realizations are used, where one or

more of the dimensions of the elements are comparable with the wavelength of operation. However, lump-element filters still play an important role to understand the distributed filters. Another important aspect for lump-element filters lie in the fact that most low-pass, high-pass, band-pass and band-stop distributed filters designs commence from lumped-element low-pass prototype filters which exhibit butterworth, chebychev, or other response like elliptic response.

Directional coupled filter consists of cascade of resonators coupled in series through the capacitive gap between two adjacent open ends. The coupling gaps may become quite small for a much larger fractional bandwidth. Directional coupled filter could be realized in coaxial, waveguide, microstrip and strip line forms and explained by the classic Cohn paper [6]. Parallel-coupled-line filters consist of resonators which are positioned so that adjacent resonators are parallel to each other to form the coupled multi-resonator filter [7]. Each individual resonator is affected by reactive loading from adjacent couplings and open-ended capacitive fringing. Parallel-coupled-line filter can be realized in stripline or in microstrip forms, etc. This parallel arrangement gives relatively large coupling for a given spacing between resonators, and thus, this filter structure is particularly convenient for constructing filters having a wider bandwidth as compared to the structure for the directional coupled filters. Though, compared with directional coupled, parallel-coupled-line filter reduces its length by a factor of 2, its excessive length still precludes their applications. Hairpin filters, firstly proposed by Cristal and Franco [8], are one of various types of folded parallel-coupled-line filter and preferable configuration in stripline or microstrip because ground connections are not need. In addition, they are very useful due to their compact structure. Though Hairpin filters may be obtained by folding the resonators

of parallel-coupled-line filter into a U shape, design equations for hairpin filter is not the same as that for parallel-coupled-line filter because folding the resonators will reduce the coupling between resonators. Open-loop resonator is comparable in size to a hairpine-line resonator and described by Hong and Lancaster [9]. Combline filter consists of an array of parallel resonators that are short circuited at one end with a loading capacitor at the other end. The resonators are oriented so that the short circuits are all on one side of the filter, and the capacitors all at the other side. The capacitive end loading of the resonators gives a useful size reduction compared with those that are based on a quarter-wave resonance, which make them more widely used. Interdigital filters are another option and consist of parallel- coupled quarter wavelength alternating between the short and open circuited ends.

### 3.2 Filter design

#### 3.2.1 Low-pass prototype and calculation of coupling coefficients

The bandpass filter is designed for central frequency of 9.06 GHz, with the 3dB fractional bandwidth of 10%. The passband insertion loss needed is less than 2dB and stop-band rejection larger than 20dB and designed by the Chebychev (equal ripple) low-pass prototype synthesis and transformation technique [4] [10]. To meet these requirements, the minimum number of order is 3. The low-pass prototype parameters, given for a normalized low-pass cutoff frequency 1 and a pass-band ripple of 0.1dB, are $g_0 = g_4 = 1$, $g_1 = g_3 = 1.0316$ and $g_2 = 1.1474$ [10].

Having obtained the low-pass parameters, the band-pass filter characterization could be performed by optimizing the external couplings of the first and last resonators as well as the internal coupling between adjacent resonators. The coefficients calculation of external quality factors of the resonators at the input ($Q_{e1}$) and output ($Q_{e2}$) and the internal coupling between adjacent resonators ($M_{1,2}$ , $M_{2,3}$) are presented below [9]:

$$Q_{e1} = \frac{g_0 g_1}{FBW} = 10.32 \qquad (3.1)$$

$$Q_{e2} = \frac{g_3 g_4}{FBW} = 10.32 \qquad (3.2)$$

$$M_{1,2} = \frac{FBW}{\sqrt{g_1 g_2}} = 0.09 \qquad (3.3)$$

$$M_{2,3} = \frac{FBW}{\sqrt{g_2 g_3}} = 0.09 \qquad (3.4)$$

Where FBW is the required fractional bandwidth. Using full-wave simulation software, Sonnet, these desired $Q_e$s and $M$ s can be mapped to physical dimensions of the filter.

### 3.2.2 Half-wavelength open-loop resonator

This filter is implemented by microstrip mix-coupled open-loop resonators, first proposed by Hong and Lancaster [11-13], with coupled feedline at input and output. The advantage of the open-loop resonator is the reduction in size.

Each of these three gold microstrip open-loop resonators has a perimeter approximate but less than a half-wavelength on a $LaAlO_3$ (LAO) dielectric substrate, which has a

relative dielectric constant of 24 and a thickness of 0.5mm. A general microstrip structure is shown in figure3.2 below.

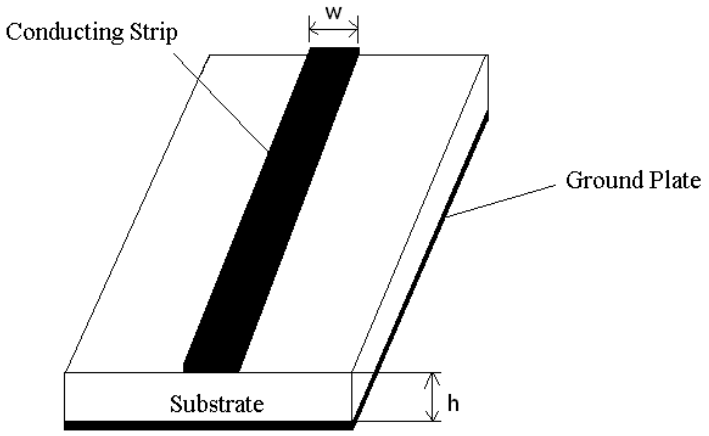


Figure3.2 General microstrip structure.

Though microstrip structure does not support pure TEM wave due to its inhomogeneous nature, quasi-TEM approximation can also be applied to this structure when the longitudinal components of the electromagnetic fields are much smaller than the transverse components. Therefore, microstrip structure could possess the parameter of effective dielectric constant $\varepsilon_{eff}$ , which is resulted from replacing the inhomogeneous air-dielectric media by a homogeneous media with the effective dielectric constant. With effective dielectric constant, it is possible to calculate the guided half-wavelength, i.e the perimeter of each resonator by the formula,

$$\lambda/2 = \frac{C}{2f\sqrt{\varepsilon_{eff}}} \tag{3.5}$$

where C is the light velocity in vacuum, $f$ is the electromagnetic wave frequency, simple closed form expressions for $\varepsilon_{eff}$ of the microstrip structure is[4],

$$\varepsilon_{eff} = \frac{\varepsilon_r + 1}{2} + \frac{\varepsilon_r - 1}{2}\left[\left(1 + 12\frac{h}{W}\right)^{-0.5} + 0.04\left(1 - \frac{W}{h}\right)^2\right] \quad \text{when } W/h \le 1 \qquad (3.6)$$

$$\varepsilon_{eff} = \frac{\varepsilon_r + 1}{2} + \frac{\varepsilon_r - 1}{2}\left(1 + 12\frac{h}{W}\right)^{-0.5} \quad \text{when } W/h \ge 1 \qquad (3.7)$$

where W is the strip width and h the dielectric substrate thickness.

In addition, due to the fact that the fringe field at the open end of the resonator will affect the resonant frequency of the resonator, the actual perimeter of the resonator will be shorter than the guided half wavelength. Therefore, more accurate model could be obtained using Full-wave electromagnetic field simulator. The dimension of the open-loop resonator decided by Sonnet simulator is shown in figure3.3 with a cross section of the planar $Ba_{0.5}Sr_{0.5}TiO_3$ thin film varactor.

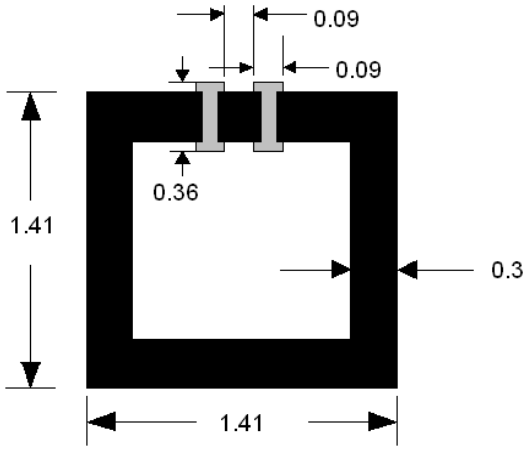


Figure3.3. Dimension of the open-loop resonator with unit mm

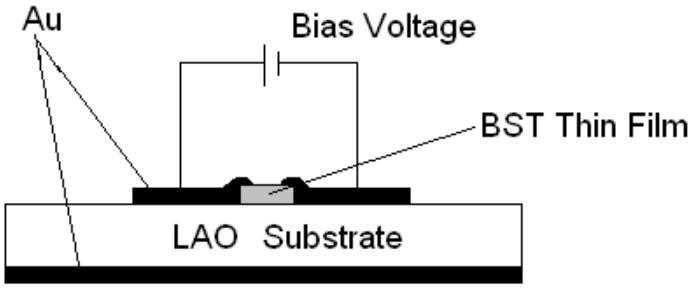


Figure3.4. Sideview of the planar $Ba_{0.5}Sr_{0.5}TiO_3$ varactor on LAO substrate.

The black area represents the gold circuit and grey area represents patterned $Ba_{0.5}Sr_{0.5}TiO_3$ thin film. Gold circuit is patterned on the top surface of the LAO ($10 \times 10 \times 0.5mm^3$) substrate together with a whole gold ground plate on the bottom of the LAO substrate to establish the microstrip structure. The line width is 0.3mm to make the current density uniform and thus ohm loss in conductor small. The thickness of the conducting metal is 4.5um, which is about 3-4 times of the skin depth at resonance frequency, to ensure uniformity of the electromagnetic fields of the filter.

### 3.2.3 Coupled feedline and external quality factor

There are generally two types of input/output coupling structures for coupled microstrip resonator filters, the tapped line and the coupled line structures.

(a) (b)

Figure3.5 (a) tapped line and (b) coupled line structures for input/output coupling.

In this filter, the input and output microwave signal is coupled to the resonator by the coupled line structure shown in figure3.5 (b). The 50 ohm width of the feedline could be calculated according to the following closed form expression [5],

$$Z_c = \frac{\eta}{2\pi\sqrt{\varepsilon_{eff}}} \ln\left(\frac{8h}{W} + 0.25\frac{W}{h}\right) \quad \text{for } W/h \le 1 \tag{3.8}$$

$$\text{or } Z_c = \frac{\eta}{\sqrt{\varepsilon_{eff}}}\left[\frac{W}{h} + 1.393 + 0.677\ln\left(\frac{W}{h} + 1.444\right)\right] \quad \text{for } W/h \ge 1 \tag{3.9}$$

Similarly, the width of the 50ohm feed line can also be modeled by electromagnetic field simulator. In this filter, the width of the coupled line is 0.18mm, resulting in an impedance of 50 ohm over the 0.5mm LAO substrate.

For the coupled line structure used in our filter, the coupling is dependent on the gap between feedline and resonator as well as the width of the feedline. For a fixed width of the feedline, the coupling and then external quality factors $Q_{e1}$ and $Q_{e2}$ are obtained by optimizing the spacing between feed line and resonator according to the method below [14].

Generally, the unloaded quality factor for a resonator can be defined as,

$$Q_u = 2\pi \frac{W}{P_L T_0} = \omega_0 \frac{W}{P_L} \tag{3.10}$$

where W is the total energy stored in resonator, $P_L$ is the average energy dissipation in the resonator, $T_0$ is the resonant period, $\omega_0$ is the resonant angular frequency.

The external quality factor, which describes the energy dissipation in the external circuit, is,

$$Q_e = \omega_0 \frac{W}{P_e} \tag{3.11}$$

where $P_e$ is the energy dissipation in the external circuit coupled to the resonator.

The coupling coefficient, which describes the relationship between energy dissipated in the resonator and the energy dissipated of the external circuit, can be expressed by

$$\beta = \frac{P_e}{P_L} = \frac{Q_u}{Q_e} \tag{3.12}$$

Therefore, the loaded quality factor is,

$$Q_L = \omega_0 \frac{W}{P_L + P_e} = Q_u \frac{1}{1+\beta} = Q_e \frac{\beta}{1+\beta} \tag{3.13}$$

$$\frac{1}{Q_L} = \frac{1}{Q_u} + \frac{1}{Q_e} \tag{3.14}$$

For a resonator coupled to n pieces of transmission lines, the relationship between the loaded quality factor and the unloaded quality factor is,

$$Q_u = \left(1 + \sum_{i=1}^{n} \beta_i\right) Q_L \tag{3.15}$$

By simulation or experiment, the loaded quality factor can be extracted from the Scattering parameters according to

$$Q_L = \frac{f_0}{\Delta f} \tag{3.16}$$

where $f_0$ is the resonant frequency and $\Delta f$ the half power bandwidth shown in figure3.6.

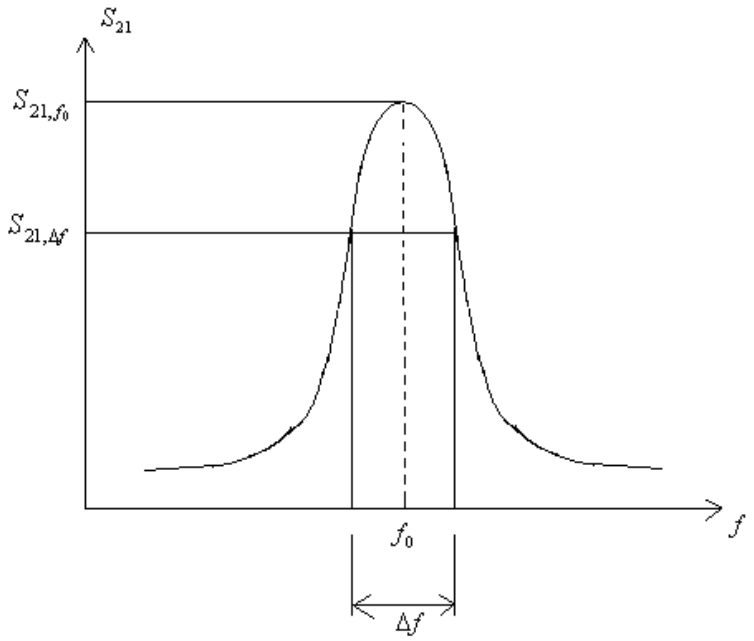


Figure3.6 Transmission scattering parameter of a typical resonator.

The $\Delta f$ can be determined by the scattering parameter $S_{21}$ according to the equation,

$$S_{21,\Delta f} = S_{21,f_0} - 3 \tag{3.17}$$

where $S_{21,f_0}$ is the value of $S_{21}$ at resonant frequency.

For this resonator with two coupled feedline at input and output,

$$Q_u = (1 + \beta_1 + \beta_2) \cdot Q_L \tag{3.18}$$

where $\beta_1$ and $\beta_2$ are the coupling coefficient of the resonator to the two ports respectively [11].

$$\beta_1 = \frac{1 - S_{11,f_0}}{S_{11,f_0} + S_{22,f_0}} \tag{3.19}$$

$$\beta_2 = \frac{1 - S_{22,f_0}}{S_{11,f_0} + S_{22,f_0}} \tag{3.20}$$

Altering the spacing between the feedline and the resonator and then extract the external quality factor $Q_e$ according to the method abovementioned, the relationship between spacing and $Q_e$ could be obtained and results are shown figure 3.7 below:

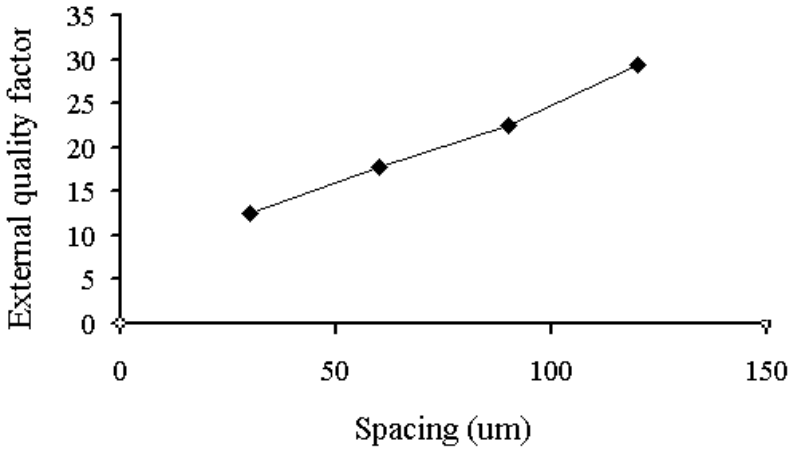


Figure3.7. Dependence of external quality factor on the spacing between feedline and resonator.

The optimized separation between resonator and feedline is 30um which gives, according to the relation shown above, external quality factors a value of 12.54. Narrowing the separation will make the value of $Q_e$ equal to10.32 and meet the

design requirement exactly, but limitation is set on the difficulty in fabrication process in lithography. The layout of the open-loop resonator is shown in figure 3.8.

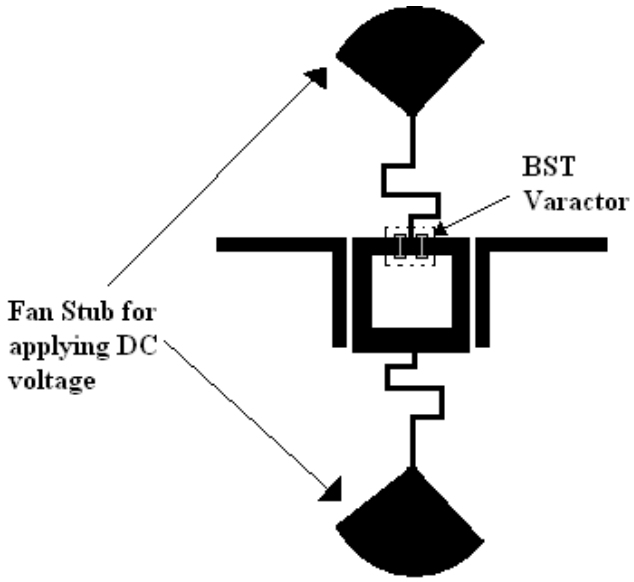


Figure3.8. Layout of open-loop resonator.

With the decided 30 um spacing between feedline and resonator, the modeled simulation result is shown in figure 3.9. The deep in 7.5GHz comes from the interaction of fan stubs.

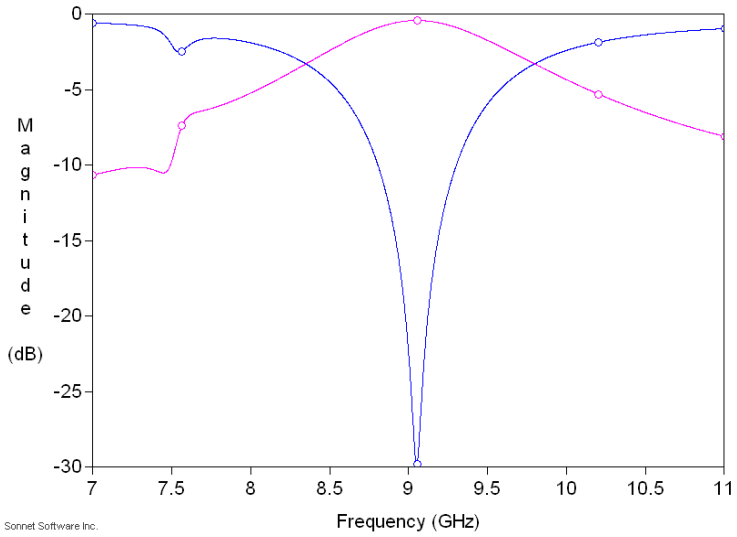


Figure3.9. Simulation result of open-loop resonator. Pink color curve represents transmission scattering parameter and blue color curve reflection scattering parameter.

### 3.2.4 Coupling of resonators and coupling coefficient

This coupled open-loop resonators bandpass filter is built by coupling the electromagnetic field of the resonators. Resonators before coupling have their resonant frequency determined by their self-capacitance and self-inductance. By placing these resonators next to each other, the electromagnetic field of each individual resonator will be affected by electromagnetic fields of other resonators, which could be described by the mutual capacitance and/or mutual inductance. These mutual couplings between resonators for any type of coupling structures can both enhance and reduce the stored energy of the resonators, which will change the resonant peak of individual resonator and therefore result in resonant mode splitting.

In general, there are three types of coupling structure, electric coupling, magnetic coupling and mix coupling for coupled open-loop resonators filter. These different types of coupling structure depend on the orientation of the resonator pairs, which will result in the different electromagnetic field distribution among the resonators.

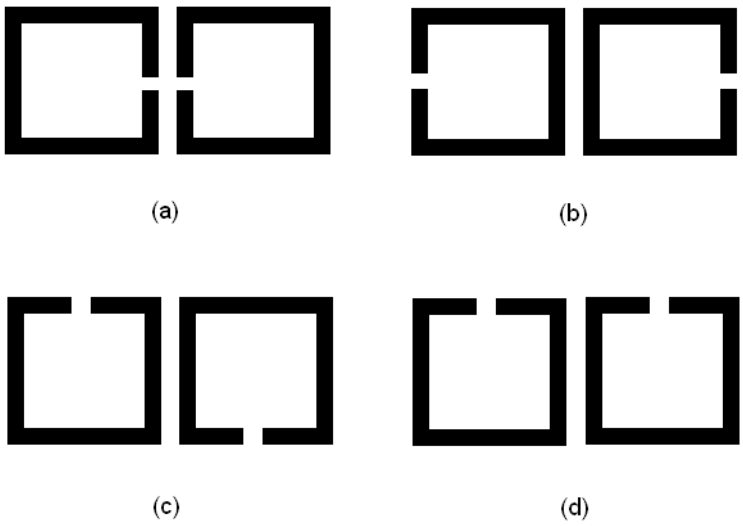


Figure3.10. (a) Electric coupling structure (b) Magnetic coupling structure (c) and (d) Mix coupling structure.

From the nature of the electromagnetic field distribution, at resonance, maximum electric field density lies between the open-gap of the resonator and the maximum magnetic field density is at the middle of the folded strip. Therefore, two open-loop resonators are oriented so that the open-sides are closely spaced as shown in figure3.10 (a) will be coupled by the electric coupling; the magnetic coupling will be obtained if the middle of the two resonators are placed proximately as shown in figure3.10 (b). Mix coupling will happen in figure3.10 (c) and (d) where the electric and magnetic field at the coupled sides have comparative strength so that both the electric and the magnetic couplings occur.

The extent of resonant mode splitting is related to the coupling coefficient and can be express by the equations below,

$$M_E = \frac{f_m^2 - f_e^2}{f_m^2 + f_e^2} \qquad (3\text{-}21)$$

for electric coupling structure in figure3.10 (a), where $f_e = \frac{1}{2\pi\sqrt{L(C + C_m)}}$ and $f_m = \frac{1}{2\pi\sqrt{L(C - C_m)}}$ , L and C are the self-inductance and self-capacitance of uncoupled resonators, $C_m$ is the mutual capacitance.

$$M_M = \frac{f_e^2 - f_m^2}{f_e^2 + f_m^2} \qquad (3\text{-}22)$$

for magnetic coupling structure in figure3.10 (b), where $f_e = \frac{1}{2\pi\sqrt{(L-L_m)C}}$ and $f_m = \frac{1}{2\pi\sqrt{(L+L_m)C}}$, L and C are the self-inductance and self-capacitance of uncoupled resonators, $L_m$ is the mutual inductance.

$$M_B = \frac{f_e^2 - f_m^2}{f_e^2 + f_m^2} \qquad (3\text{-}23)$$

for mix coupling structure in figure3.10 (c) and (d), where $f_e = \frac{1}{2\pi\sqrt{(L-L_m^{'})(C-C_m^{'})}}$ and $f_m = \frac{1}{2\pi\sqrt{(L+L_m^{'})(C+C_m^{'})}}$, L and C are the self-inductance and self-capacitance of uncoupled resonators, $L_m^{'}$ and $C_m^{'}$ are the mutual inductance and capacitance.

A schematic figure is shown in figure3.11.

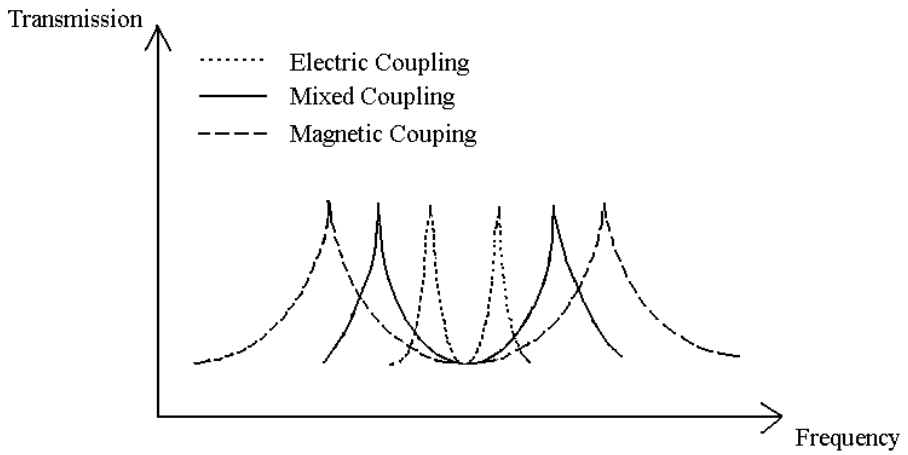


Figure3.11 Resonant mode splitting of three types of coupled open-loop resonators.

From the frequency response of scattering parameters of the coupled structure using sonnet simulator, there are two dominant resonant frequencies $f_1$ and $f_2$ for two coupled resonators, which are split off from their original resonance frequency due to the mutual electromagnetic field coupling and actually correspond to $f_e$ and $f_m$. For given dimension of resonators, the resonance frequency splitting and therefore the coupling coefficient M of two resonators are dependent on the spacing between the resonators. Therefore, it is possible to extract the coupling coefficients for different spacing between resonators and then optimize to the desired values.

The layout and simulation result of the modeled filter is shown below with 60um spacing, which is determined to give the value of $M_{1,2}$ and $M_{2,3}$ in equation 3.3 and 3.4. The simulation result has a good agreement with the specification for this filter.

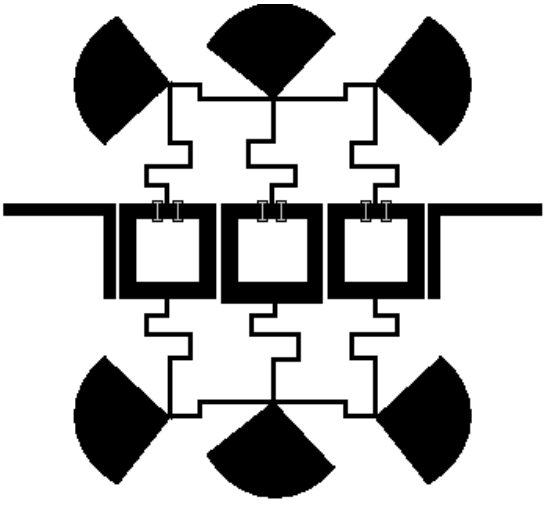

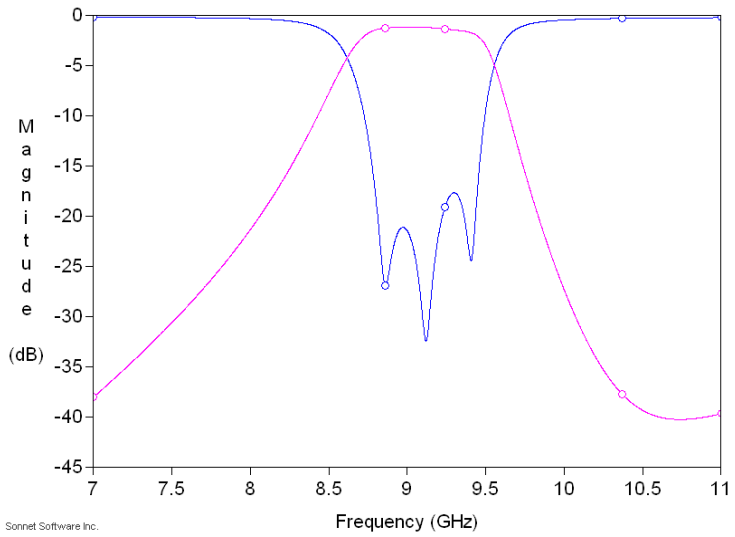


Figure3.12. Layout of the tunable bandpass filter. Black area represents the regions with gold; grey area represents the regions with $Ba_{0.5}Sr_{0.5}TiO_3$ thin film.

Figure3.13. The simulation results of the tunable bandpass filter. Curve of blue color represents $S_{11}$ parameter and curve of pink color represents $S_{21}$ parameter.

### 3.3 Fabrication of filter

At the first step, patches of $Ba_{0.5}Sr_{0.5}TiO_3$ thin films are patterned on the LAO substrate according to the fabrication process described in section 2.3 using soft mask designed by above-mentioned Sonnet simulation. On the top of the prepared patterned $Ba_{0.5}Sr_{0.5}TiO_3$ thin films, gold metallization with a thickness of 4.5um, which is used as conducting layer of the filter, is coated by RF sputtering and gold plating method according to section2.2. By the same process, the 4.5 um thickness gold also is grown on the bottom of the LAO substrate. The bottom of the LAO substrate has no $Ba_{0.5}Sr_{0.5}TiO_3$ thin films and

the gold layer on this side is only used as conducting metal to establish the microstrip structure. Then use photolithography method to obtain patterned gold circuit structure. In this process, wet etching is used to remove unusable chromium and gold respectively. A schematic process flow of the fabrication of the metallization of the filter is shown in figure3.14 below,

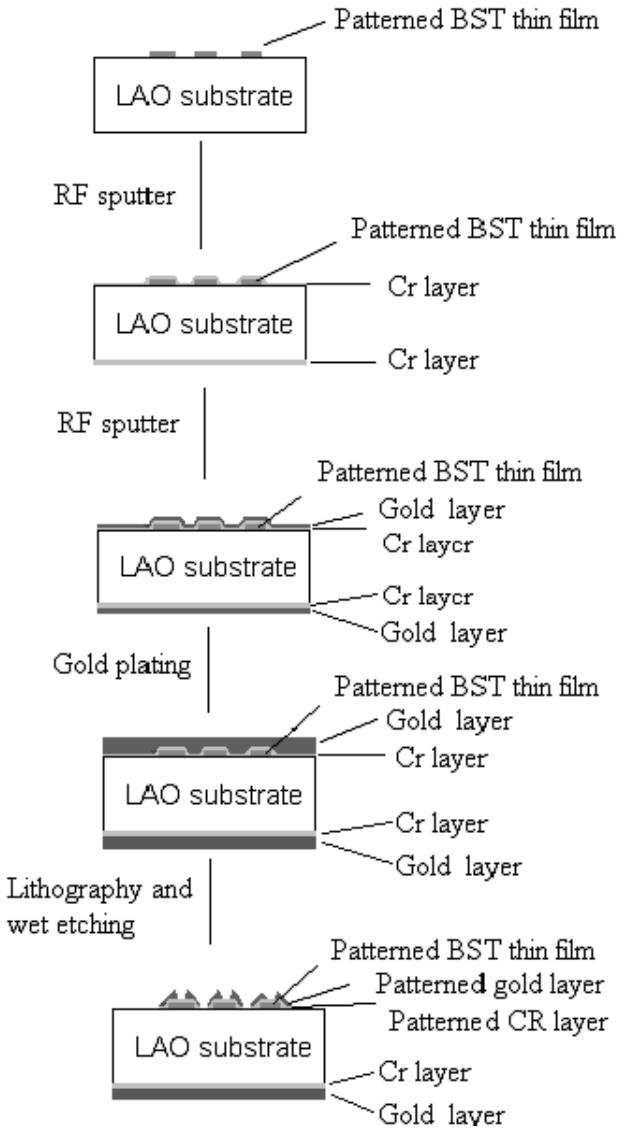


Figure3.14 Fabrication process flow for metal layer of filter.

### 3.4 Measurement results and discussion

The changing of scattering parameters of the filter are measured using the HP8722D vector network analyzer at room temperature with frequency ranging from 7GHz to 11GHz and bias voltage ranging from zero to 200 V.

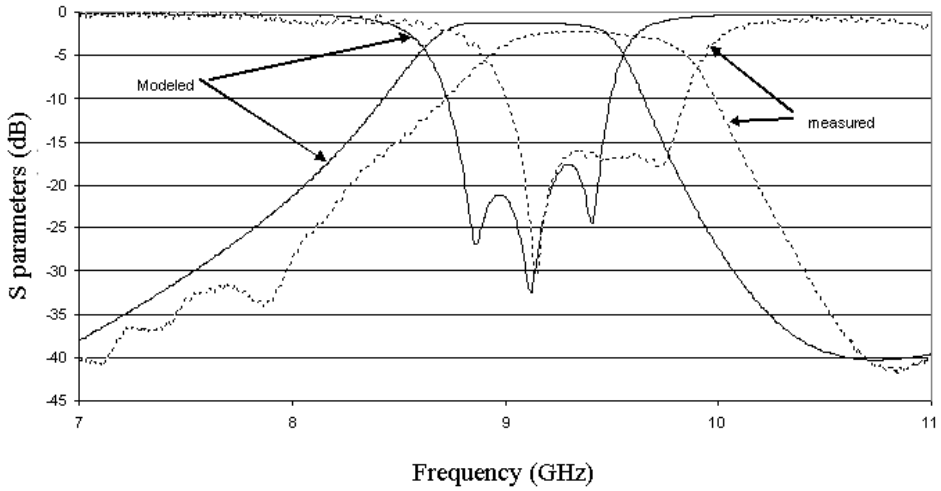


(a)

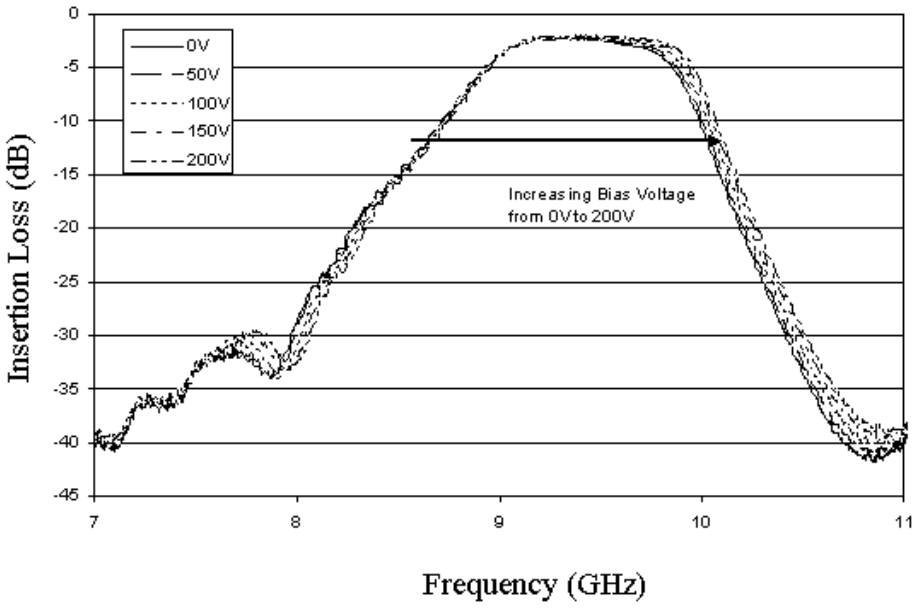


(b)

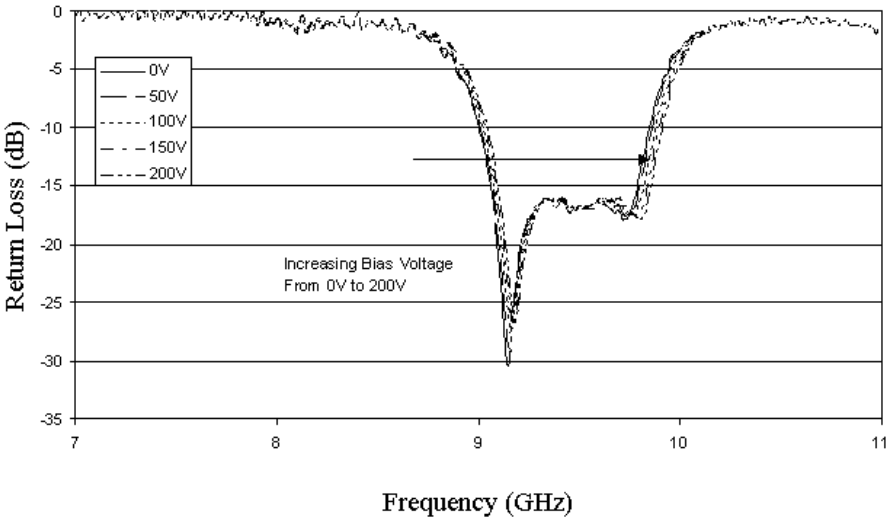


(c)

Figure3.15. Scattering matrix measured for the filter. (a) Comparison of modeled and measured data (b) Insertion loss versus bias voltage (c) Return loss versus bias voltage.

The measured filter characteristics are shown in figure3.15 (a) together with the caparison with the modeled one. The central frequency of this filter is 9.390GHz at unbiased state. The deviation of the central frequency from simulation result is due to two parts: one is the fabrication tolerance like over etching and the other is a thinner fabricated $Ba_{0.5}Sr_{0.5}TiO_3$ thin film of 300nm used than that of 500nm in the simulation. The smaller thickness results in decreased capacitance between the two end of the open loop resonator and hence an increased central frequency, but only affect little couplings between resonators.

Figure 3.15(b) shows the varying of the insertion loss of the filter with bias voltage. When a 200V bias voltage is applied, the central frequency increases to 9.465GHz with frequency tunability of 0.8 %. The tunablity of this filter is smaller than its HTS counterpart, which has a tunability of 1.6% [15].

For planar varactors used in both filters, the effective dielectric constant determines the tunability of varactors and then the tunability of the filter. This effective dielectric constant is a combination of the dielectric constant of three parts, the air above varactors, the $Ba_{0.5}Sr_{0.5}TiO_3$ thin film as well as the LAO substrate, and is dependent on the thickness and dielectric constant of these three materials.

In this filter, the thickness of the $Ba_{0.5}Sr_{0.5}TiO_3$ thin film is 300nm, which is smaller than the 400nm thick $Ba_{0.1}Sr_{0.9}TiO_3$ thin film used in the HTS one. Owing to the fact that BST thin film has much larger dielectric constant than those of air and LAO, thinner BST film

means less electric field being in the BST film and causes smaller effective constant and smaller tunability for this filter than those of the HTS one.

Furthermore, limitation in the tunability of this filter also comes from its quite wide gaps between varactor's electrodes (90um in this filter). The electrodes need to be as close as possible to maximize the electric field within the $Ba_{0.5}Sr_{0.5}TiO_3$ thin film. Therefore further improvement of the tunability can also be achieved by using high resolution lithography and hard mask.

In addition, according to the features of ferroelectrics, the higher dielectric constant the higher tunability, the smaller tunability of this filter may also attributes to the smaller dielectric constant of $Ba_{0.5}Sr_{0.5}TiO_3$ thin film used in this gold circuit filter than that of $Ba_{0.1}Sr_{0.9}TiO_3$ used in the HTS filter. Reports in literatures show that the relative dielectric constant of $Ba_{0.5}Sr_{0.5}TiO_3$ thin film at room temperature is from 1000 to 1800 [16-18] and that of $Ba_{0.1}Sr_{0.9}TiO_3$ thin film used in the HTS filter is about 1350 [15]. The variation of the values of dielectric constant of $Ba_{0.5}Sr_{0.5}TiO_3$ thin film reported by different groups is due to the different quality of BST thin film, which may depends on factors like defects, stress, and secondary phase introduced from deposition process, the quality of film-substrate interface, the thickness of the film, as well as other difference in device preparation process[19-20]. Further research could be performed to carefully measure the dielectric constants of $Ba_{0.5}Sr_{0.5}TiO_3$ thin film used in our lab.

The insertion loss in the passband is 2.27 dB without bias and decreases to 1.90 dB after a 200V voltage is applied. The decreasing of the insertion loss with applied voltage is due to increasing value of the unloaded quality factor of the resonators used in this filter. In order to measure the unloaded quality factor, resonator with the layout shown in figure3.8 is fabricated in this study and results show the unloaded quality factor increases from 34.12 to 47.88 when the state of the resonator varies from unbias to 200V bias state. Increasing value of unloaded quality factor can be explained by the decreasing of the loss tangent of the $Ba_{0.5}Sr_{0.5}TiO_3$ thin film with increasing bias voltage.

The insertion loss of this filter is larger than the HTS counterpart, which has the insertion loss of 1.6dB without bias and 0.35dB when 200VDC voltage is applied. Considering that the bandwidth of this filter is 10 % which is larger than the 5% bandwidth of the HTS filter, a similar room temperature filter with the same 5% bandwidth as the HTS one should have higher insertion loss than 2.27dB. It can be seen that when 200V bias voltage is applied, changing of insertion loss for the HTS filter is larger than that for the gold circuit filter. Since conducting loss in both filters is independent of electric field and dielectric loss is bias voltage dependent, it is reasonable to explain that the conducting loss in gold filter contributes more to the overall insertion loss than that of the HTS one.

### 3.4 Summary

In this chapter, a planar tunable microstrip bandpass filter is implemented. This filter had a good performance from 7GHz to 11GHz. The 3dB bandwidth is 10.22% and frequency tunability is 0.8%. The insertion loss at zero bias state is 2.27dB, stopband rejection

larger than 30dB and return loss larger than 15dB. Compared with HTS counterpart, this gold circuit filter demonstrates a smaller tunability. This smaller tunability can be attributed to the properties and thickness of the $Ba_{0.5}Sr_{0.5}TiO_3$ thin films used as well as the wide gap between varactor's electrodes. Improvements in $Ba_{0.5}Sr_{0.5}TiO_3$ film quality and lithography resolution could lead to better tunability. Although larger insertion loss in this gold circuit filter is still the main challenge, it is encouraging to see, from the experimental results, that insertion loss of the gold filter is only a little higher than that of HTS filter. In addition, materials chosen for microwave devices depend on the applications. Normal metals are suitable for room temperature applications and have the advantages of easy fabrication and implementation in industry as well as low cost for production and maintenance; high Tc superconductors are desirable for high Q if cryogenic requirements are acceptable. Therefore, there should be an optimal trade-off for different purpose of applications.

**Reference**

[1] Ian C. Hunter, Laurent Billonet, Bernard Jarry, and Pierre Guillon, Microwave filters-application and technology, *IEEE transactions on microwave theory and techniques*, Volume 50, Number 3, Pages 794-805 (2002)

[2] Ralph Levy and Seymour B. Cohn, A history of microwave filter research, design and development, *IEEE transactions on microwave theory and techniques,* Volume MTT-32, Number 9, Pages 1055-1067 (1984)

[3] Ralph Levy, Richard V. Snyder, and George Matthaei, Design of microwave filters, *IEEE transactions on microwave theory and techniques,* Volume 50, Number 3, pages 783-793 (2002)

[4] G. Matthaei, E.M.T.Jones and L.Young, Microwave filters, impedance-matching networks and coupling structures, Artech House Publishers (1980)

[5] David M.Pozar, Microwave Engineering, Wiley (1997)

[6] Seymour B. Cohn, Direct-Coupled-Resonator filters, *Proceedings of the IRE*, Volume 45, Issue 2, Pages 187-196 (1957)

[7] Seymour B. Cohn, Parallel-coupled transmission-line resonator filters, *IRE Transactions Microwave Theory Tech*niques, Volume MTT-6, Pages 223 – 231 (1958)

[8] Edward G. Cristal and Sidney Frankel, Hairpin-line and hybrid hairpin-line/half-wave parallel-coupled line filters, *IEEE Transactions on Microwave Theory and Techniques,* Volume. MTT-20, Pages 719-728 (1972)

[9] J.S. Hong and M.J. Lancaster, Canonical microstrip filter using square open-loop resonators, *Electronics Letters,* Volume 31, Number 23, Pages 2020-2022 (1995)

[10] Jia-Sheng. Hong, M.J.Lancaster, Microstrip filters for RF/Microwave applications, John Wiley & Sons, Inc (2001)

[11] Jia-Sheng Hong, and Michael J. Lancaster, Couplings of microstrip square open-loop resonators for cross-coupled planar microwave filters, *IEEE transactions on microwave theory and techniques,* Volume 44, Number 12, Pages 2099-2109 (1996)

[12] Jia-Sheng. Hong, M.J.Lancaster, Theory and experiment of novel microstrip slow-wave open-loop resonator filters, *IEEE transactions on microwave theory and techniques,* Volume 45, Number 12, pages 2358-2365 (1997)

[13] Jia-Sheng. Hong, M.J.Lancaster, Crooss-coupled microstrip hairpin-resonator filters, *IEEE transactions on microwave theory and techniques,* Volume 46, Number 1, pages 118-122 (1998)

[14] L.F.Chen, C.K.Ong and C.P.Neo, Microwave electronics measurement and materials characterization, John Wiley & Sons Ltd (2004)

[15] C Y Tan and C K Ong, Planar tunable HTS microwave filter with patterned ferroelectric thin film, *Superconductor science and technology,* Volume 19, Number 2, Pages 212-216 (2006)

[16] C. L. Chen, H. H. Feng, Z. Zhang, A. Brazdeikis, Z. J. Huang, W. K. Chu, and C. W. Chu, Epitaxial ferroelectric Ba0.5Sr0.5TiO3 thin films for room-temperature tunable element applications, *Applied physics letters* Volume 75, Number 3, Pages 412-414 (1999)

[17] Y. Gim, T. Hudson, Y. Fan, C. Kwon, A. T. Findikoglu, B. J. Gibbons, B. H. Park, and Q. X. Jia, Microstructure and dielectric properties of Ba1-xSrxTiO3 films grown on

LAalO3 substrates, *Applied physics letters,* Volume 77, Number 8, pages 1200-1202 (2000)

[18] X HZhu, L P Yong, H F Tian, W Peng, J Q Li and D N Zheng, The origin of the weak ferroelectric-like hysteresis effect in paraelectric Ba0.5Sr0.5TiO3 thin films grown epitaxially on LaAlO3, *Journal of physics: condensed matter,* Volume18, Pages 4709-4718 (2006)

[19] A.K.Tagantsev, V.O.Sherman, K.F. Astafiev, J.Venkatesh, and N.Setter, Ferroelectric Materials for Microwave Tunable Applications, *Journal of Electroceramics,* Volume 11, Pages 5-66 (2003)

[20] Xinhua Zhu, Jianmin Zhu, Shunhua Zhou, Zhiguo Liu, Naiben Ming, Shengguo Lu, Helen Lai-Wan Chan, and Chung-Loong Choy, Recent Progress of (Ba,Sr)TiO3 Thin Films for Tunable Microwave Devices, *Journal of Electronic Material,* Volume 32, Number 10, Pages 1125-1134 (2003)

# Chapter4:

# Microwave tunable coupled microstrip lines phase shifter with $Ba_{0.5}Sr_{0.5}TiO_3$ thin film varactors

Tunable microwave phase shifters are crucial components in phase array antennas. A phased array antenna consists of thousands of radiating elements and should be served by thousands of phase shifters, which are used to modify and control the width and angle of the steered radar beam. In this chapter, the design, fabrication and measurement of a coupled microstrip lines phase shifter using $Ba_{0.5}Sr_{0.5}TiO_3$ thin film varactors as tuning elements on LAO substrate are presented. The first part concerns the theory of coupled microstrip lines, followed by the explanation of balun circuit. The detail of phase shifter design is described in the second part. Fabrication process and measurement results are discussed in the last part.

## 4.1 Properties of coupled microstrip lines

Many types of phase shifter circuit topologies exist including lumped elements, transmission line, reflection type phase shifter, waveguide, etc. The differential phase shift capability of a tunable transmission line phase shifter lies on the fact that the phase velocity of an electromagnetic signal $V_p = \frac{1}{\sqrt{\varepsilon_{eff}\,\mu_{eff}}}$ can be tailored by changing the effective permittivity and/or the effective permeability of the circuit. As a result, the

insertion phase of a phase shifter for a given frequency $\varphi = \frac{\omega}{V_p} l = \omega l \sqrt{\varepsilon_{eff}\,\mu_{eff}}$ will become a function of effective permittivity and/or effective permeability.

Transmission line phase shifters using coplanar waveguide (CPW) lines periodically loaded with varactors have been investigated by several groups [1-3]. However, when the CPW phase shifters are integrated with circuits supporting balanced signals, additional transition circuit, which transform the unbalanced signal in CPW to the balanced signal, is needed. In this case, extra loss is introduced and the complexity of the circuit is increased. Therefore, coupled microstrip (CM) lines phase shifters are preferable for balanced circuits and will improve the flexibility of circuit design and integration [4-8]. Figure 4.1 illustrates the cross section of a pair of CM lines.

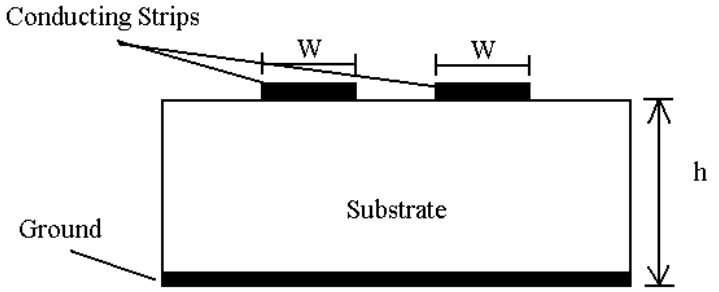


Figure4.1. Cross section of coupled microstrip lines.

Different from the single microstrip line, this CM lines structure support two quasi-TEM modes: the odd mode and the even mode shown in figure4.2 below.

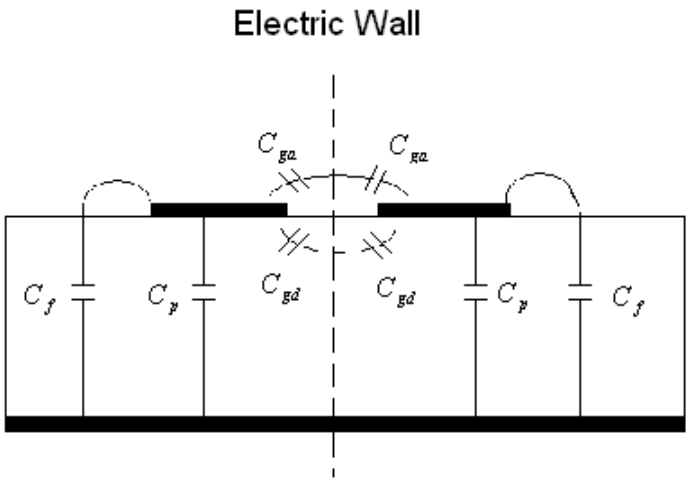


(a)

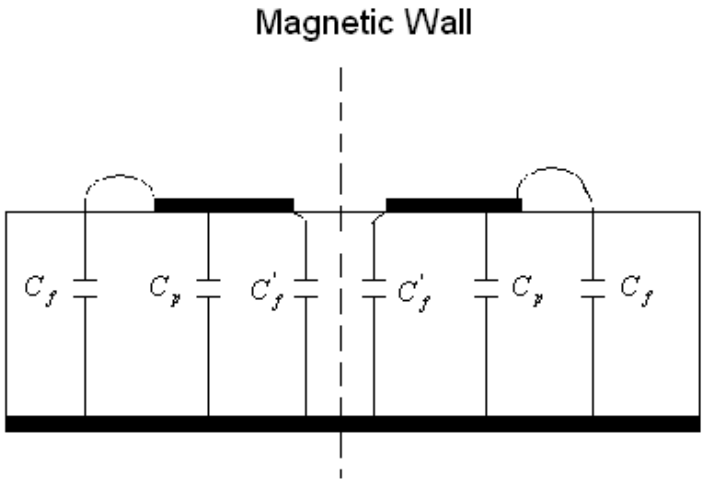


(b)

Figure4.2. Quasi-TEM modes of a pair of coupled microstrip lines: (a) odd mode (b) even mode.

For an odd mode excitation as shown in figure4.2 (a), the two microstrip lines posses the opposite voltage potentials or carry the opposite sign charges, resulting in the zero value of tangential electric field at the symmetry plane, which represents an electric wall. In the case for even mode excitation, shown in figure4.2 (b), the two microstrip lines contain the same voltage potentials or carry the same sign charges, indicating a zero value of tangential magnetic field at the symmetry plane, which is defined as a magnetic wall.

The odd and even mode capacitance $C_o$ and $C_e$ , as well as effective dielectric constant $\varepsilon_o$ and $\varepsilon_e$ could be expressed by,

$$C_o = C_p + C_f + C_{gd} + C_{ga} \tag{4.1}$$

$$C_e = C_p + C_f + C_f^{'} \tag{4.2}$$

$$\varepsilon_o = \frac{C_o}{C_o^a} \tag{4.3}$$

$$\varepsilon_e = \frac{C_e}{C_e^a} \tag{4.4}$$

Where $C_p$ represents the parallel plate capacitance between the strip and the ground plane, $C_f$ denotes the fringe capacitance for a single microstrip line as the absence of the other line, $C_f^{'}$ is the modification of $C_f$ due to the effect from another line. $C_{ga}$ and $C_{gd}$ in the formula for odd mode capacitance are the fringe capacitance for the air and dielectric regions between the gap of two microstrip lines. $C_e^a$ and $C_o^a$ are the even and odd mode capacitances when the dielectric is replaced by air.

### 4.2 Odd mode excitation of balun circuit

It can be seen from equation (4.1)-(4.4) that, in general, the phase velocity of coupled microstrip lines determined by the formula $V_p = \frac{1}{\sqrt{\varepsilon_{eff}\,\mu_{eff}}}$ are different for odd and even modes excitation due to the difference of effective dielectric constants. For the phase shifter designed in this work, the phase velocity of a signal can be more effectively tuned in the odd mode due to the fact that DC bias field is applied between the coupled lines and concentrates in the BST thin film. If the phase velocity is dominated by the even mode field, the microwave electric field is between the microstrip lines and the ground plane as shown in figure 4.2(b), the changing of phase velocity with applied bias voltage will be insignificant. In order to provide an odd mode excitation of the CM lines, a microstrip Marchand balun circuit [9] is adopted in this phase shifter. This balun can also work as an impedance matching network; this will be explained later. A schematic layout of the balun with its microstrip implementation is shown in figure4.3 below:

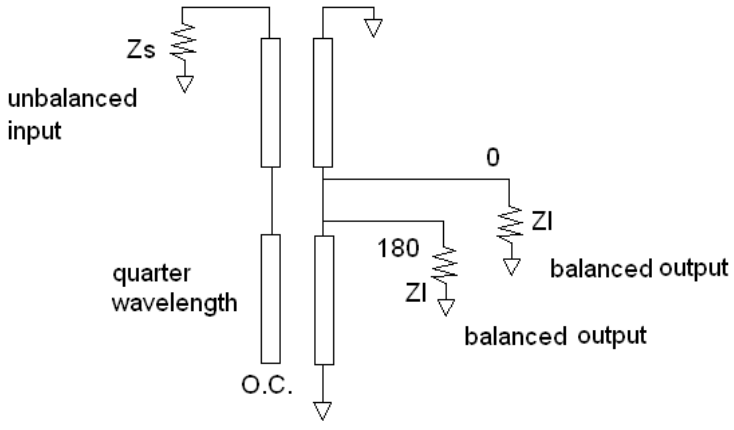


(a)

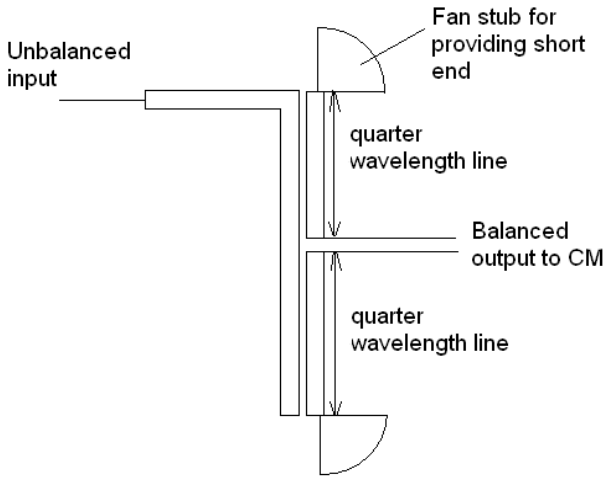


(b)

Figure4.3 (a) Schematic layout of a planar Marchand balun (b) microstrip implementation of the balun.

The balun consists of two pairs of parallel-coupled quarter wavelength lines connected in series. The signal referenced to ground at unbalanced input will be transformed into two signals with equal amplitude and a phase difference of 180° at output. Then these differential signals at balanced port of the balun will be fed to the inputs of the CM lines. By this means, the balun works as a transformer of odd mode excitation and a transmission stop circuit for even mode excitation.

## 4.3 Phase shifter design

### 4.3.1 Calculation of phase shift and tunability

This phase shifter comprises a high impedance ( $Z_0$ ) coupled microstrip lines periodically loaded with planar plate $Ba_{0.5}Sr_{0.5}TiO_3$ thin film varactors. The space between varactors is ΔL and it is also the unit cell length. The CM lines can be approximated as a lump inductance $L_0$ and capacitance $C_0$ in a unit cell. Discussed here and the following of this phase shifter are all for the odd mode excitation of CM. The substrate used is LAO, the same as that used in filter design in chapter3, which has a dielectric constant of 24 and thickness 0.5mm. A schematic structure of the CM lines phase shifter is shown in figure4.4 (balun circuit is not shown for clarity) with its simple equivalent circuits. For the sake of simplicity, lossless case is assumed.

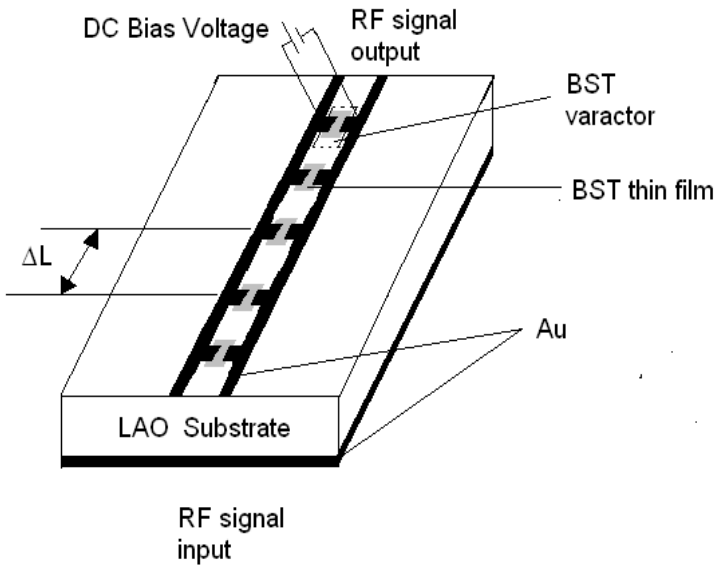


(a)

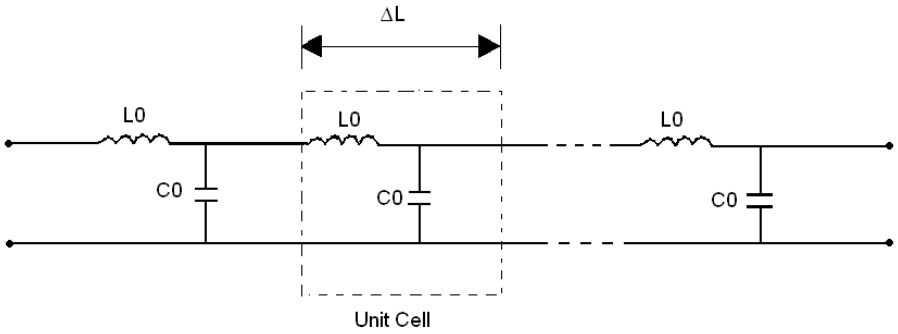


(b)

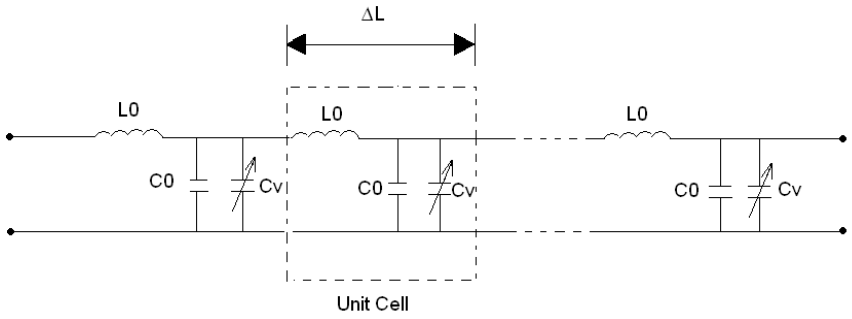


(c)

Figure4.4. Schematic structure of a CM phase shifter periodically loaded with $Ba_{0.5}Sr_{0.5}TiO_3$ thin film varactors and its circuit approximation (a) schematic layout (b) equivalent circuit of coupled lines before loaded with varactors (c) after loaded with varactors.

The characteristic impedance and propagation constant of the unloaded CM lines shown in figure 4.4(b) are presented below:

$$Z_0 = \sqrt{\frac{L_0}{C_0}} \qquad (4.5)$$

$$\beta_0 = \omega\sqrt{L_0 C_0} \qquad (4.6)$$

Where $L_0$ and $C_0$ represent distributed inductance and capacitance per unit length as shown.

After varactors with capacitance $C_{v1}$ at zero bias state are loaded periodically between the CM lines, as seen in the equivalent circuit of figure4.4(c), the capacitance per unit length is increased and the inductance per unit length for these coupled lines remains unchanged. The characteristic impedance, propagation constant and phase shift are,

$$Z_1 = \sqrt{\frac{L_0}{C_0 + C_{v1}/\Delta l}} \tag{4.7}$$

$$\beta_1 = \omega\sqrt{L_0(C_0 + C_{v1}/\Delta l)} \tag{4.8}$$

$$\varphi_1 = \omega l\sqrt{L_0(C_0 + C_{v1}/\Delta l)} \tag{4.9}$$

After a bias voltage of U is applied to the varactors, the corresponding characteristic impedance, propagation constant and phase shift are

$$Z_2 = \sqrt{\frac{L_0}{C_0 + C_{v2}/\Delta l}} \tag{4.10}$$

$$\beta_2 = \omega\sqrt{L_0(C_0 + C_{v2}/\Delta l)} \tag{4.11}$$

$$\varphi_2 = \omega l\sqrt{L_0(C_0 + C_{v2}/\Delta l)} \tag{4.12}$$

Where $C_{v2}$ is the capacitance of the varactors at bias state. From equation (4.9) and (4.12), it can be seen that since the capacitance of the loading varactors is electric field dependant, the properties of the loaded microstrip lines, such as the characteristic impedance, phase velocity, propagation constant, are functions of electric field. Therefore, it is possible to tailor the phase shift for a given length of transmission lines by

changing the bias electric field strength. The differential phase shift between two states then can be expressed by,

$$\Delta\varphi = \varphi_2 - \varphi_1 = \omega l(\sqrt{L_0(C_0 + C_{v2}/\Delta l)} - \sqrt{L_0(C_0 + C_{v1}/\Delta l)}) \qquad (4.13)$$

Therefore, tunability of the phase shifter between the two states can be calculated,

$$\frac{\Delta\varphi}{\Delta U} \approx \frac{2\pi f\sqrt{L_0}(C_{v1}/\Delta l)}{2\sqrt{C_0 + C_{v1}/\Delta l}} \frac{\Delta(C_{v2}/C_{v1})}{\Delta U} = \frac{\beta_0}{2}(\frac{Z_0}{Z_1} - \frac{Z_1}{Z_0}) \frac{\Delta(C_{v2}/C_{v1})}{\Delta U} \qquad (4.14)$$

### 4.3.2 HFSS simulator optimization of phase shifter

The design of a phase shifter is to obtain maximum phase shift with the lowest insertion loss and, meanwhile, maintain impedance matching at the ports. Hence, the first step for phase shifter optimization in this work is focus on achieving the maximum tunability. At any given frequency, the maximum tunability can be optimized by equation (4.14). The full wave electromagnetic simulation software, High Frequency Structure Simulator (HFSS) from Ansoft, is used to model the relationship between $\beta_0$ and the strips width and also $\beta_0$ with gap between strips.

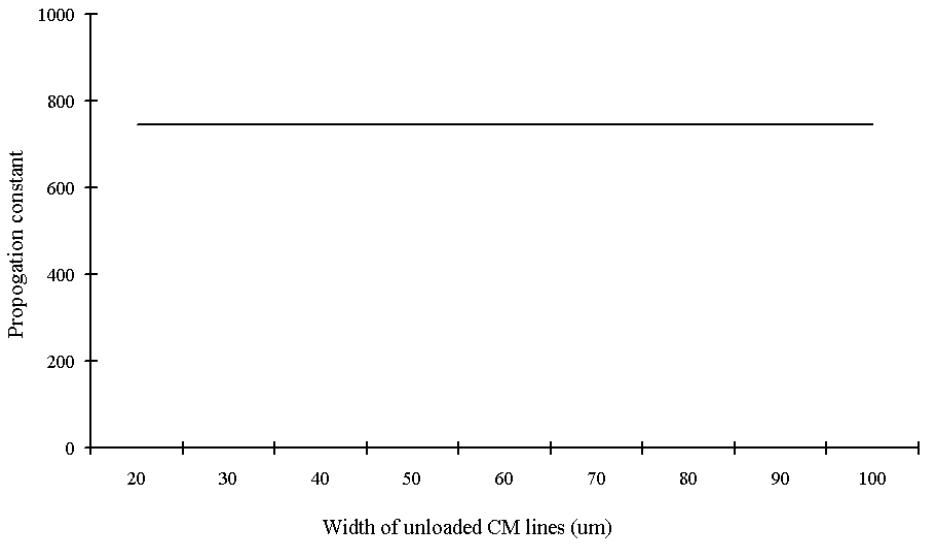


(a)

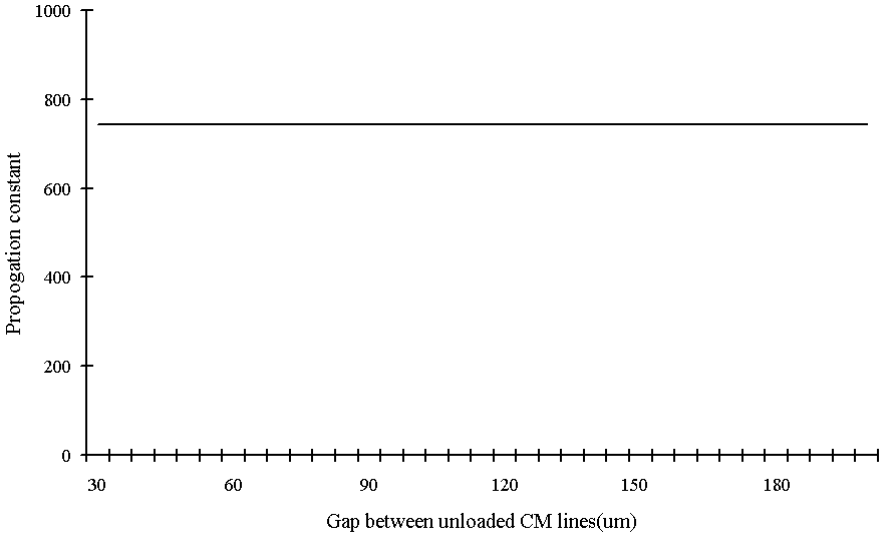


(b)

Figure4.5. Simulated relationship between propagation constant and (a) width of unloaded CM lines (b) gap between unloaded CM lines.

From figure4.5, the propagation constant $\beta_0$ remains unchanged (744.3 in this phase shifter) with the variation of the width of strips and gap between strips of unloaded CM

lines. Therefore, three factors are remaining in equation (4.14) to affect the tunability of the phase shifter, which indicate that increasing $\frac{\Delta(C_{v2}/C_{v1})}{\Delta U}$ , impedance of the unloaded CM lines $Z_0$ and/or decreasing the impedance of the loaded CM lines $Z_1$ will result in higher tunability.

The term $\frac{\Delta(C_{v2}/C_{v1})}{\Delta U}$ , which represents tunability of the varactors, is one of the three factors affecting the tunability of the phase shifter. For the $Ba_{0.5}Sr_{0.5}TiO_3$ thin film of fixed electric properties, reducing spacing between the two electrodes can maximize the tunability. Due to the limitation set by lithography resolution, 30 um spacing is used in this phase shifter.

Meanwhile, to attain maximum tunability of the phase shifter, the impedance of the unloaded CM lines $Z_0$ should be as large as possible.

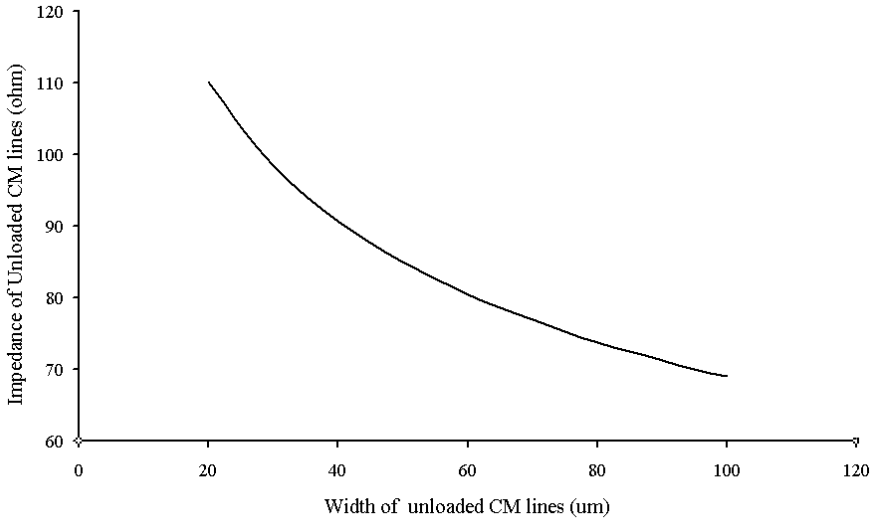

(a)

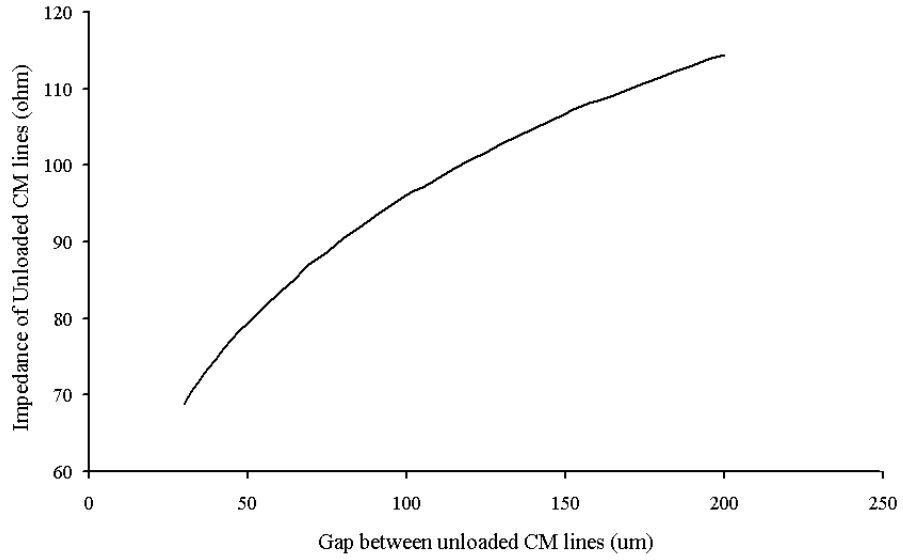


(b)

Figure4.6. Simulation of the changing of unloaded CM lines odd mode impedance with (a) strip width of CM lines (b) gap between CM lines.

As can be seen from figure4.6 (a), in order to obtain the largest impedance of unloaded lines $Z_0$, the strip width of the lines should be as small as possible. Here the 30um limitation for the strip width is also due to the lithography resolution. The gap chosen in this phase shifter is 110um. Although larger gap will benefit the tunability, it is still necessary to keep the two strips close enough in order to reduce the discontinuity caused by the stubs used for varactors loading.

In addition, maximum tunability could be obtained by minimizing the loaded CM lines impedance at unbiased state $Z_1$. However, $Z_1$ could not be too small because of the constraint imposed that $Z_1$ should be modeled to a value for impedance matching. As aforementioned, in this phase shifter, balun is used as impedance matching network. The impedance of loaded CM lines is $Z_1$, even and odd impedance of balun is $Z_e$ and $Z_o$, the impedance of microstrip feedline at unbalance port is $Z_{feed}$. The relationship between these four satisfies the equation [10],

$$\sqrt{Z_1 \bullet Z_{feed}} = \frac{2Z_e Z_o}{Z_e - Z_o} \qquad (4.15)$$

$Z_{feed}$ used is 50 ohm.

By altering the width of strips and gaps between strips in the balun, it's even and odd mode impedance $Z_e$ and $Z_o$ can be adjusted. Therefore, from equation (4.15), the impedance of the loaded CM lines will be changed. By this means, the balun provides tailored impedance matching between different impedances of circuits. HFSS simulation result of the relationship between balun dimension and loaded CM lines impedance $Z_1$ is shown in figure4.7 respectively.

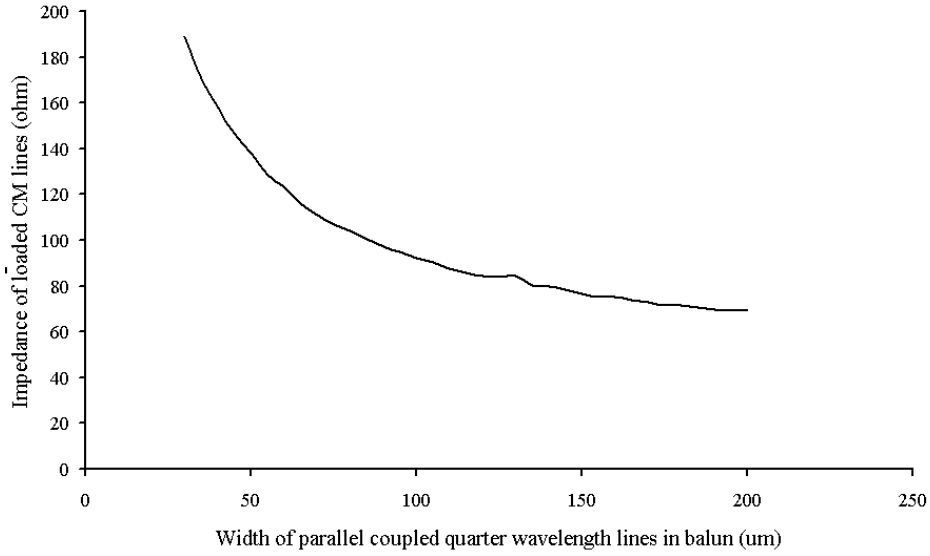


(a)

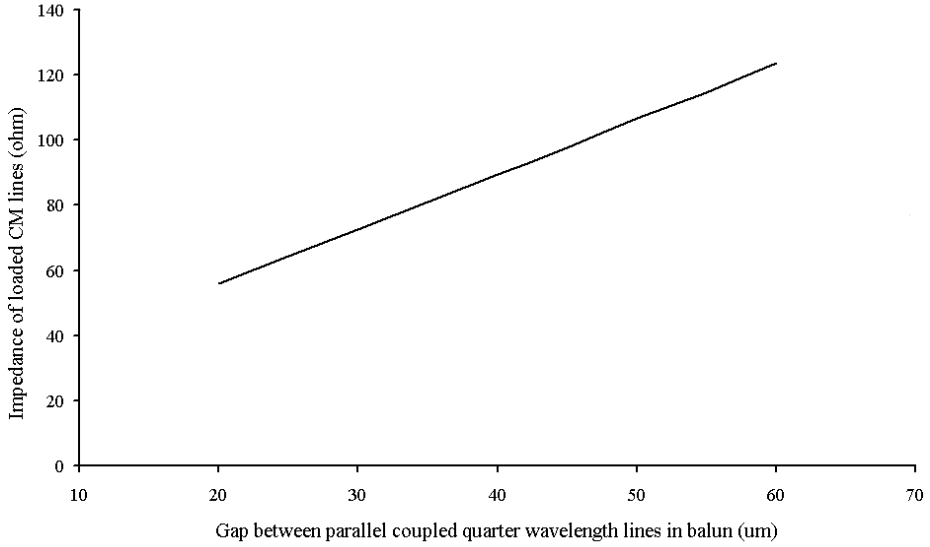


(b)

Figure4.7. Simulation result of the relationship between odd mode impedance of the loaded CM lines and (a) strip width of balun (b) gap between strips in balun.

From figure4.7 (a), the width of balun strips chosen in this phase shifter is 170um because further increasing the width could not significantly decrease the loaded CM lines impedance $Z_1$. Here, the gap between two coupled quarter wavelength strips of balun is chosen to be 30um and also is limited by the lithography resolution. This dimension of the balun provides impedance transforming between 50 ohm microstrip feedline and 72ohm loaded CM lines. Further narrowing the gap between balun's strips will decrease the impedance of the loaded CM lines and thus increase the tunability. However, 30um is the highest resolution of our commercial soft mask. Therefore, these conflicting requirements involve a compromise among the tunability and impedance matching.

The whole structure of the coupled microwave phase shifter without balun circuit is simulated by HFSS and, by altering the dimension of the $Ba_{0.5}Sr_{0.5}TiO_3$ thin film varactor and the unit cell length of the modeled structure to adjust the capacitance of $Ba_{0.5}Sr_{0.5}TiO_3$ thin film varactors, the loaded CM lines impedance is optimized to be 72 ohm. The simulation result is shown in figure4.8 (a) with the final phase shifter dimension in figure4.8 (b).

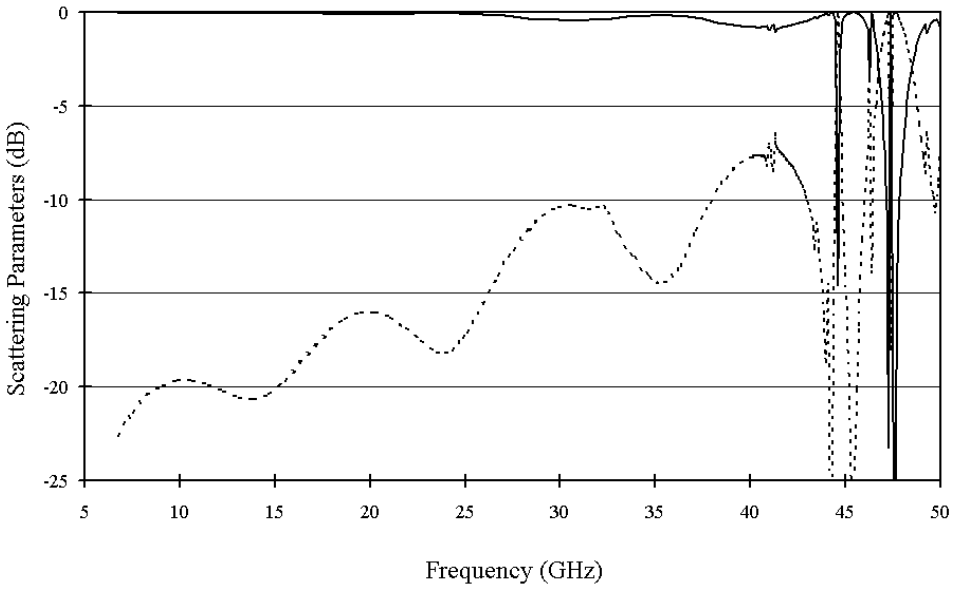
Scattering Parameters (dB)
0
-5
-10
-15
-20
-25
5
10
15
20
25
30
35
40
45
50
Frequency (GHz)

(a)

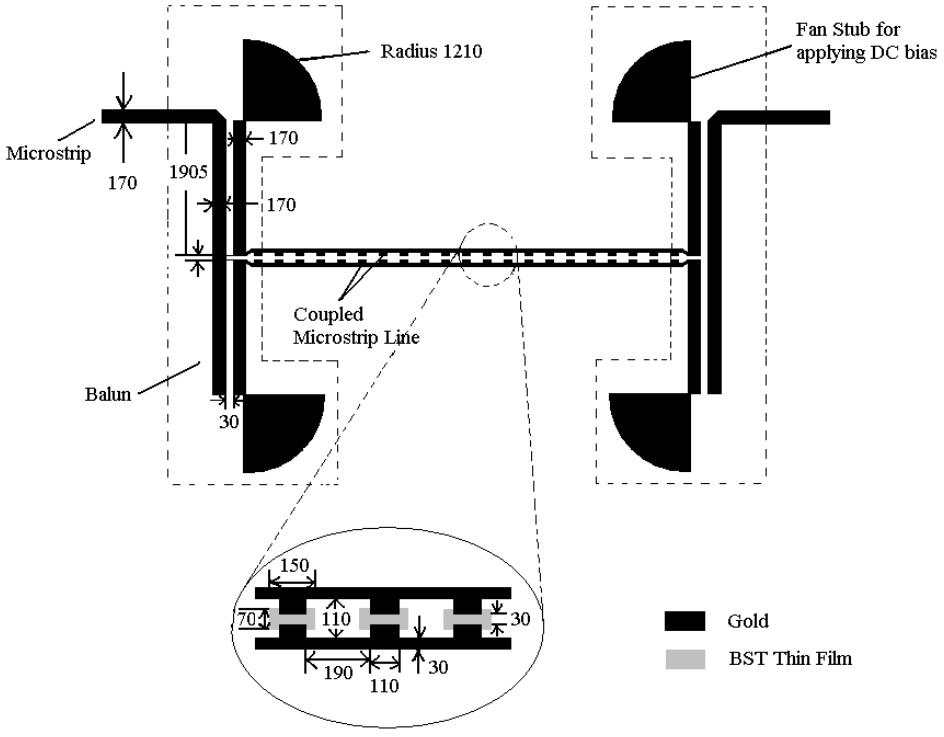
Radius 1210
Fan Stub for
applying DC bias
Microstrip
170
170
1905
170
Coupled
Microstrip Line
Balun
30
150
70
110
30
190
110
30
Gold
BST Thin Film

(b)

Figure4.8. (a) Simulation result of the modeled phase shifter without balun circuit, solid line represents transmission scattering papameter, dashed line represents reflection scattering parameter (b) layout of the phase shifter with dimension unit um.

### 4.4 Fabrication of phase shifter

Basic fabrication process of this phase shifter is similar to the filter in chapter3 and follows the same fabrication flow except for the different designed mask for patterns of thin film and conducting metal.

### 4.5 Measurement results and discussion

The performance of the CM phase shifter at room temperature is evaluated by measuring the scattering parameters at the frequency range from 6GHz to 14GHz using the HP 8722D vector network analyzer at room temperature. The measurement results of the differential phase shift, insertion loss and return loss of the phase shifter at DC bias from 0V to 200V are shown in Figure4.9 below.

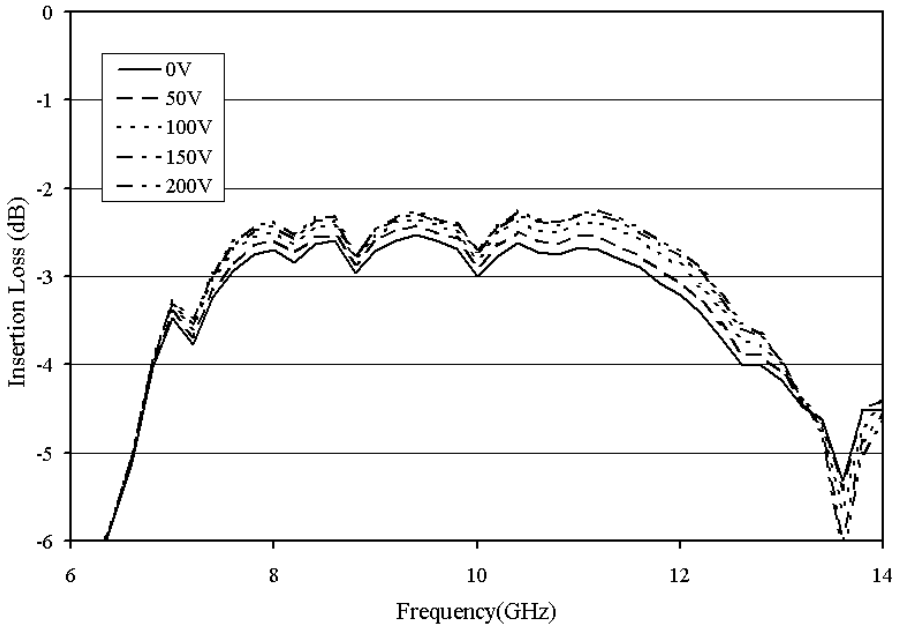
0
-1
-2
-3
-4
-5
-6
0V
50V
100V
150V
200V
Insertion Loss (dB)
6
8
10
12
14
Frequency(GHz)

(a)

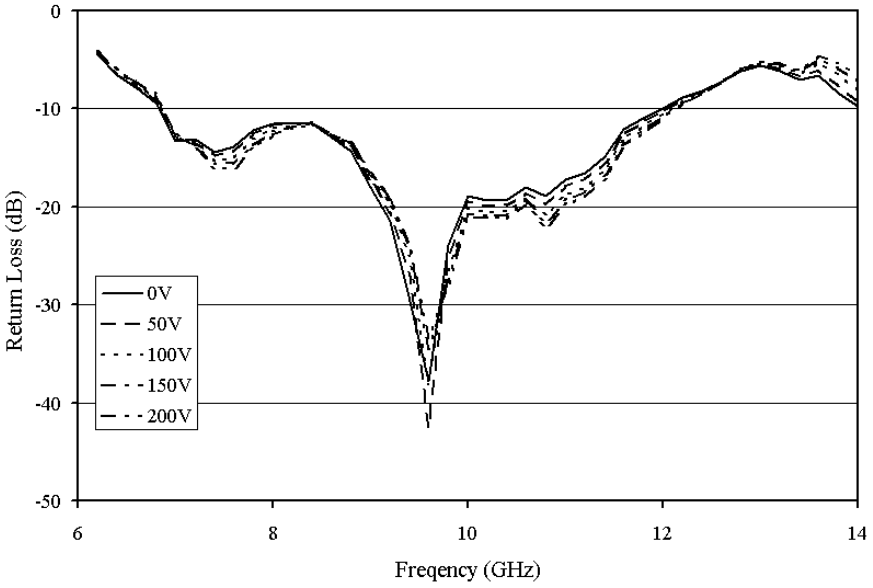
0
-10
-20
-30
-40
-50
0V
50V
100V
150V
200V
Return Loss (dB)
6
8
10
12
14
Freqency (GHz)

(b)

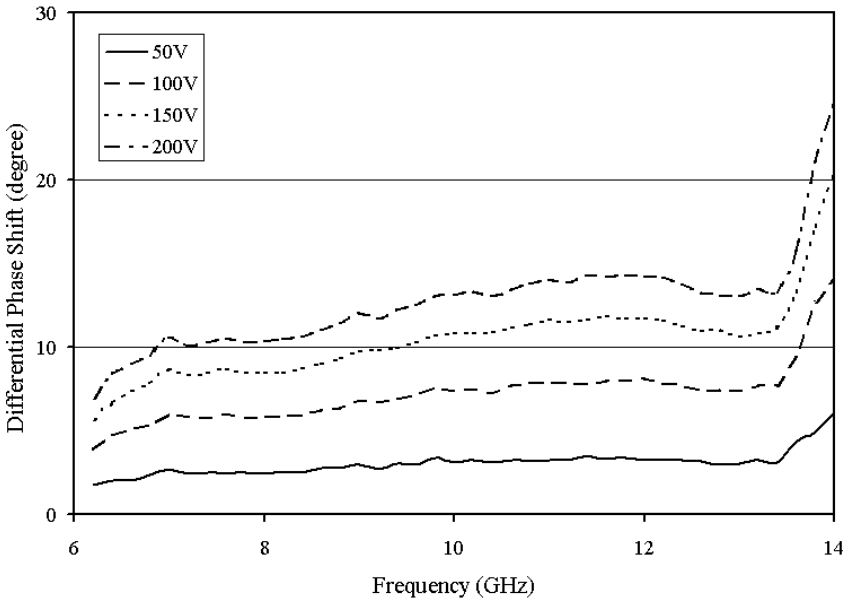


(c)

Figure4.9. Measured scattering parameters (a) insertion loss (b) return loss (c) differential phase shift of the coupled microstrip lines phase shifter with frequency.

Figure4.9 (a) and (b) shows the insertion loss of the phase shifter at bias voltage from 0V to 200 in steps of 50V. The maximum insertion is less than 3dB at frequency from 8GHz to 12GHz with the return loss better than 10dB at all states. The differential phase shift with respect to the unbiased state is shown in figure4.9 (c). This phase shifter has a 15 degree phase shift at 200 DC biases, which corresponds to a figure of merit of 5°/dB. The differential phase shift is limited in this phase shifter by the wide spacing of $Ba_{0.5}Sr_{0.5}TiO_3$ thin film varactor‘s electrodes. Thus, the phase shift will be improved by narrower spacing using high resolution lithography technique. Meanwhile, differential

phase shift can be improved by using further narrower transmission line strips. However, narrow strips will result in extra insertion loss for the gold circuit.

### 4.6 Summary

In this chapter, an analog phase shifter using $Ba_{0.5}Sr_{0.5}TiO_3$ thin film varactors periodically loading high impedance coupled microstrip lines is designed, fabricated and measured. The phase shifter has a good phase shift nearly 15 degree at 200V DC bias. The insertion loss is less than 3dB and return loss greater than 10 dB at the frequency range from 8GHz to 12GHz.

**Reference**

[1] O.G. Vendik., E.F. Carlsson., P.K. Petrov., R.A. Chakalov., S.S. Gevorgian. and Z.G. Ivanov, HTS/ferroelectric CPW structures for voltage tunable phase shifters, *Microwave Conference and Exhibition, 1997 27th European*, Volume1, Pages196-202 (1997)

[2] Gevorgian.S.S, Kaparkov.D.I and Vendik.O.G, Electrically controlled HTSC/ferroelectric coplanar waveguide, *IEE Proceedings, Microwaves, Antennas& Propagation*, Volume141, Number 6, Pages 501-503(1994)

[3] Yu Liu, Amit S. Nagra, Erich G. Erker, Padmini Periaswamy, Troy R. Taylor, James Speck, and Robert A. York, BaSrTio3 interdigitated capacitors for distributed phase shifter applications, *IEEE Microwave and Guided Wave Letters*, Volume10, Number 11, Pages 448-450 (2000)

[4] F. W. Van Keuls, R. R. Romanofsky, D. Y. Bohman, M. D. Winters, F. A. Miranda, C. H. Mueller, R. E. Treece, T. V. Rivkin, and D. Galt, (YBa2Cu3O7-σ, Au)/SrTiO3/LaAlO3 thin film conductor/ferroelectric coupled microstripline phase shifter for phased array applications, *Applied Physics Letters*, Volume 71, Pages 3075-3077 (1997)

[5] F. W. Van Keuls, C. H. Mueller, F. A. Miranda, and R. R. Romanofsky, Room temperature thin film BaxSr1-xTiO3 Ku-Band coupled microstrip phase shifters: effects of film thickness, doping, annealing and substrate choice, *Microwave Symposium Digest, 1999 IEEE MTT-S International*, Volume 2, Pages 737-740 (1999)

[6] F. W. Van Keuls, R. R. Romanofsky, and F. A. Miranda, Several microstrip-based conductor/thin film ferroelectric phase shifter designs using (YBa2Cu3O7- σ, Au)/SrTiO3/LaAlO3 structures, *Integrated Ferroelectrics*, Volume 22, Pages 373-381 (1998)

[7] F. W. Van Keuls, R. R. Romanofsky, N. D. Varaljay, F. A.Miranda, C. L. Canedy, S. Aggarwal, T. Venkatesan, and R. Ramesh, A Ku-band gold/BaxSr1-xTiO3/LaAlO3

conductor/thin-film ferroelectric microstrip line phase shifter for room temperature communications applications, *Microwave and Optical technology Letters*, Volume 20 Number 1, Pages 53-56 (1999)

[8] Robert R. Romanofsky, Jennifer T. Bernhard, Frederick W. Van Keuls, Félix A. Miranda, Gregory Washington, and Chadwick Canedy, K-Band Phased Array Antennas Based on Ba0:60Sr0:40TiO3 Thin-Film Phase Shifters, *IEEE transactions on microwave theory and techniques*, Volume 48, Number 12, Pages 2504-2510 (2000)

[9] Marchand. N, Transmission line conversion transformers, *Electronics*, Volume 17, Pages 142-145 (1944)

[10] Yoke Choy Leong, Kian Sen Ang, and Chee How Lee, A derivation of a class of 3-port baluns from symmetrical 4-portnetworks, *Microwave Symposium Digest, 2002 IEEE MTT-S International*, Volume 2, Pages 1165-1168 (2002)

# Chapter5:

# Bismuth zinc niobate thin film and its varactors

This chapter presents a study concerning the dielectric properties of $Bi_{1.5}Zn_{1.0}Nb_{1.5}O_7$ thin film for microwave tunable devices applications. The structure of bismuth zinc niobate (BNZ) material is introduced first. In the second part, crystallization and morphology of the $Bi_{1.5}Zn_{1.0}Nb_{1.5}O_7$ thin films studied by X-ray diffraction (XRD) and Scanning Electron Microscope (SEM) are presented. Microwave characterization of varactor performance and thin film dielectric properties are explained and discussed in the last part.

## 5.1 Introduction to $Bi_{1.5}Zn_{1.0}Nb_{1.5}O_7$ thin film

Generally, two phases in ternary oxide of bismuth zinc niobate system are of interests for high frequency dielectrics depending on composition and belong to the general family $(Bi_{3x}Zn_{2-3x})(Zn_xNb_{2-x})O_7$ , where x=1/2 for $Bi_{1.5}Zn_{1.0}Nb_{1.5}O_7$ with cubic pyrochlore phase and x=2/3 for $Bi_2Zn_{2/3}Nb_{4/3}O_7$ with monoclinic zirconnolite phase. Composition is a key factor to affect the crystal structure and dielectric properties of BZN thin films. Cubic pyrochlore phase $Bi_{1.5}Zn_{1.0}Nb_{1.5}O_7$ have attracted much attention as tuning element for microwave tunable devices due to its properties of medium relative permittivity in the range of 150-200, dielectric loss in an order of $10^{-3}$ at room temperature [1-7]. A much lower loss tangent of $5\times10^{-4}$ at 1MHz was reported by Jiwei et al and electric field

tunability up to 55% under an applied bias field of 2.4MV/cm at room temperature [8]. In contrast, $Bi_2Zn_{2/3}Nb_{4/3}O_7$ shows small dielectric constant about 80 and a little electric field dependence [1-2].

An ideal oxide pyrochlore structure, which represents a family of phase isostructural to the mineral pyrochlore $(NaCa)(NbTa)O_6F/(OH)$, has the general formula of $A_2B_2O_7$ with four crystallographically nonequivalent kinds of atom and often described by $B_2O_6 \cdot A_2O$. This implies that pyrochlore structure consists of two types of cation coordination polyhedron: $BO_6$ octahedra and $A_2O'$ tetrahedral. In the $B_2O_6$ octahedral sub-structure, the B cation is sixfold coordinated with oxygen to construct octahedra. $A_2O'$ tetrahedra sub-structure consists of an $A_2O'$ array of oxygen-centered tetradra, where the $O'$ anion is tetrahedrally coordinated by 4 A cations.

Investigations of $Bi_{1.5}Zn_{1.0}Nb_{1.5}O_7$ bulk ceramics in $Bi_2O_3$ - $ZnO$ - $Nb_2O_5$ system are consistent with a cubic pyrochlore structure (space group $Fd\overline{3}m$) with a=1.056nm [9-10], implying that $Zn^{2+}$ can occupy both A site and B site, while large radius $Bi^{3+}$ occupies the A site and small radius $Nb^{5+}$ trends to occupy B site. Local deviations from ideal pyrochlore unit cell structure and symmetry are also indicated, which emphasizes that O' and Bi/Zn sites in the $A_2O'$ network are displaced, with six possible positions for Bi/Zn and twelve for O' sites, to low symmetry positions [11-12]. This kind of displacive disorder of Bi/Zn and O' ions result in more polar modes than those for ideal pyrochlore

arrangement and may have effects on the high dielectric constant of the cubic pyrochlore $Bi_{1.5}Zn_{1.0}Nb_{1.5}O_7$ [13-14]

## 5.2 Crystalline structure and morphology of $Bi_{1.5}Zn_{1.0}Nb_{1.5}O_7$ thin films

For later study, $Bi_{1.5}Zn_{1.0}Nb_{1.5}O_7$ thin films are deposited on commercial (111) platinum coated silicon substrate (Pt (200nm)/Ti (20nm)/SiO2 (500nm)/Si) and (001) LAO single crystal substrate by pulsed laser deposition techniques according to parameters described in chapter2.

### 5.2.1 Crystallization of $Bi_{1.5}Zn_{1.0}Nb_{1.5}O_7$ thin films

The phase composition and crystallization of the $Bi_{1.5}Zn_{1.0}Nb_{1.5}O_7$ films are studied by an X-ray diffractometer (XRD) with CuKa radiation. Figure5.1 shows the x-ray diffraction patterns of $Bi_{1.5}Zn_{1.0}Nb_{1.5}O_7$ thin films deposited on the two substrates.

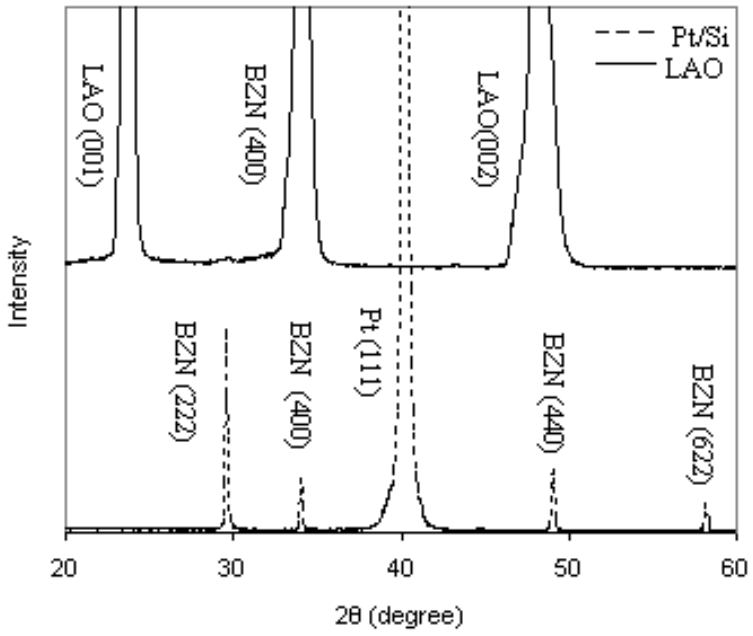


Figure5.1. XRD patterns of $Bi_{1.5}Zn_{1.0}Nb_{1.5}O_7$ films on Pt/Si and LAO substrates.

XRD results show that $Bi_{1.5}Zn_{1.0}Nb_{1.5}O_7$ thin films on both substrates are crystalline with a pure cubic pyrochlore phase, which is consistent with reports of other literatures [1-4]. It is necessary to mention that the intensity ratios of the film diffraction are different on these two substrates. $Bi_{1.5}Zn_{1.0}Nb_{1.5}O_7$ film on Pt/Si substrate shows a random oriented polycrystalline texture structure with no strong preferred orientation. (222), (400), (440) and (622) diffraction peaks of $Bi_{1.5}Zn_{1.0}Nb_{1.5}O_7$ cubic pyrochlore structure appear in the sample on Pt/Si substrate and the relative intensity of the (222) diffraction peak at 2θ=29.3° is somewhat higher than other peaks. However, $Bi_{1.5}Zn_{1.0}Nb_{1.5}O_7$ film on LAO substrate exhibits only a (400) main diffraction peak, indicating a strong preference for (400) orientation. L Z Cao et al also reported in his literature the deposition of (400) orientation of $Bi_{1.5}Zn_{1.0}Nb_{1.5}O_7$ thin film on STON substrate [15]. This may suggest that

some single crystal substrates would likely be desirable than the Pt/Si substrate with no orientation for depositing oriented $Bi_{1.5}Zn_{1.0}Nb_{1.5}O_7$ thin film.

### 5.2.2 Morphology of $Bi_{1.5}Zn_{1.0}Nb_{1.5}O_7$ thin films

The surface and cross-section morphology of the films are characterized by scanning electron microscope (SEM, JEOL JSM-6700F) equipment.

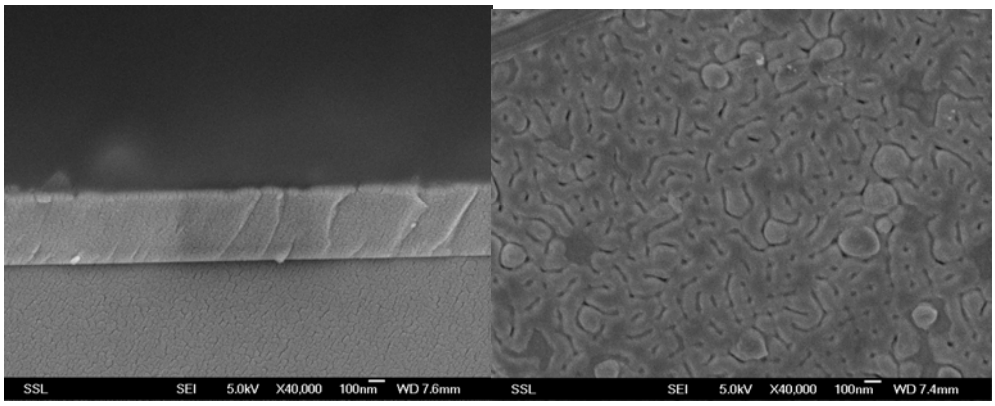


(a)

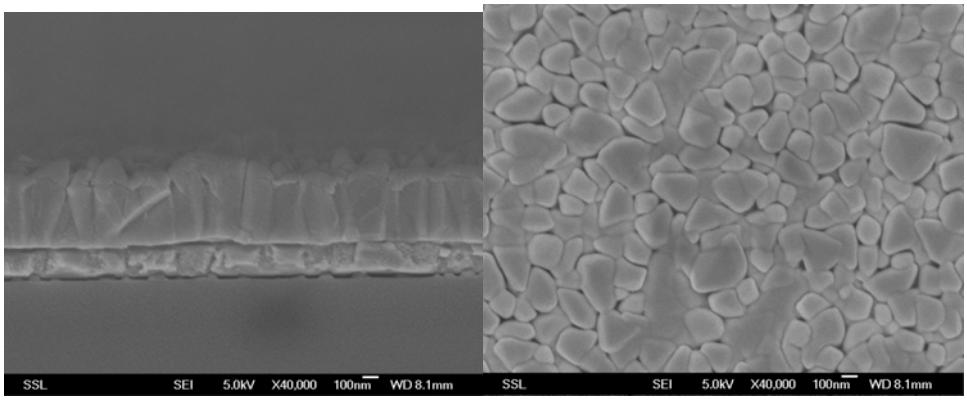


(b)

Figure5.2. SEM cross-section and surface morphologies of $Bi_{1.5}Zn_{1.0}Nb_{1.5}O_7$ thin films on (a) LAO and (b) Pt/Si substrates.

It is demonstrated in figure5.2 that crack-free and uniform $Bi_{1.5}Zn_{1.0}Nb_{1.5}O_7$ thin film can be grown on both substrates, which is consistent with XRD results. The thicknesses of the $Bi_{1.5}Zn_{1.0}Nb_{1.5}O_7$ thin films determined by SEM are about 600 nm and 400 nm on Pt/Si and LAO substrates, respectively.

## 5.3 Dielectric properties of $Bi_{1.5}Zn_{1.0}Nb_{1.5}O_7$ thin films and their varactors

### 5.3.1 Fabrications of $Bi_{1.5}Zn_{1.0}Nb_{1.5}O_7$ thin film varactors

For dielectric properties characterization at microwave frequency, parallel plate metal-insulator-metal (MIM) capacitor and planar plate interdigital capacitor structures are fabricated. During fabrication process, 1 um thick Au layer is first deposited on the top of the thin films by RF sputtering and gold plating techniques described in chapter2. For parallel plate Au/BZN/Pt varactor, circle Au top electrodes with diameter 13um are coated on the top of the $Bi_{1.5}Zn_{1.0}Nb_{1.5}O_7$ thin film on Pt/Si substrate by standard positive lithography and wet etching method using designed soft mask. For planar plate interdigital varactor, fingers of electrodes are patterned on the top of $Bi_{1.5}Zn_{1.0}Nb_{1.5}O_7$ thin film on LAO substrate by negative lithography and wet etching method using designed hard mask. Figure5.3 below shows the fabrication flow of these varactors,

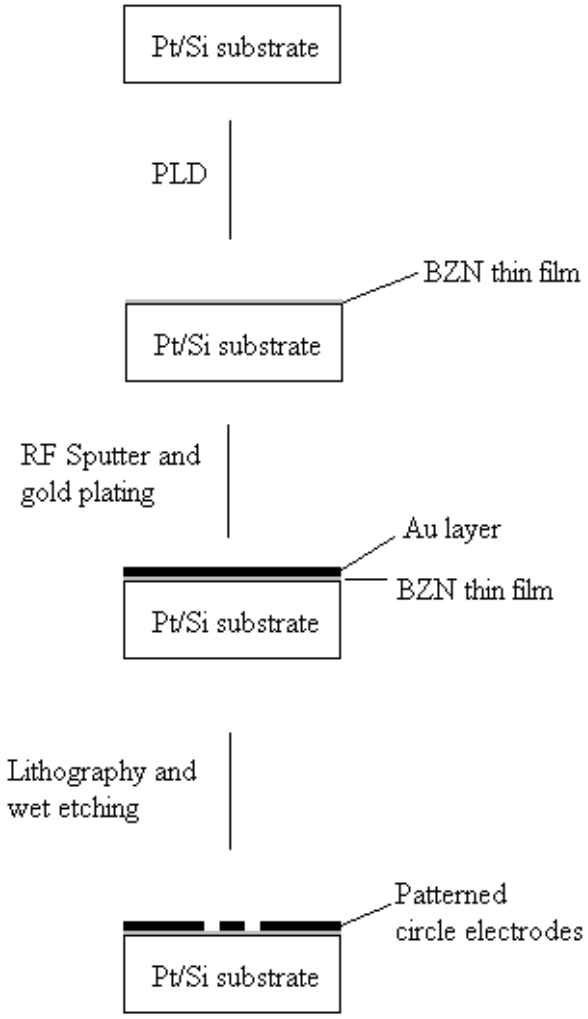
Pt/Si substrate
PLD
BZN thin film
Pt/Si substrate
RF Sputter and
gold plating
Au layer
BZN thin film
Pt/Si substrate
Lithography and
wet etching
Patterned
circle electrodes
Pt/Si substrate

(a)

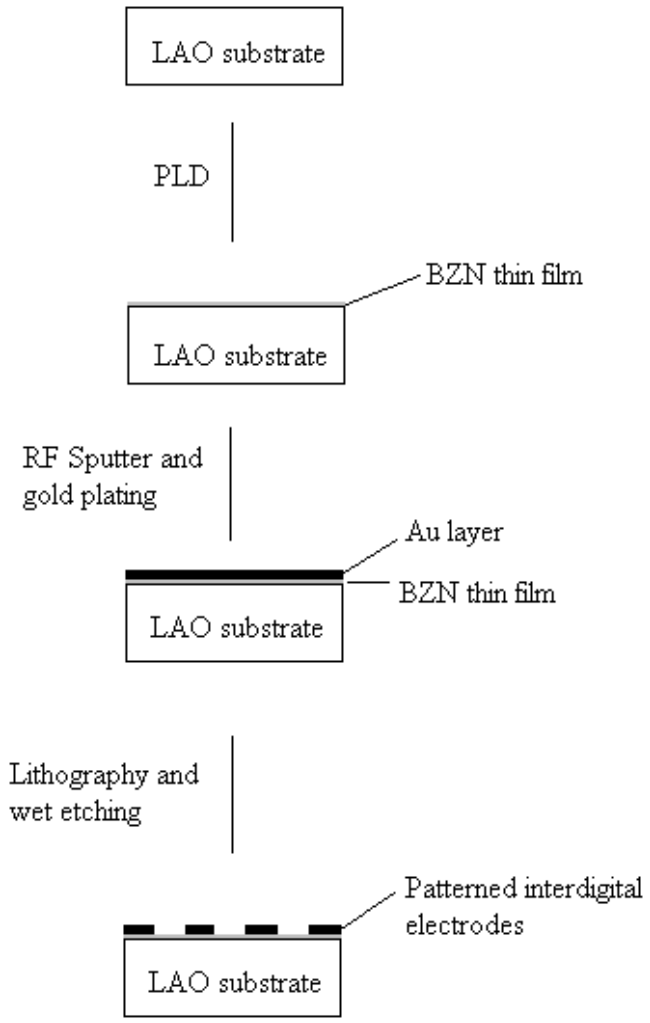


(b)

Figure5.3 Fabrication process flow of $Bi_{1.5}Zn_{1.0}Nb_{1.5}O_7$ thin film (a) parallel plate varactor on Pt/Si substrate and (b) planar plate interdigital varactor on LAO substrate.

Patterns of varactor electrodes after fabrication are shown in figure5.4,

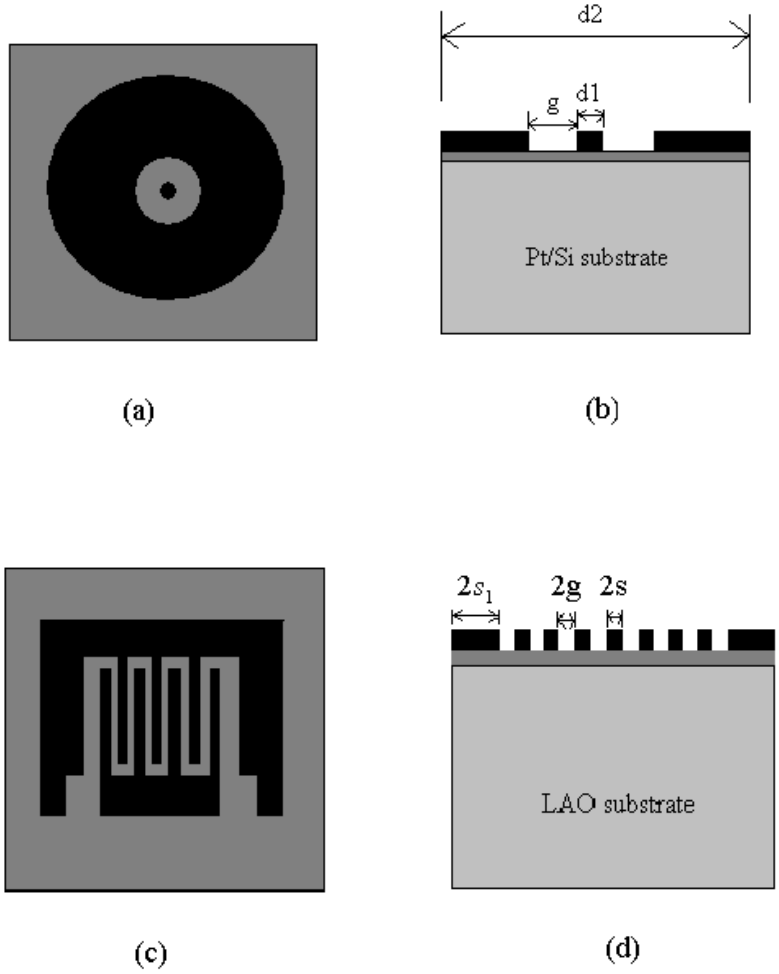


Figure5.4 Patterns of $Bi_{1.5}Zn_{1.0}Nb_{1.5}O_7$ thin film varactors on Pt/Si substrate (a) top view and (b) side view; on LAO substrate (c) top view and (d) side view.

The dimension specifications are: for parallel plate varactor on Pt/Si substrate, diameter of inner circle $d_1$ is 26um, diameter of the outer circle $d_2$ is 400um, gap between two circle electrodes g is 30um; for interdigital varactor on LAO substrate, width of internal

finger $2s$ is 10um, width of external finger $2s_1$ is 100um, gap between internal fingers $2g$ is 10um.

### 5.3.2 Microwave dielectric properties characterization

Microwave dielectric properties of the $Bi_{1.5}Zn_{1.0}Nb_{1.5}O_7$ thin films and varactors are characterized based on parallel plate Au/BZN/Pt MIM varactor and planar plate interdigital varactor structures shown in figure5.5 below.

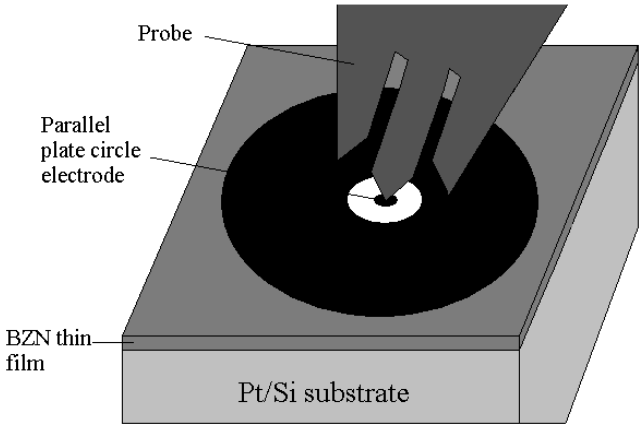


(a)

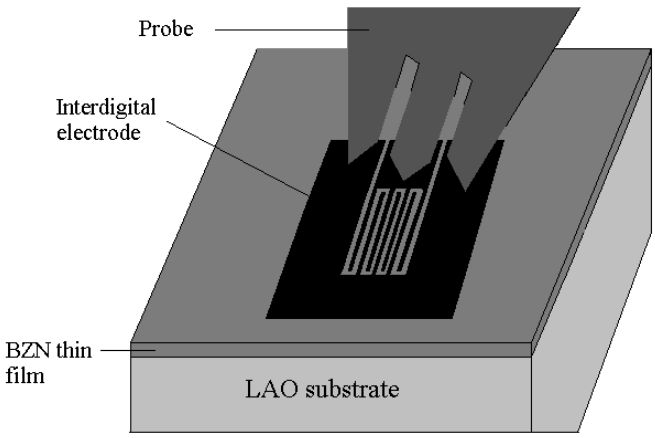


(b)

Figure5.5. Measurement setup for $Bi_{1.5}Zn_{1.0}Nb_{1.5}O_7$ thin film (a) parallel plate and (b) interdigital varactors.

For the parallel plate varactor, the CPW probe makes contact to the inner circular patch of metal which functions as the top electrode of the capacitor, and the metal outside the ring which functions effectively as the ground. For interdigital varactor, the CPW probe makes contact to the fingers metal alternatively to pass through signals and functions as grounds, respectively.

For both varactors, microwave parameters of varactors and dielectric properties of thin films are extracted from data of complex reflection coefficient ( $S_{11}$ ) measured using PNA series Network Analysis (Agilent N5230A) with coplanar waveguide probe station (GGB Industries Model 40A) at microwave frequency range. In order to perform the one-port reflection measurement, a one-port short-open-load calibration is performed over a frequency range from 0.6 GHz to 20GHz using standard calibration wafer. The

impedance of the varactor under test $Z_{test}$ could be derived from the measured $S_{11}$ data by the formula,

$$Z_{test} = Z_0 \frac{1+S_{11}}{1-S_{11}} = \mathrm{Re}[Z_{test}] + j\,\mathrm{Im}[Z_{test}] \qquad (5.1)$$

Where $Z_0$ is the characteristic impedance of the transmission cable and is usually 50Ω, $S_{11}$ is the complex reflection coefficient measured. Then the capacitance and loss tangent of varactors could be obtained according to the impedance of varactor $Z_{test}$ by formulas

$$C = \frac{1}{j\omega Z_{test}} = C' - jC'' \qquad (5.2)$$

$$C' = \mathrm{Re}\left[\frac{1}{j\omega Z_{test}}\right] \qquad (5.3)$$

$$\tan\delta = \frac{C'}{C''} = -\frac{\mathrm{Im}[\frac{1}{j\omega Z_{test}}]}{\mathrm{Re}[\frac{1}{j\omega Z_{test}}]} = -\frac{\mathrm{Re}[Z_{test}]}{\mathrm{Im}[Z_{test}]} \qquad (5.4)$$

where $C'$ and $C''$ are the real and imaginary part of complex capacitance, respectively.

#### 5.3.2.1 Performance of varactors

For parallel plate varactor shown in figure5.5 (a), the capacitance calculated by equation (5.3) is the capacitance of inner circle $1/j\omega C_{inner}$ and outer circle $1/j\omega C_{outer}$ in series as shown in figure5.6 below,

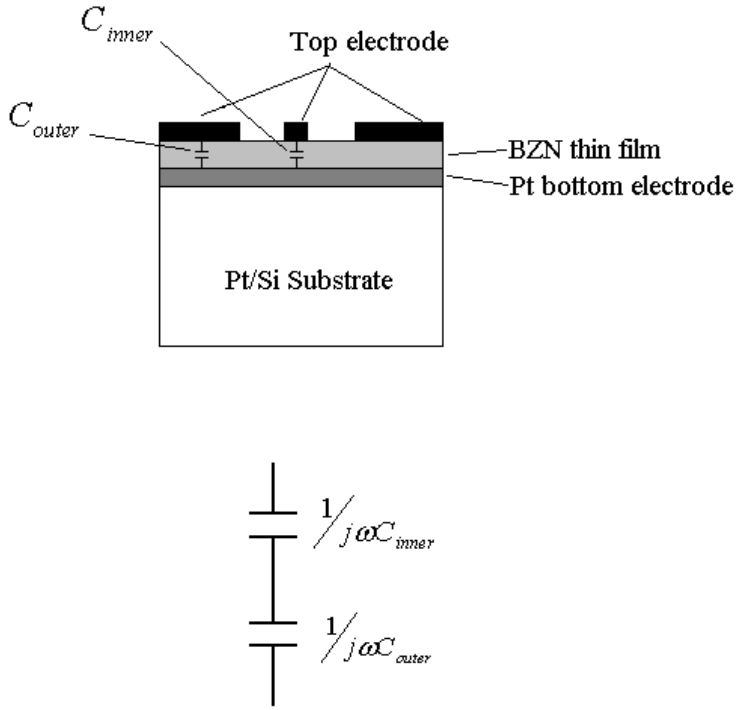


Figure5.6 Equivalent circuit of BZN thin film parallel plate varactor including inner circle and outer circle capacitors.

The capacitance of a parallel plate varactor is proportional to the area of the electrodes according to the formula $C' = \frac{\varepsilon_0 \varepsilon_r A}{t}$, where $C'$ is the capacitance of varactor, $\varepsilon_0$ is the dielectric constant of vacuum, $\varepsilon_r$ is the relative dielectric constant of material, A is the area of electrode, t is the distance between electrodes. Here, the radius of the inner electrode is 13um and that of outer electrode is 200um. Due to the much larger area of outer electrodes, the capacitance of the outer circle is much larger than that of inner circle so that the impedance of the outer circle capacitor is much smaller than the inner circle

capacitor and could be omitted. Therefore, the capacitance calculated according to equation (5.3) could be the capacitance of inner circle capacitor.

Figure5.7 shows the zero-bias capacitance and loss tangent of both varactors measured at microwave frequency from 0.6GHz to 20GHz at room temperature:

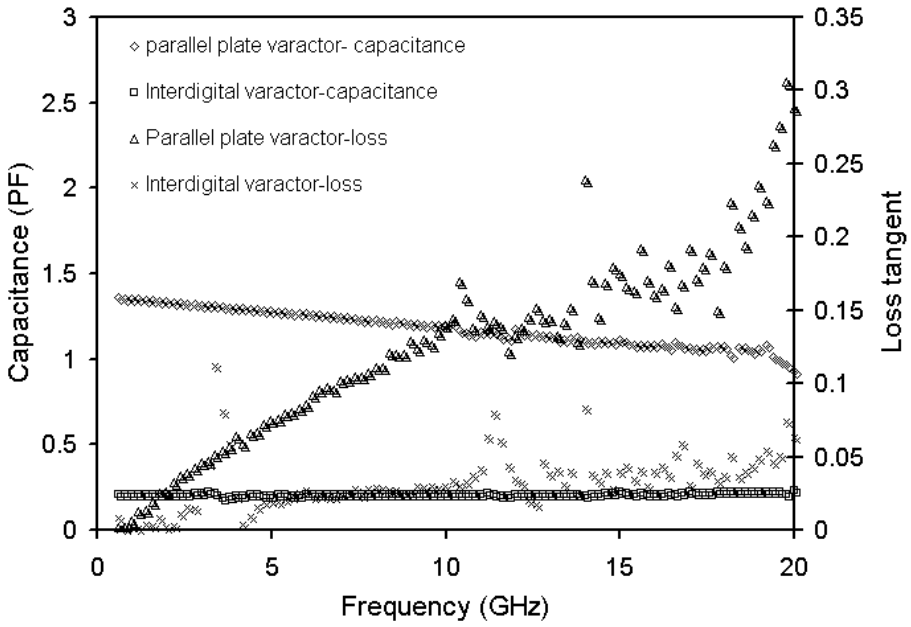


Figure5.7. Measured zero-bias capacitance and loss tangent of $Bi_{1.5}Zn_{1.0}Nb_{1.5}O_7$ thin film parallel plate and interdigital varactors at room temperature.

Measurement results show that capacitance of $Bi_{1.5}Zn_{1.0}Nb_{1.5}O_7$ thin film parallel and interdigtal varactors are 1.35PF and 0.22PF respectively. Capacitance of parallel plate varactor decreases with increasing measurement frequency to 1PF at 20GHz while capacitance of interdigtal varactor remains frequency independent at the whole frequency

range. Other groups also reported a similar dependence of capacitance and loss tangent on frequency for parallel plate varactor even at low frequency range of 1 KHz - 1MHz [4, 15]. This dependence may be partly due to the finite conductivity of platinum bottom electrodes. In the case of a perfect conductivity bottom electrode used, the electric field is normal to the electrode surface as shown in figure5.8 (a). When platinum electrode with finite conductivity is used, the current flowing in it will cause a potential different with position and affect the electric field distribution as shown in figure5.8 (b), where the direction of electric field will not be perpendicular to the bottom electrode surface and hence capacitance of this varactor is smaller than the previous one. This effect will be significant as frequency increasing and exhibits a decrease of capacitance with frequency.

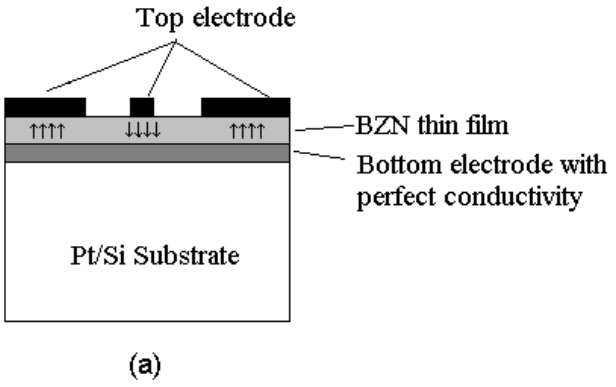


(a)

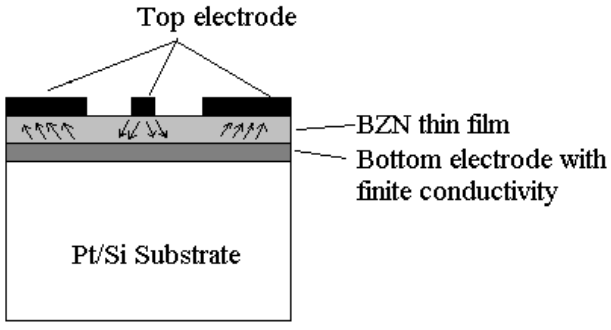


(b)

Figure5.8 a schematic graph of electric field distribution of parallel plate varactor with (a) perfect conductivity and (b) finite conductivity bottom electrode.

Loss tangent of parallel plate and interdigital varactors are very low for both structures, which are 0.0057 and 0.0025 at 1GHz, respectively. With the increment of frequency, loss tangent of parallel varactor increases. For thin film varactors, dielectric loss in the thin film, conductor loss from metal electrodes, and radiation contribute the total device loss. In equation5.1, impedance of the varactor under test is expressed in terms of complex capacitance of varactor, which means the loss tangent calculated using equation5.4 is actually the ratio of the real and imaginary parts of varactor impedance and represent the total loss. To separate resistive loss of electrodes from the intrinsic dielectric losses, the impedance of the varactor could be modified with an additional term R, which indicates the ohm losses caused by electrodes. Due to the small volume of our capacitors, radiation could be omitted. An equivalent circuit is shown in figrue5.9 below.

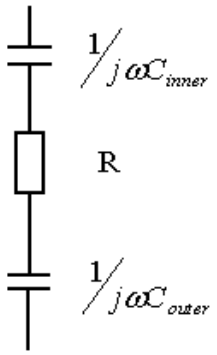


Figure5.9. A simplified equivalent circuit of the parallel plate varactor on Pt/Si subtrate.

The impedance and loss tangent of the varactor could be expressed by,

$$Z_{test} = R + \frac{1}{j\omega C_{inner}} = R + \frac{1}{j\omega(C_{inner}^{'} - jC_{inner}^{"})} = R + \frac{C^{"}}{\omega(C^{'2} + C^{"2})} - \frac{jC^{'}}{\omega(C^{'2} + C^{"2})} \qquad (5.5)$$

$$\tan\delta = \frac{\mathrm{Re}[Z_{test}]}{\mathrm{Im}[Z_{test}]} = \frac{\omega R(C^{'2} + C^{"2})}{C^{'}} + \frac{C^{"}}{C^{'}} \qquad (5.6)$$

Because generally $C^{"} << C^{'}$ for most cases, equation 5.6 could be approximated as,

$$\tan\delta = \omega R C^{'} + \frac{C^{"}}{C^{'}} \qquad (5.7)$$

From equation (5.7), when conductor loss R is extracted from the impedance, a clear formula could be obtained to express the total loss tangent of under test varactor by two terms: the first term represents conductors' contributions and the second term is the intrinsic loss tangent of thin film. The loss tangent resulting from conductors is proportional to conductor resistance R, measurement frequency $\omega$ as well as the real part of varactor capacitance $C^{'}$. Due to its narrow distance between electrodes for parallel plate varactor, $C^{'}$ will be rather large. Therefore, when frequency increases to microwave frequency, total losses of device will be dominated by conductor losses of the Pt bottom electrode and the deterioration of calculation accuracy by resistive parasitics will be significant.

The loss tangent will show weaker frequency dependence, according to equation 5.7 and explanation above, for a thicker Pt electrode, which means a smaller R. Juwei et al reported the effect of bottom electrode thickness on loss tangent [8]. Even at low frequency 100MHz, loss tangent increase significantly when the thickness of Pt bottom electrode is reduced from 100nm to 30nm[8].

Another method to alleviate this problem is to implement varactors with capacitance $C'$ as small as possible, which could be achieved, according to the formula calculating capacitance of parallel plate varactor $C = \frac{\varepsilon_0 \varepsilon_r A}{t}$, by growing thicker thin film and/or fabricating smaller area electrodes. Figure5.10 shows the measured loss tangent of parallel varactors with different electrodes size.

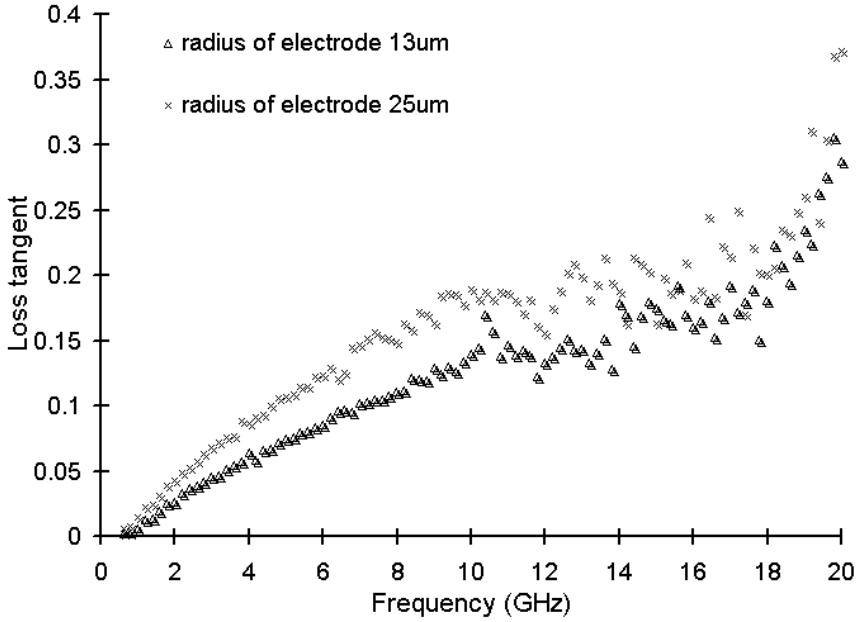


Figure5.10. Loss tangent of $Bi_{1.5}Zn_{1.0}Nb_{1.5}O_7$ thin film parallel plate varactor with two sizes of electrodes.

It can be seen that varactor with large area electrode exhibit more rapid increase of loss tangent with increasing frequency, which is consistent with equation5.7 and indicates the conductor loss mechanism of the varactor because the intrinsic loss of $Bi_{1.5}Zn_{1.0}Nb_{1.5}O_7$

thin film will not change with different varactor geometry. In addition, it may be reasonable to assume that smaller size of electrodes, which means smaller real part of the capacitance of the parallel plate varactor $C^{'}$, will be desirable for accurate measurement of the dielectric properties of parallel plate varactors. A problem accompanying with small electrodes is more conductor loss created. Therefore, the choice of geometrical design can have a strong influence over the varactor losses.

Correction methods are also studied to remove the effect from electrodes. For example, Kenji et al proposed an open and short circuit, which have the same configuration as the original varactor except for a part of the top electrode, to remove the parasitic effects [16]. This method was adopted by Jaehoon Park et al to characterize dielectric properties of $Bi_{1.5}Zn_{1.0}Nb_{1.5}O_7$ thin film [17]. Ma et al used circle electrodes pattern, the same as that in this study, for microwave measurement of parallel plate varactor. A set of formula were deduced to calculate the impedance of the inner circle and the gap. By subtracting the impedance of two varactors, which have different inner electrode area but the same gap between the inner and outer electrodes, the impedance of outer circle could be eliminated [18]. These methods prove usable; however, problems exist due to the different electromagnetic boundary conditions of the open and short correction circuits with original device, this will affect the solution of Maxwell equations and deteriorate the accuracy. The same thing happens on Ma's method.

$Bi_{1.5}Zn_{1.0}Nb_{1.5}O_7$ thin film interdigital varactor in figure5.7 shows low loss tangent less than 0.01 until resonant frequency of the LCR circuit, which is caused by the capacitance

and inductance of the varactor and measurement circuit. Because of the independence of capacitance on frequency, no dielectric relaxation occurs. The slowly increase of loss tangent with increasing frequency may be due to the conductor loss from interface effect between $Bi_{1.5}Zn_{1.0}Nb_{1.5}O_7$ film and gold electrodes. Other researchers suggest that a rapid thermal annealing treatment could improve the interface between film and electrodes [5, 8]. Further research could be undertaken.

#### 5.3.2.2 Dielectric response of $Bi_{1.5}Zn_{1.0}Nb_{1.5}O_7$ thin films

Complex relative permittivity of $Bi_{1.5}Zn_{1.0}Nb_{1.5}O_7$ thin film based on parallel varactor structure could be calculated by the equation,

$$\varepsilon_r = \frac{C \cdot t}{\varepsilon_0 \cdot A} \qquad (5.8)$$

where $C$ is the complex varactor capacitance calculated by equation (5.2), t is the thickness of $Bi_{1.5}Zn_{1.0}Nb_{1.5}O_7$ thin film, $\varepsilon_0$ is relative permittivity of vacuum, A is the area of varactor electrodes.

That of $Bi_{1.5}Zn_{1.0}Nb_{1.5}O_7$ thin film based on interdigital varactor structure is calculated using a conformal mapping method [19]. Firstly, the varactor capacitance could be divided into three parallel parts: the capacitance from the two outermost finger gaps $C_{outer}$, the capacitance from the inner $n-3$ fingers $C_{inner}$ if the fingers number $n>3$, and the capacitance from all the fingers' ends $C_{end}$,

$$C = C_{outer} + C_{inner} + C_{end} \tag{5.9}$$

$$C_{outer} = 4l\varepsilon_0\varepsilon_{outer}\frac{K(k'_{0outer})}{K(k_{0outer})} \tag{5.10}$$

$$C_{inner} = (n-3)l\varepsilon_0\varepsilon_{inner}\frac{K(k_{0inner})}{K(k'_{0inner})} \tag{5.11}$$

$$C_{end} = 4ns(2+\pi)\varepsilon_0\varepsilon_{end}\frac{K(k_{0end})}{K(k'_{0end})} \tag{5.12}$$

Here each part of the capacitance is approximated to be composed of three parallel capacitances: air, thin film and substrate with the effective relative permittivity,

$$\varepsilon_{outer} = 1 + q_{1outer}\frac{\varepsilon_1 - 1}{2} + q_{2outer}\frac{\varepsilon_2 - 1}{2} \tag{5.13}$$

$$\varepsilon_{inner} = 1 + q_{1inner}\frac{\varepsilon_1 - 1}{2} + q_{2inner}\frac{\varepsilon_2 - 1}{2} \tag{5.14}$$

$$\varepsilon_{end} = 1 + q_{1end}\frac{\varepsilon_1 - 1}{2} + q_{2end}\frac{\varepsilon_2 - 1}{2} \tag{5.15}$$

where $\varepsilon_1$ and $\varepsilon_2$ are the relative permittivity of substrate and thin film, respectively.

$$q_{iouter} = \frac{K(k_{iouter})}{K(k'_{iouter})}\frac{K(k'_{0outer})}{K(k_{0outer})} \qquad i = 1,2 \tag{5.16}$$

$$q_{iinner} = \frac{K(k_{iinner})}{K(k'_{iinner})}\frac{K(k'_{0inner})}{K(k_{0inner})} \qquad i = 1,2 \tag{5.17}$$

$$q_{iend} = \frac{K(k_{iend})}{K(k'_{iend})}\frac{K(k'_{0iend})}{K(k_{0iend})} \qquad i = 1,2 \tag{5.18}$$

Ks are the complete elliptic integral of the first kind,

$$k_{0outer} = \frac{s}{s+2g}\sqrt{\frac{1-\left(\frac{s+2g}{s+2s_1+2g}\right)^2}{1-\left(\frac{s}{s+2s_1+2g}\right)^2}} \qquad (5.19)$$

$$k_{iouter} = \frac{\sinh\left(\frac{\pi s}{2h_i}\right)}{\sinh\left(\frac{\pi(s+2g)}{2h_i}\right)}\sqrt{\frac{1-\frac{\sinh^2\left[\frac{\pi(s+2g)}{2h_i}\right]}{\sinh^2\left[\frac{\pi(s+2s_1+2g)}{2h_i}\right]}}{1-\frac{\sinh^2\left(\frac{\pi s}{2h_i}\right)}{\sinh^2\left[\frac{\pi(s+2s_1+2g)}{2h_i}\right]}}} \qquad i=1,2 \quad (5.20)$$

$$k'_{iouter} = \sqrt{1-k_{iouter}^2} \qquad i=0,1,2 \qquad (5.21)$$

$$k_{0inner} = \frac{s}{s+g} \qquad (5.22)$$

$$k_{iiner} = \frac{\sinh\left(\frac{\pi s}{2h_i}\right)}{\sinh\left[\frac{\pi(s+g)}{2h_i}\right]}\sqrt{\frac{\cosh^2\left[\frac{\pi(s+g)}{2h_i}\right]+\sinh^2\left[\frac{\pi(s+g)}{2h_i}\right]}{\cosh^2\left(\frac{\pi s}{2h_i}\right)+\sinh^2\left[\frac{\pi(s+g)}{2h_i}\right]}} \qquad i=1,2 \quad (5.23)$$

$$k'_{iiner} = \sqrt{1-k_{iiner}^2} \qquad i=0,1,2 \qquad (5.24)$$

$$k_{0end} = \frac{x}{x+2g_{end}}\sqrt{\frac{1-\left(\frac{x+2g_{end}}{x+w+2g_{end}}\right)^2}{1-\left(\frac{x}{x+w+2g_{end}}\right)^2}} \qquad (5.25)$$

$$k_{iend} = \frac{\sinh\left(\frac{\pi x}{2h_i}\right)}{\sinh\left(\frac{\pi\left(x+2g_{end}\right)}{2h_i}\right)}\sqrt{\frac{1-\frac{\sinh^2\left[\frac{\pi\left(x+2g_{end}\right)}{2h_i}\right]}{\sinh^2\left[\frac{\pi\left(x+2w+2g_{end}\right)}{2h_i}\right]}}{1-\frac{\sinh^2\left(\frac{\pi x}{2h_i}\right)}{\sinh^2\left[\frac{\pi\left(x+2w+2g_{end}\right)}{2h_i}\right]}}}, \quad i=1,2 \qquad (5.26)$$

$$k'_{iend} = \sqrt{1-k_{iend}^2}, \quad i=0,1,2 \qquad (5.27)$$

where $h_1$ and $h_2$ are thickness of substrate and thin film, respectively. $s$ and $s_1$ are the half inner and outer finger width, $l$ is inner finger length, g is half gap width between inner fingers, $g_{end}$ is the gap between the finger end and the end strip, $x$ is the length of the finger end, w is end strip width.

Figure5.11 below shows the dielectric properties of $Bi_{1.5}Zn_{1.0}Nb_{1.5}O_7$ thin film without and with bias electric field at microwave frequency on the two substrates.

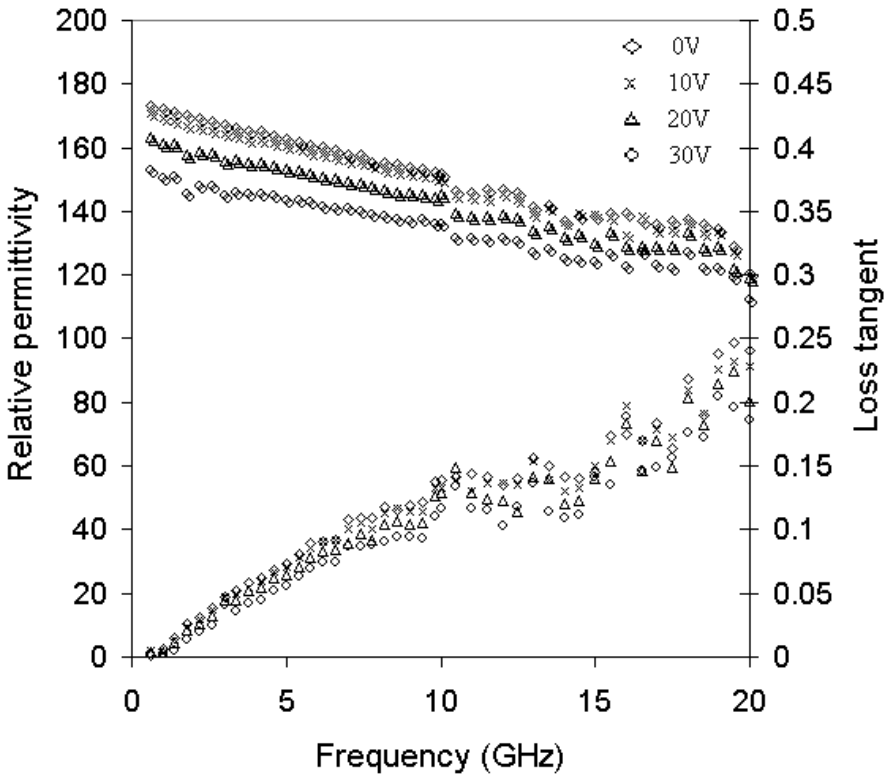
Relative permittivity
Loss tangent
Frequency (GHz)
0V
10V
20V
30V
200
180
160
140
120
100
80
60
40
20
0
0.5
0.45
0.4
0.35
0.3
0.25
0.2
0.15
0.1
0.05
0
0
5
10
15
20

(a)

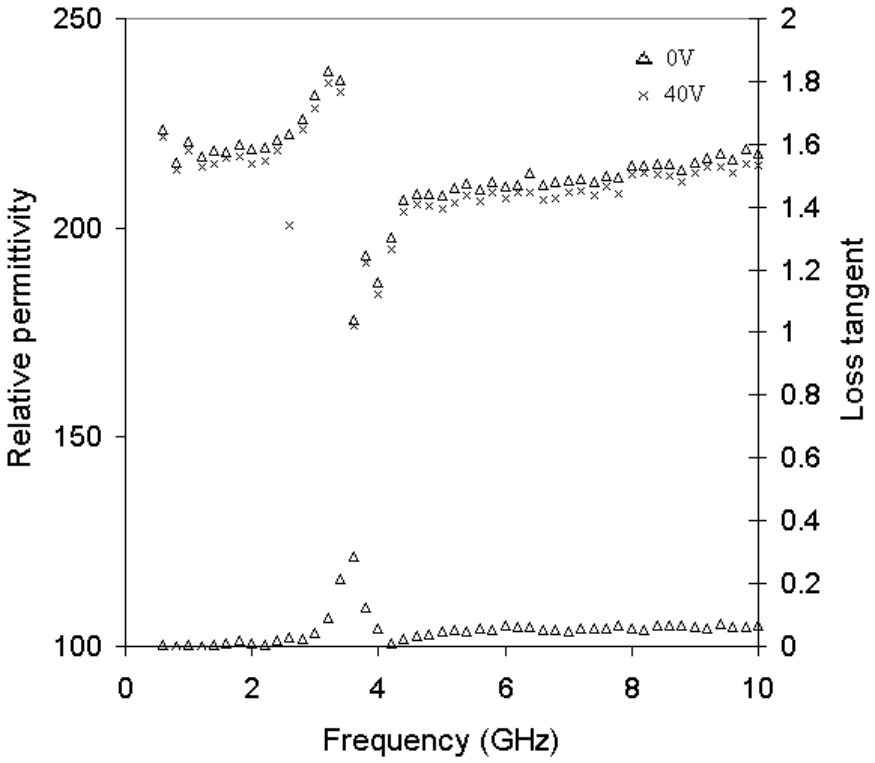


(b)

Figure5.11. Relative permittivity and loss tangent of $Bi_{1.5}Zn_{1.0}Nb_{1.5}O_7$ thin films on Pt/Si and LAO measured at zero and none-zero bias states.

It can be seen that the relative permittivity of $Bi_{1.5}Zn_{1.0}Nb_{1.5}O_7$ thin films are about 172 on Pt/si substrate and 220 on LAO substrate, which agree well with other reported values[4-5]. The larger in-plane relative permittivity of film on LAO substrate may reflect dielectric properties of (400) oriented $Bi_{1.5}Zn_{1.0}Nb_{1.5}O_7$ thin film. Another aspect may play a role is a dielectric layer with low relative permittivity on the interface between film and electrodes. This effect will reduce both in-plane and out-of-plane

measured effective relative permittivity but will be more significant on the out-of-plane one.

The loss tangent of $Bi_{1.5}Zn_{1.0}Nb_{1.5}O_7$ thin films on Pt/Si and LAO substrates are 0.0057 and 0.0047 at 1GHz, respectively. Other groups also reported loss tangent in an order of $10^{-3}$ at frequency range from 10 KHz - 1MHz [1-3]. The loss tangent of $Bi_{1.5}Zn_{1.0}Nb_{1.5}O_7$ film on Pt/Si substrate decrease with applying bias electric field and that of $Bi_{1.5}Zn_{1.0}Nb_{1.5}O_7$ film on LAO substrate shows unchanged (not shown). This may because that the bias electric field applied to interdigital varactor is so small that change of loss tangent is beyond the accuracy of the measurement.

Bias electric field dependence of normalized relative permittivity for both $Bi_{1.5}Zn_{1.0}Nb_{1.5}O_7$ thin films at 1GHz is shown figure5.12.

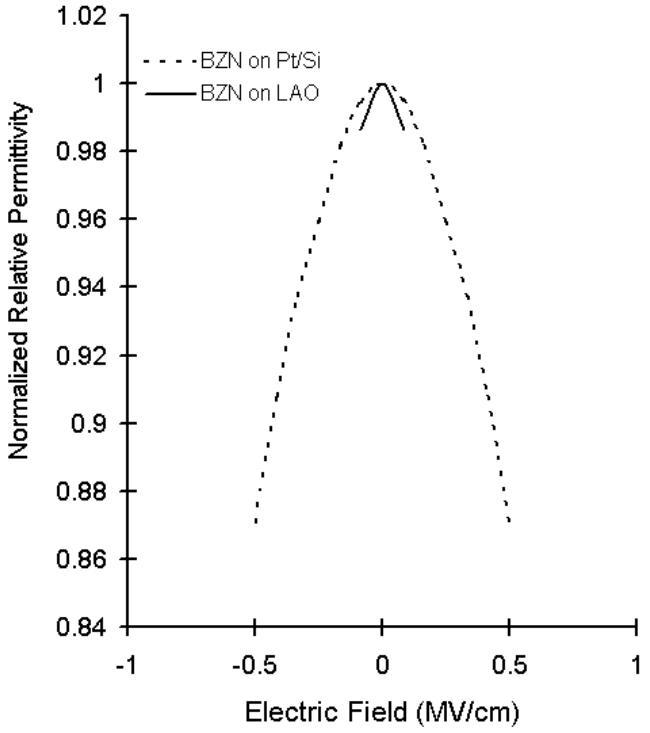


Figure5.12. Bias electric field dependence of normalized relative permittivity of $Bi_{1.5}Zn_{1.0}Nb_{1.5}O_7$ thin films on Pt/Si and LAO substrates measured at 1GHz.

The curve is symmetric with respect to zero bias and has no hysteresis. The tunability is 13.1% with an applied electric field of 500KV/CM and 1.4% with an applied electric field of 80KV/CM for $Bi_{1.5}Zn_{1.0}Nb_{1.5}O_7$ thin films on Pt/Si and LAO substrates, respectively. The small tunability of film on LAO substrate is due to the relatively large distance between electrodes of interdigital varactor structure and no evidence of saturation shown. Under the same bias electric field, the tunability of $Bi_{1.5}Zn_{1.0}Nb_{1.5}O_7$ thin film on LAO substrate is larger than those on Pt/Si substrate. This difference in tunability of films on the two substrates reflects the difference in dielectric constant.

Table below summaries the microwave dielectric properties of varactors and $Bi_{1.5}Zn_{1.0}Nb_{1.5}O_7$ thin film on these two substrates.

| | Parallel plate varactor on Pt/Si substrate | Interdigital varactor on LAO substrate |
|---|---|---|
| frequency | 1GHz | 1GHz |
| Capacitance of varactor | 1.35PF | 0.22PF |
| Loss tangent of varactor | 0.0057 | 0.0025 |
| Thickness of film | 600nm | 400nm |
| Relative pemittivity | 172 | 220 |
| Loss tangent of film | 0.0057 | 0.0043 |
| Applied voltage (electric field) | 30V ( 500KV/cm) | 40V ( 80KV/cm) |
| Tunability | 13.1% | 1.4% |

Table1. Dielectric performance of $Bi_{1.5}Zn_{1.0}Nb_{1.5}O_7$ thin films and their varactors characterized at microwave frequency

**5.4 Summary**

In this chapter, $Bi_{1.5}Zn_{1.0}Nb_{1.5}O_7$ thin films are deposited by PLD method and characterized at microwave frequency up to 20GHz based on both parallel plate MIM varactor structure on platinum coated silicon substrate and planar plate interdigital varactor on single crystal LAO substrate at room temperature, respectively. Measurement results show that at 1GHz measurement frequency $Bi_{1.5}Zn_{1.0}Nb_{1.5}O_7$ film on Pt/Si substrate presents a relative permittivity of 172, low loss tangent of 0.0057, tunability of 13.1% under bias electric field of 500KV/cm; those of film on LAO are 220, 0.0043 and 1.4% under 80KV/cm applied electric field. The small tunability of $Bi_{1.5}Zn_{1.0}Nb_{1.5}O_7$ film

on LAO substrate is due to its large distance between electrodes of interdigital structure. Through the whole measurement frequency up to 20GHz, the relative permittivity decreases and loss tangent increases with increasing frequency for the $Bi_{1.5}Zn_{1.0}Nb_{1.5}O_7$ film on Pt/Si substrate with parallel plate varactor structure due to the ohm losses from electrodes; for film on LAO substrate with interdigital structure, the dielectric constant remains independence with frequency and loss tangent increase slightly due to film-electrode interface effects. In summary, this low dielectric loss tangent and medium relative permittivity and tunability indicate that $Bi_{1.5}Zn_{1.0}Nb_{1.5}O_7$ thin film could be promising candidate for tunable microwave devices applications

**Reference**

[1] Wei Ren, Susan Trolier-McKinstry, Clive A. Randall, and Thomas R. Shrout, Bismuth zinc niobate pyrochlore dielectric thin films for capacitive applications, *Journal of applied physics*, Volume 89, Number 1, Pages 767-774 (2001)

[2]Young P. Hong, Seok Ha, Ha Yong Lee, Young Cheol Lee, Kyung Hyun Ko, Dong-Wan Kim, Hee Bum Hong and Kug Sun Hong, Voltage tunable dielectric properties of rf sputtered $Bi_2O_3$ - $ZnO$ - $Nb_2O_5$ pyrochlore thin films, *Thin Solid Films*, Volume 419, Pages 183-188 (2002)

[3] S.HA, Y.S.LEE, Y.P.HONG, H.Y.LEE, Y.C.LEE, K.H.KO, D.W.KIM, H.B.HONG and K.S.HONG, The effect of substrate heating on the tunability of rf-sputtered $Bi_2O_3$ - $ZnO$ - $Nb_2O_5$ thin films, *Applied physics A*, Volume 80, Pages 585-590 (2005)

[4] S.W.Jiang, B.Jiang, X.Z.Liu and Y.R.Li, Laser deposition and dielectric properties of cubic pyrochlore bismuth zinc niobate thin films, *Journal of Vacuum Science and Technology A*, Volume 24, 261-263 (2006)

[5] R. L. Thayer, C. A. Randall and S. Trolier-McKinstry, Medium permittivity bismuth zinc niobate thin film capacitors, *Journal of applied physics*, Volume 94, Number 3, Pages 1941-1947 (2003)

[6]Shan-Tao Zhang, Yi-Zhang, Ming-Hui Lu, Yan-Feng Chen and Zhi-Guo Liu, Structures and dielectric properties of $Bi_{1.5}Zn_{1.0}Nb_{1.5-x}Ti_xO_7$ (x=0, 0.05 and 0.10) thin films, *Applied physics letters*, Volume 90, 042903 (2007)

[7]Alexander K. Tagantsev, Jiwei Lu and Susanne Stemmer, Temperature dependence of the dielectric tunability of pyrochlore bismuth zinc niobate thin films, *Applied physics letters*, Volume 86, 032901 (2005)

[8] Jiwei Lu and Susanne Stemmer, Low-loss, tunable bismuth zinc niobate films deposited by rf magnetron sputtering, *Applied physics Letters*, Volume 83, Number 12, Pages 2411-2413 (2003)

[9]Donhang Liu, Yi Liu, Shui-Q. Huang and Xi Yao, Phase structure and dielectric properties of $Bi_2O_3$ - $ZnO$ - $Nb_2O_5$ based dielectric ceramics, *Journal of the American ceramic society*, Volume 76, Pages 2129-2132 (1993)

[10] Xiaoli Wang, Hong Wang, and Xi Yao, Structures, phase transformations, and dielectric properties of pyrochlore containing bismuth, *Journal of the American ceramic society*, Volume 80, Pages 2745-2748 (1997)

[11] I. Levin, T.G.Amos, J.C.Nino, T.A.Vanderah, C.A.Randall and M.T.Lanagan, Structural study of an unusual cubic pyrochlore $Bi_{1.5}Zn_{0.92}Nb_{1.5}O_{6.92}$ , *Journal of solid state chemistry*, Volume 168, Pages 69-75 (2002)

[12] R.L.Withers, T.R.Welberry, A.-K.Larsson, Y.Liu, L.Noren, H.Rundlof and F.J.Brink, Local crystal chemistry, induced strain and short range order in the cubic pyrochlore $(Bi_{1.5-\alpha}Zn_{0.5-\beta})(Zn_{0.5-\gamma}Nb_{1.5-\delta})O_{(7-1.5\alpha-\beta-\gamma-2.5\delta)}$ (BZN), *Journal of Solid state chemistry*, Volume 177, Issue 1, Pages 231-244 (2004)

[13] Stanislav Kamba, Viktor Porokhonskyy, Alexej Pashkin, Viktor Bovtun, Jan Petzelt, Juan C. Nino, Susan Trolier-McKinstry, Michael T. Lanagan, and Clive A. Randall, Anomalous broad dielectric relaxation in $Bi_{1.5}Zn_{1.0}Nb_{1.5}O_7$ pyrochlore, *Physical review B*, Volume 66, 054106 (2002)

[14] Juan C. Nino, Michael T. Lanagan, and Clive A. Randall, and Stanislav Kamba, Correlation between infrared phonon modes and dielectric relaxation in $Bi_2O_3$ - $ZnO$ - $Nb_2O_5$ cubic pyrochlore, *Applied Physics Letters*, Volume 81, Number 23, Pages 4404-4406 (2002)

[15] L Z Cao, W Y Fu, S F Wang, Q Wang, Z H Sun, H Yang, B L Cheng, H Wang and Y L Zhou, *C*-axial oriented (Bi1.5Zn0.5)(Zn0.5Nb1.5)O7 thin film grown on Nb doped SrTiO3 substrate by pulsed laser deposition, *Journal of physics D*, Volume 40, Pages 1460-1463 (2007)

[16] Kenji Ikura, Yohtaro Umeda and Yasunobu Ishii, Measurement of high-frequency dielectric characteristics in the mm-wave band for dielectric thin films on semiconductor substrates, *Japanese Journal of Physics*, Volume 34, Pages L1211-L1213 (1995)

[17] Jaehoon Park, Jiwei Lu, Susanne Stemmer and Robert A.York, Microwave dielectric properties of tunable capacitors employing bismuth zinc niobate thin films, *Journal of Applied physics*, Volume 97, 084110 (2005)

[18] Zhengxiang Ma, Andew J. Beck, P. Polakos, Harold Huggins, John Pastalan, Hui Wu, K, Watts, Y. H. Wong, and P. Mankiewich, RF measurement technique for characterizing thin dielectric films, *IEEE transactions on electron devices*, Volume 45, Number 8, Pages 1811-1816 (1998)

[19] Spartak *S.* Gevorgian, Torsten Martinsson, Peter L. J. Linnkr,and Erik Ludvig Kollberg, CAD Models for Multilayered Substrate Interdigital Capacitors, , *IEEE transactions on microwave theory and techniques*, Volume 44, Number 6, Pages 896-904 (1996)

# Chapter6:
# Conclusion

My study mainly concerns room temperature microwave thin film tunable devices, which use gold thin film as a conducting strip.

A microwave tunable coupled open-loop resonators band-pass filter and a tunable coupled microstrip lines phase shifter are implemented with $Ba_{0.5}Sr_{0.5}TiO_3$ thin film varactors. Measurement results show that the filter had a good performance from 7GHz to 11GHz. The central frequency is 9.390GHz at unbiased state and the 3dB bandwidth is 10.22%. Frequency tunability is 0.8% when 200V bias voltage is applied. The insertion loss at zero bias state is 2.27dB, stopband rejection larger than 30dB and return loss larger than 15dB. The phase shifter has insertion loss 2.5dB and return loss greater than 10 dB at the frequency range from 8GHz to 12GHz with a phase shift nearly 15 degree at 200V DC bias. Insertion loss is one of the main challenge during design and fabrication of these filter and phase shifter due to the relative high dielectric loss of $Ba_{0.5}Sr_{0.5}TiO_3$ thin film as well as the ohm loss in the gold conducting layer compared with HTS ones. It is encouraging to see from the experimental results that insertion losses of both devices are less than 3dB.

As the dielectric loss of BST is relative large, we also look into other potential thin film material, namely $Bi_{1.5}Zn_{1.0}Nb_{1.5}O_7$. $Bi_{1.5}Zn_{1.0}Nb_{1.5}O_7$ is not ferroelectric and has very low

dielectric loss. Because research on $Bi_{1.5}Zn_{1.0}Nb_{1.5}O_7$ is new in our lab and thin film qualities will have significant influence on its properties. My first step is to prepare stoichiometric ceramic target and then try to find out optimal PLD parameters for thin film deposition. After this, characterization is performed at microwave frequency by extracting the complex capacitance of parallel plate and interdigital varactors from measured reflection scattering parameters. Complex relative permittivity of thin films could be calculated based on the complex capacitance of varactors. Measurement results show medium relative permittivity of $Bi_{1.5}Zn_{1.0}Nb_{1.5}O_7$ thin films 220 and 172, loss tangents 0.0043 and 0.0057 in in-plane and out-plane directions, respectively. Tunability of out-of-plane relative permittivity is 13% under 500KV/CM bias electric field and that of in-plane one is 1.4% under 80KV/cm applied electric field. These properties prove $Bi_{1.5}Zn_{1.0}Nb_{1.5}O_7$ thin film parallel plate varactors suitable for tunable device applications, however, the relative large bias electric field needed for effective tuning limits applications of $Bi_{1.5}Zn_{1.0}Nb_{1.5}O_7$ thin film in the form of planar plate varactor.